EPIC: Equivalence Principle Tests in Cosmology

Ana Marta Machado de Pinho
Mestrado em Astronomia
Departamento de Física e Astronomia
2016

Orientador
Carlos Martins, Investigador, Centro de Astrofísica da Universidade do Porto

Coorientador
Matteo Martinelli, Investigador, Leiden Institute of Physics

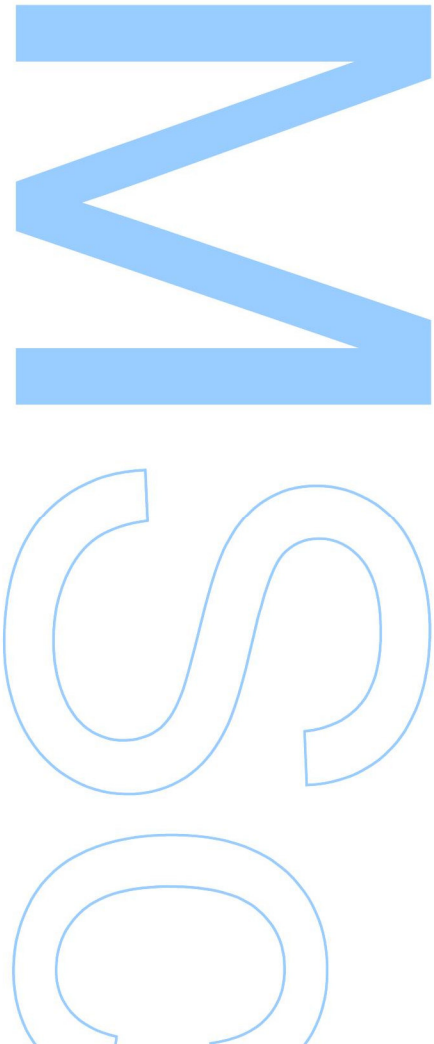

U.PORTO

FACULDADE DE CIÊNCIAS
UNIVERSIDADE DO PORTO

Todas as correções determinadas pelo júri, e só essas, foram efetuadas.

O Presidente do Júri,

Porto, _____/_____/_____

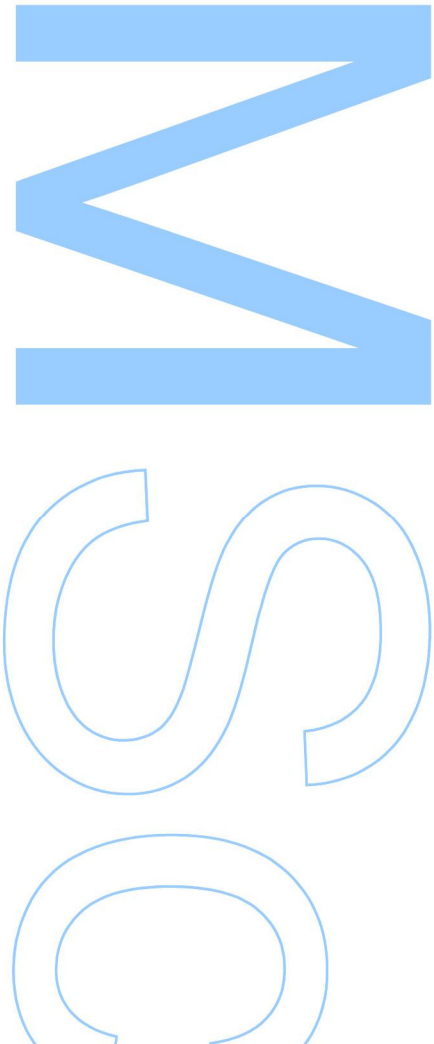

EPIC: Equivalence Principle Tests in Cosmology

Master in Astronomy Dissertation

Author:

Ana Marta Machado de Pinho[1,2]

Supervisors:

Carlos Martins[1] and Matteo Martinelli[3]

Affiliations:

[1]Centro de Astrofísica, Universidade do Porto, Rua das Estrelas, 4150-762 Porto, Portugal

[2]Departamento de Física e Astronomia, Faculdade de Ciências, Universidade do Porto, Rua do Campo Alegre, 4169-007 Porto, Portugal

[3]Institute Lorentz, Leiden University, PO Box 9506, Leiden 2300 RA, The Netherlands

"Somos um ínfimo grão de poeira cósmica."

Acknowledgements

I would like to thank Carlos Martins for the all the work we have done in these past few years, for introducing me and teaching me the dark side of the Universe. I would like to thank Matteo Martinelli for friendly hosting me at Heidelberg, for being available and to travel with me to the wonderful world of debugging. I also would like to thank Luca Amendola and everyone on the cosmology group for the warm hospitality at Heidelberg.

To all my astrofamily, a big thank you. We sure are a tiny cosmic dust grain and every single person taught me something. From the olddest to the youngest, I am gratuful that I have met you. In particular, a deep thank you to João, Filipe and Manuel, for this lovely university journey, as well a big thank you to Patrick, Raquel, João Ferreira and Catarina Leite for all the guidance and help. I also would like to thank to Mariana, Ana Martins, Tita and Catarina Santos for your sweet friendship.

To Rui Jorge, thank you for being my fundamental constant.

To my mother that I will never thank enough times as she is the one that makes everything possible. To my father for being available and supportive. And to all my family that care, motivate and celebrate with me in this and every chapter of my life.

Abstract

The Weak Equivalence Principle is the cornerstone of General Relativity, which is though to describe the dynamics of the Universe. With the significant improvements on spectroscopy, we aim to explore how astrophysical tests can shed light on the current paradigma.

The discovery of cosmic acceleration hints for an unaccounted matter component of the Universe. The standard cosmological model is consistent with most observations but its well known fine tuning problems led to formulations of alternative scenarios. From dynamical dark energy models to modified gravity, there are several theories that predict a violation of the Equivalence Principle.

In this work, we use astrophysical measurements of fundamental couplings and other cosmological parameters to assess and constraint possible time and spatial variations of the fine structure constant, α, in particular, through other dimensionless couplings. For instance, such variations can be found in dynamical dark energy models where a scalar field coupled with the electromagnetic sector is responsible for all or part of the accelerated expansion of the Universe.

Astrophysical tests with high precision spectroscopic measurements are a very useful tool, providing competitive constraints, compared with local one's on the Eötvös parameter which measures the violation of the Weak Equivalence Principle. Furthermore, the upcoming facilities of high precision ultra stable spectrographs will contribute to a new precision era of fundamental physics tests.

Keywords

Equivalence Principle Tests, Stability Tests of Fundamental Couplings, Dark Energy

Resumo

O Princípio de Equivalência Fraco é o pilar da Relatividade Geral, que se pensa descrever a dinâmica do Universo. Com as melhorias significativas em espetroscopia, pretendemos explorar como testes astrofísicos podem clarificar o paradigma atual.

A descoberta da aceleração cósmica sugere uma componente de matéria do Universo não contabilizada. O modelo cosmológico padrão é consistente com a maioria das observações mas os seus conhecidos problemas de "fine tuning" levaram a formulações de cenários alternativos. Desde modelos de energia escura dinâmica até gravidade modificada, existem várias teorias que prevêem uma violação do Princípio de Equivalência.

Neste trabalho, usamos medições astrofísicas de constantes fundamentais e outros parâmetros cosmológicos para avaliar e obter limites de possíveis variações temporais e espaciais da constante de estrutura fina, α, em particular. Por exemplo, tal variação pode ser encontrada em modelos de energia escura dinâmica onde um campo escalar acoplado com o sector eletromagnético é total ou parcialmente responsável pela expansão acelerada do Universo.

Testes astrofísicos com medições espetroscópicas de alta precisão são uma ferramenta muito útil, fornecendo limites competitivos, em relação aos já existentes, do parâmetro de Eötvös que mede a violação do Princípio de Equivalência Fraco. Além disso, as próximas instalações de espectrógrafos de alta precisão ultra estáveis irão contribuir para uma nova era de precisão de testes de física fundamental.

Palavras chave

Energia escura, Testes de constantes fundamentais, Testes do Princípio de Equivalência

Contents

1 Introduction **19**

1.1 Einstein's Equivalence Principle 19

1.2 General Relativity and the Standard Cosmological Model 21

1.3 Varying fundamental constants 24

1.4 Data and methods 28

1.4.1 Available datasets 28

1.4.2 χ^2 techniques 29

2 Time variation **31**

2.1 $w_0 = constant$ 31

2.2 One parameter redshift-dependent equation of state 36

2.2.1 A thawing model by Slepian et al. 36

2.2.2 A class of freezing models 41

2.3 Two parameters redshift-dependent equation of state 48

2.3.1 Chevalier-Polarsky-Linder parametrization 48

2.3.2 Early Dark Energy model 52

3 Dipole variation and data consistency tests **57**

3.1 Dipole variation 57

3.1.1 Pure spatial dipole variation 58

3.1.2 Redshift dependent spatial dipole variation 59

3.2 Data consistency tests 65

4 Spatial variation **69**

4.1 Observed angular power spectrum 69

4.2 Theoretical power spectrum 76

4.2.1 Symmetron model 76

4.3 Data analysis 81

5 Conclusions **87**

Bibliography **89**

A Cosmological measurements **101**

A.1 Measurements of the Hubble parameter, $H(z)$ 101

A.2 Measurements of luminosity distance 103

B Measurements of the fine structure constant, α **127**

B.1 Atomic clock measurements 127

B.2 Recent dedicated measurements 127

B.3 Archival measurements 129

C Measurements of the proton-electron mass ratio, μ **141**

D Measurements of combinations of fundamental couplings, $\Delta Q/Q$ **143**

List of Figures

2.1 Two-dimensional likelihood contours for a constant equation of state with the one, two and three sigma constrains in the $\zeta - w_0$ plane with red for the α measurements, blue the cosmological datasets and black for the combined dataset. The red lines in the top panel corresponds to the Webb measurements, in the middle to recent dedicated measurements and in the bottom panel to the atomic clock measurement. 34

2.2 Two-dimensional likelihood contours for a constant equation of state with the one, two and three sigma constrains in the $\zeta - w_0$ plane for all the combination of all the datasets. 35

2.3 Two-dimensional likelihood contours for the Slepian et al. (2014) model with the one, two and three sigma constrains in the $\zeta - w_0$ plane with red for the α measurements, blue the cosmological datasets and black for the combined dataset. The red lines in the top panel corresponds to the Webb measurements, in the middle to recent dedicated measurements and in the bottom panel to the atomic clock measurement. 39

2.4 Two-dimensional likelihood contours for the Slepian et al. (2014) model with the one, two and three sigma constrains in the $\zeta - w_0$ plane for all the measurements combined. 40

2.5 One-dimensional likelihood contours for the Slepian et al. (2014) model marginalizing over the other parameter: for ζ on the top panel and for w_0 using cosmological and Webb data (blue dashed), cosmological and dedicated measurements of α (blue dash-dotted), cosmological and atomic clocks (red dotted) and the combination of all datasets (black solid). 40

2.6 Two-dimensional likelihood contours for the dilaton model with the one, two and three sigma constrains in the $\zeta - w_0$ plane with red for the α measurements, blue the cosmological datasets and black for the combined dataset. The red lines in the top panel corresponds to the Webb measurements, in the middle to recent dedicated measurements and in the bottom panel to the atomic clock measurement. 44

2.7 Two-dimensional likelihood contours for the dilaton model with the one, two and three sigma constrains in the $\zeta - w_0$ plane for all the measurements combined. 45

2.8 One-dimensional likelihood contours for the dilaton model: for ζ (marginalizing over w_0) on the top panel and for w_0 (marginalizing over ζ) using cosmological and Webb data (blue dashed), cosmological and dedicated measurements of α (blue dash-dotted), cosmological and atomic clocks (red dotted) and the combination of all datasets (black solid). 45

2.9 Two-dimensional likelihood contours on the $\zeta - w_0$ plane with one, two and three sigma levels for all datasets combined with the Oklo bound in red and without in black. 47

2.10 One-dimensional likelihood contours for ζ on the left panel and for w_0 on the right panel with one, two and three sigma level for all datasets combined with the Oklo bound in red and without in black. 47

2.11 Two-dimensional likelihood contours for the CPL parametrization using all data combined. On the top panel is the $\zeta - w_0$ plane, $\zeta - w_a$ in the middle and $w_0 - w_a$ on the bottom panel marginalizing the remaining parameter. The contours correspond to the one, two and three sigma constraints. 50

2.12 One-dimensional likelihood contours for the CPL parametrization using all data combined. From the top to the bottom panel are the one, two and three sigma constraints for ζ, w_0 and w_a parameter, marginalizing the remaining parameters. 51

2.13 Two-dimensional likelihood contours for the EDE model parametrization using all data combined. On the top panel is the $w_0 - w_a$ plane, $w_0 - \zeta$ in the middle and $w_a - \zeta$ on the bottom panel marginalizing the remaining parameter. The contours correspond to the one, two and three sigma constraints. 54

2.14 One-dimensional likelihood contours for the EDE parametrization using all data combined. From the top to the bottom panel are the one, two and three sigma constraints for ζ, w_0 and Ω_e parameter, marginalizing the remaining parameters. 55

3.1 Two-dimensional likelihood contours for a pure spatial dipole parametrization. Webb *et al.* dataset in black, recent measurements in blue and all data in red. 61

3.2 One-dimensional likelihood contours for a pure spatial dipole parametrization. Webb *et al.* dataset in black, recent measurements in blue and all data in red. 62

3.3 Two-dimensional likelihood contours for a spatial dipole with redshift dependence parametrization. Webb *et al.* dataset in black, recent measurements in blue and all data in red. . . 63

3.4 One-dimensional likelihood contours for a spatial dipole with redshift dependence parametrization. Webb *et al.* dataset in black and all data in red. 64

3.5 Two dimensional likelihood contours for the parameters (P, Q) using all datasets available combined. 67

4.1 Angular power spectrum $\widehat{C}_l$ for the Keck dataset (blue), VLT dataset (red) and recent dedicated measurements (green) plotted together. 73

4.2 Angular power spectrum estimation $\widehat{C}_l$ as a function of the multipole ℓ with its expected error Σ for the datasets considered: Keck, VLT, Webb (Keck+VLT), recent dedicated measurements (New) and all datasets combined. 74

4.3 The logarithm of the expected error Σ of the estimator $\widehat{C}_l$ and the individual contributions of the shot noise Σ_{SN} and cosmic variance Σ_{CV} for each considered dataset. 75

4.4 Theoretical power spectrum $P_{\alpha-\bar{\alpha}}(k, a)$ given by eq. 4.27 as a function of the wavenumber k for $a = 1$ and different symmetry breaking scale factors $a_{SSB} = [0.33, 0.5, 0.66]$. In this plot a normalization factor was used $x = 0.06(0.5/a_{SSB})$. 79

4.5 Source distribution function in redshift space for the archival dataset (Webb et al. (2011)). 80

4.6 Theoretical power spectrum C_l for the symmetron model for different values of the scale factor for the symmetry breaking a_{SSB} in loglog scale. 81

4.7 Normalized posterior probability distribution contours from COSMOMC sampling only the a_{SSB} parameter. In the right panel, we use the archival dataset and in the left panel all data combined, with $log(\beta^2) = 1$ and $\lambda_{\phi 0} = 1$ fixed. 84

4.8 Normalized posterior probability distribution contours from COSMOMC sampling only the $log\beta^2$ parameter with different values of a_{SSB}. On the right panel, we use the archival dataset and on the left panel all data combined, with $\lambda_{\phi 0} = 1$ fixed. 84

4.9 Posterior probability distribution contours from COSMOMC sampling a_{SSB} and $log(\beta^2)$ using the archival dataset of α measurements (Webb et al. (2011)). On the top panel is the two-dimensional contours and on the bottom the one-dimensional normalized contours for the scale factor where the symmetry breaks a_{SSB} on the left and for logorithm of the strength of the coupling to gravity $log(\beta^2)$. 85

4.10 Posterior probability distribution contours from COSMOMC sampling a_{SSB} and $log\beta^2$ using all the datasets of α measurements combined. On the top panel is the two-dimensional contours and on the bottom the one-dimensional normalized contours for the scale factor where the symmetry breaks a_{SSB} on the left and for logorithm of the strength of the coupling to gravity $log(\beta^2)$. 86

List of Tables

2.1 Obtained constrains for the Slepian et al. (2014) model for different parameters using all datasets combined with and without the Oklo bound. 46

3.1 1σ and 3σ constrains on the free parameters for a pure spatial dipole. 59

3.2 1σ and 3σ constrains on the free parameters for a spatial dipole with redshift dependence. 60

4.1 Constrains on the symmetron parameters a_{SSB} and $log\beta^2$ with $\lambda_{\phi 0} = 1$ given by the archival dataset of α measurements of Webb et al. (2011) and all datasets combined (archival and recent dedicated measurements, table B.2). 83

4.2 2 σ constraints on the symmetron parameter $log\beta^2$ given by the Webb et al. (2011) dataset and all datasets combined (archival and recent dedicated measurements, table B.2) for different values of a_{SSB} and fixing $\lambda_{\phi 0} = 1$. 84

A.1 Compilation of measurements by Farooq et al. (2013) of the Hubble parameter and its error, σ_H for a given redshift, z. 101

A.2 Supernovae Type Ia luminosity distance measurements, its redshift and uncertainty from Suzuki et al. (2012), with the provided number of significant digits. 103

B.1 Atomic clock constrain on the current drift of α by Rosenband et al. (2008) where we assume $H_0 = 70 kms^{-1}Mpc^{-1}$. 127

B.2 Dedicated measurements of $\Delta\alpha/\alpha(z)$ in ppm from the UVES Large Program and other recent measurements. Note that the second measurement on table B.3 is the weighted mean from measurements in several absorption systems along lines of sight that are widely separated on the sky whose individual values were not reported by the authors. For that reason, this measurement will not be included in our analysis. The uncertainties of the measurements from Murphy et al. (2016) presented are the systematical and statistical uncertainties added in quadrature. 127

B.3 Archival measurements dataset of $\Delta\alpha/\alpha$ and its statistical uncertainty $\sigma_{\Delta\alpha/\alpha}$ used by Webb et al. (2011). σ_{flag} is the systematical error described on table B.4. The measurements are sorted by observational sub-samples within the telescope used as defined by Murphy et al. (2009). A is the previous low redshift sample from Murphy et al. (2003), B1 is the previous high redshift sample from Murphy et al. (2003), B2 is the addition of 15 absorbers from Murphy et al. (2004) and C is the labeled new sample from Murphy et al. (2003). D is for the VLT sample. 129

B.4 Values of the correspondent σ_{flag} in units of 10^{-5}- error associated to the random component (see Webb et al. (2011)). LC and HC mean "Low Constrast" and "High Contrast" as the Keck sample was computed in different ways. 140

C.1 Proton-electron mass ratio measurements compiled by Ferreira et al. (2015) listed by object along line of sight, the redshift and the value of the measurement with its corresponding uncertainty, as well as the original reference. 141

D.1 Combined measurements of the dimensionless couplings α, μ and g_p from the compilation of Ferreira et al. (2014) (and references therein). The list is sorted by redshift z and specifies the object along the line of sight, the dimensionless parameter being constrained and the measurement with its associated uncertainty in parts per million. . 143

D.2 Recent combined measurements of the dimensionless coupling $\alpha^2 g_p/\mu$. Listed is the name of the object along the line of sight, the redshift and the measurement itself with its corresponding uncertainty in parts per million. (Darling (2012) - Figure 4 - the individual data were requested directly to the author). 144

Chapter 1.

Introduction

The universe works in mysterious ways. Our work focuses on Equivalence Principle tests, in particular, how astrophysical tests of stability of fundamental couplings can probe dark energy. These stability tests can lead to constraints on the Eötvös parameter that measures the violation of the Weak Equivalence Principle. Also, we explore several paradigms where the variation of the fine-structure constant is the key observable consequence to survey and assess different explanations for the nature of dark energy.

1.1 EINSTEIN'S EQUIVALENCE PRINCIPLE

Einstein called it "der glücklichste Gedanke", or "the luckiest thought", of his life (Heaston (2008)). Formulated in 1907, the Einstein's Equivalence Principle (EEP) was the first step towards General Relativity. This theory that binds gravitation and the special theory of relativity only appeared in 1915. The Equivalence Principle traces back to Newton with the statement that mass of an object is proportional to its weight, known as its weak form (Will (2014)). One can also state the Weak Equivalence Principle (WEP) as "the trajectory of a *free* falling body is independent of its specific composition and structure", where no other forces play a role. Or reformulate it as two different bodies in a gravitational field fall with the same acceleration which is called the universality of the free fall.

The Einstein's Equivalence Principle is a wider concept (Will (2014)), that relies upon the validity of the

Weak Equivalence Principle and also on the statement that "the outcome of any local non-gravitational experiment is independent of the velocity of the freely-falling reference frame in which it is performed" (local Lorentz invariance) and also "independent of the where and when in the universe it is performed" (local position invariance). Thus, if these are valid, the effects of gravity must be equivalent to those of living in a curved spacetime.

To explain this phenomenon, there is a broad class of metric theories of gravity of which general relativity is an example, but also other theories, such as Brans-Dicke theory, are considered. Not included in this class are theories where varying non-gravitational constants are associated with dynamical fields that couple directly to matter, or superstring theory, which imply violations of the Weak Equivalence Principle. Therefore, such pillar of general relativity should be thoroughly tested.

There are several tests to each baseline of the Einstein Equivalence Principle such as the famous Michelson-Morley experiment for the local Lorentz invariance. Measuring gravitational redshift would assess the local position invariance but it also implies that fundamental constants of non-gravitational physics should be constant in time. Measurements of fundamental constants can be done by quantifying the present rate of variation, like in a clock comparison test, or by comparison with the value measured in the laboratory today using measurements from natural reactors such as the Oklo bound or from high precision astrophysical spectroscopy, with the ability to reach high redshift. One of our main results regarding tests of the Weak Equivalence Principle are constraints on the Eötvös parameter, that measures the fractional difference in acceleration between two bodies with different compositions in an external gravitational field. The inertial mass of such a body accounts for different kinds of mass-energy, for instance, rest energy or electromagnetic energy. Hence, if one of these types of energy contributes to the inertial mass in another way, it would mean there is a violation of the WEP. Suppose that the passive gravitational mass m_P is no longer equal to the inertial mass m_I in a gravitational field g (i.e., $m_I a = m_P g$), then one would have

$$m_P = m_I + \sum_A \frac{\eta^A E^A}{c^2} \tag{1.1}$$

with E^A the internal energy of the body due to interaction A, η^A is the Eötvös parameter, a dimensionless parameter that measures the strength of the violation of the WEP produced by that interaction, and the speed of light c. The Eötvös ratio of the relative accelerations between two bodies (a_1, a_2) is

then given by

$$\eta \equiv 2\frac{|a_1 - a_2|}{|a_1 + a_2|} = \sum_A \eta^A \left(\frac{E_1^A}{m_1 c^2} - \frac{E_2^A}{m_2 c^2} \right), \tag{1.2}$$

where the experimental bounds are found for η^A. Currently, the best available direct constraints stem from torsion balance tests (Wagner et al. (2012)) where

$$\eta = (-0.7 \pm 1.3) \times 10^{-13} \tag{1.3}$$

or from lunar laser ranging tests (Müller et al. (2012)) with

$$\eta = (-0.8 \pm 1.2) \times 10^{-13}. \tag{1.4}$$

The addition of bodies with self-gravitational interactions as celestial bodies and experiments involving gravitational forces to the EEP leads to the Strong Equivalence Principle. One can summarize this Strong Equivalence Principle in three parts: the WEP validity extends from self gravitating bodies to test bodies, the outcome of any local test experiment is independent of velocity of the free falling apparatus and of where and when in the universe it is performed. Hence the EEP is a special case of Strong Equivalence Principle ignoring local gravitational forces. The Strong Equivalence Principle is beyond the scope of this work, but obviously it will also be violated if the EEP is.

1.2 GENERAL RELATIVITY AND THE STANDARD COSMOLOGICAL MODEL

We will briefly introduce the concepts and equations necessary to describe the dynamics of the universe for the background cosmology scenarios discussed in the following work.

The matter/energy distribution determines the geometric properties of space-time in general relativity (Mo et al. (2010)). The Friedmann-Lemâitre-Robertson-Walker metric describes those properties for

a homogeneous and isotropic universe. The line element in 4 dimensions is given by

$$ds^2 = c^2dt^2 - a^2(t)\left[\frac{dr^2}{1-Kr^2} + r^2(d\theta^2 + sin^2\theta d\phi)\right] \tag{1.5}$$

where $a(t)$ is the scale factor depending on cosmic time t, that relates the real distance $\overrightarrow{r}$ with co-moving distance $\overrightarrow{x}$ that accounts for the expansion of the universe (Liddle (2003)). It is multiplied by the 3-dimensional space metric with a constant curvature K (Amendola and Tsujikawa (2010)). The closed, flat and open geometries correspond to $K = +1, 0$ and -1, and polar coordinates are used.

The single dynamical field of General Relativity is the metric g and there are no arbitrary functions or parameters except for the coupling constant G (Will (2014)). One can derive the GR field equations through the invariant action principle $\delta S = 0$, where

$$S = \frac{1}{16\pi G}\int \sqrt{g}Rd^4x + S_m(\phi_m, g_{\mu\nu}) \tag{1.6}$$

where R is the Ricci scalar, S_m is the matter action which depends on the matter fields ϕ_m which are coupled to the metric g. The variation of the action with respect to $g_{\mu\nu}$ leads to the field equations

$$G_{\mu\nu} \equiv R_{\mu\nu} - \frac{1}{2}g_{\mu\nu}R = 8\pi G T_{\mu\nu} + \Lambda \tag{1.7}$$

with $T_{\mu\nu}$ as the matter energy-momentum tensor, $G_{\mu\nu}$ the Einstein tensor and Λ the cosmological constant. The geometry of spacetime is given by the left hand side, as the right hand side expresses the energies and momenta of matter components (Amendola and Tsujikawa (2010)). Assuming that the energy-momentum tensor $T_{\mu\nu}$ takes the perfect fluid form

$$T^\mu_\nu = (\rho + P)u^\mu u_\nu + P\delta^\mu_\nu \tag{1.8}$$

with $u^\mu = (-1, 0, 0, 0)$ as the four-velocity fluid in comoving coordinates, and ρ and P are the energy density and pressure as function of t. Using $c = 1$ and taking the time-time component of Einstein equations, one can derive

$$\left(\frac{\dot{a}}{a}\right)^2 = \frac{8\pi G}{3}\rho - \frac{K}{a^2} \tag{1.9}$$

which is the Friedmann equation that describes the expansion of the Universe. One can rewrite this equation using the Hubble parameter given by $H \equiv \frac{\dot{a}}{a}$ that characterizes the expansion rate of the Universe. From the space-space component one can also get the Raychaudhuri equation

$$\frac{\ddot{a}}{a} = -\frac{4\pi G}{3}(\rho + 3P), \tag{1.10}$$

and after some algebra (or using the conservation of the energy-momentum tensor), one finds the continuity equation

$$\dot{\rho} + 3H(\rho + P) = 0. \tag{1.11}$$

Substituting the Friedmann equation and assuming that the universe is dominated by a single component with a constant equation of state as $w \equiv P/\rho = const.$ one can obtain

$$\rho \propto a^{-3(1+w)} \tag{1.12}$$

for a flat universe. For radiation, the equation of state $P = \rho/3$ is obeyed yielding $w = 1/3$. Thus, when radiation dominates, the cosmic evolution can be given by $\rho_{rad} \propto \frac{1}{a^4}$. We know that for the matter case, the pressure is negligible and if set to $p = 0$, the equation of state is $w = 0$. Consequently, during matter-domination era, the cosmic evolution goas as $\rho_{mat} \propto \frac{1}{a^3}$. The observed late time cosmic acceleration implies that $\ddot{a} > 0$ thus requiring

$$P < -1/3 \qquad \Longrightarrow \qquad w < -1/3 \tag{1.13}$$

for a postitive energy density ρ. Such conditions should be met by the Dark Energy component, introduced to explain the accelerated phase. When $w = -1$, then $p = -\rho$ and one gets the so called cosmological constant case. It can also be accounted on the Friedmann equation by adding an extra term as

$$H^2 = \frac{8\pi G}{3}\rho - \frac{K}{a^2} + \frac{\Lambda}{3} \tag{1.14}$$

where Λ is the cosmological constant. This can be interpreted as the vaccum energy density but particle physics theories predict $\rho_{vac} \approx 10^{74} GeV^4$ that is much larger than the observational bounds of dark energy $\rho_\Lambda \approx 10^{-47} GeV^4$. This is the well known cosmological constant problem (Amendola and Tsujikawa (2010)). If a cosmological constant is responsible for the late time cosmic acceleration, then there is a need to find a mechanism to match these values or alternative models.

Note that the Friedmann equation can be rewritten in terms of energy density dimensionless parameter $\Omega \equiv \rho/\rho_C$, where $\rho_C = \frac{3H^2}{8\pi G}$ is defined as the critical density which arises from a flat universe, thus

$$\Omega_m(t) + \Omega_r(t) + \Omega_\Lambda(t) + \Omega_k(t) = 1 \tag{1.15}$$

for matter, radiation and dark energy, respectively and with $\Omega_k = -\frac{K}{a^2}$.

1.3 VARYING FUNDAMENTAL CONSTANTS

Although a cosmological constant is still the simplest explanation for cosmic acceleration, its well known problems of fine-tuning led to the formulatation of alternative theories. The most natural alternative theory would involve scalar fields, of which the Higgs field is an example (Aad et al. (2012), Chatrchyan et al. (2012)).

If a dynamical scalar field is present, it is expected to couple with the rest of the theory, unless a still unknown symmetry supresses this coupling (Carroll (1998)). Particularly, the coupling of a dynamical field with the electromagnetic sector can lead to spacetime variations of the fine-structure constant, $\alpha \equiv \frac{e^2}{\hbar c^2}$ (Uzan (2011),Martins (2014)). There are some indications of such a variation (Webb et al. (2011)) at the parts-per-million level and the additional recent dedicated measurements provide motivation to repeat and deepen the study of such theories.

Martins (2014) distinguished two broad classes of models for the evolution of the fine structure constant. Class I corresponds to the models where the same dynamical degree of freedom provides

the variation of α and the dark energy responsible for the cosmic acceleration. Conversely in Class II they are independent, i.e., the degree of freedom is not responsible for the dark energy component. Our main focus is on Class I models but we also compare to an example of a Class II model (section 2.2.2).

We will assume that there is a dynamical scalar field responsible for dark energy, ϕ, which couples to the rest of the theory. The coupling between the scalar field and the electromagnetism stems from a gauge kinetic function $B_F(\phi)$

$$\mathcal{L}_{\phi F} = -\frac{1}{4} B_F(\phi) F_{\mu\nu} F^{\mu\nu}. \tag{1.16}$$

To a good aproximation, this function can be assumed to be linear,

$$B_F(\phi) = 1 - \zeta\kappa(\phi - \phi_0), \tag{1.17}$$

(where $\kappa^2 = 8\pi G$) since the absence of such a term would require the presence of a $\phi \to -\phi$ symmetry, but such symmetry must be broken throughout most of the cosmological evolution (Dvali and Zaldarriaga (2002)) as the field ϕ is a time-dependent field changing along most of the history. One can explicitly relate the evolution of α to dark energy with these assumptions. In summary, the evolution of α can be written as

$$\frac{\Delta\alpha}{\alpha} \equiv \frac{\alpha - \alpha_0}{\alpha} = B_F^{-1} = \zeta\kappa(\phi - \phi_0) \tag{1.18}$$

and using the fraction of the dark energy density

$$\Omega_\phi \equiv \frac{\rho_\phi(z)}{\rho_{tot}} \simeq \frac{\rho_\phi(z)}{\rho_\phi(z) + \rho_m(z)} \tag{1.19}$$

where we have neglected the contribution from radiation (since our measurements are low-redshift, $z < 5$, and the radiation density today is roughly $\Omega_r \approx 10^{-4}$), the evolution of the scalar field can be

expressed in terms of dark energy properties Ω_ϕ and w_ϕ as (Nunes and Lidsey (2004))

$$1 + w_\phi = \frac{(\kappa\phi')^2}{3\Omega_\phi} \tag{1.20}$$

where the prime denotes the derivative with respect to the logarithm of the scale factor. From the equation of state $w_\phi = P_\phi/\rho_\phi$ and as a canonical scalar field evolves as $\dot{\phi}^2 = (1 + w(z))\rho_\phi$ for a Friedmann-Lemâitre-Robertson-Walker universe, hence

$$\phi(z) - \phi_0 = \frac{\sqrt{3}}{\kappa}\int_0^z \sqrt{1 + w(z)}\left(1 + \frac{\rho_m}{\rho_\phi}\right)^{-1/2}\frac{dz}{1+z} \tag{1.21}$$

from which we finally obtain

$$\frac{\Delta\alpha}{\alpha}(z) = \zeta\int_0^z \sqrt{3\Omega_\phi(z)(1 + w_\phi(z))}\frac{dz'}{1+z'} \tag{1.22}$$

for a canonical scalar field, where $\Omega_\phi = \rho_\phi/(\rho_m + \rho_\phi)$. To include the case where $w_\phi < -1$, the evolution of α for a phantom field is given by

$$\frac{\Delta\alpha}{\alpha}(z) = -\zeta\int_0^z \sqrt{3\Omega_\phi(z)|1 + w_\phi(z)|}\frac{dz'}{1+z'} \tag{1.23}$$

where the change of sign is due to the fact that one expects the phantom field to roll up the potential rather than down. Thus, in these models, the evolution of α is characterized by cosmological parameters plus the coupling ζ, without referencing the putative scalar field.
In these models, it is also expected that the proton and electron masses vary due to the electromagnetic corrections of their masses (Uzan (2011)). Consequently, local tests of the equivalence principle lead to the conservative general constraint on the dimensionless coupling paramenter $|\zeta_{local}| < 10^{-3}$.

The realization that varying fundamental couplings induce violations of the universality of free fall is several decades old, going back to the work of Dicke (Damour and Donoghue (2010)). A light scalar field such as the one we are considering inevitably couples to nucleons due to the α dependence of their masses, and therefore mediates an isotope-dependent long-range force. This can be quantified by the dimensionless Eötvös parameter η, which describes the level of violation of WEP. One can show that for the class of models we are considering the Eötvös parameter and the dimensionless coupling

ζ are simply related by (Uzan (2011),Dvali and Zaldarriaga (2002),Chiba and Kohri (2002),Damour and Donoghue (2010))

$$\eta \approx 10^{-3}\zeta^2 \tag{1.24}$$

This relation only applies to Class I models.

In what follows we analyse three classes of models which taken together provide a reasonable sample of the allowed parameter space: a constant equation of state, one and two parameter redshift-dependent equations of state. Therefore we can examine and assess how the relevant constraints are model dependent while sustaining conceptual simplicity. Given that there are degeneracies between the coupling ζ and w_0 (which are partially broken by the cosmological datasets), one may legitimally ask how robust these constraints are. One goal of our work is to answer this question by extending the analysis to more general dark energy models.

We have done a systematic analysis on the stability tests of nature's fundamental couplings. Starting with time variation on chapter 2, we study different dark energy equations of state. From the constant equation of state to phenomenological parametrizations, we analyse the impact of the simplicity of the chosen model and assess the relevance of the constraints obtained with the current data presented in section 1.4. As recent dedicated measurements are now available, we search for a dipole spatial variation on chapter 3 that prompts data consistency tests which includes measurements of other fundamental couplings. Finally, chapter 4 will cover a spatial variation of α given by a modified gravity model. Conclusions can be found on chapter 5.

1.4 DATA AND METHODS

Available datasets

The different approaches to the Equivalence Principle tests need different data. The data used in our analysis can be summarized as follows:

- **Fine-structure constant measurements**

  We use spectroscopic measurements of α by Webb et al. (2011), an archival dataset of 293 measurements (table B.3) where the systematical uncertainties were obtained directly from the sample distribution. A compilation of recent dedicated measurements presented by table B.2 is also used. Early results from the UVES Large Program for Testing Fundamental Physics are included in the latter dataset, which are expected to have a better control over possible systematics. We also use the atomic clock constraint on the current drift of α from Rosenband et al. (2008) reported on table B.1. This is the strongest available laboratory constraint on α only. There are other laboratory constraints but these are weaker and depend on other couplings. The constraint is assessed by

$$\frac{1}{H_0}\frac{\dot{\alpha}}{\alpha} = \mp\zeta\sqrt{3\Omega_{\phi 0}|1+w_0|} \tag{1.25}$$

  with the minus and plus signs corresponding to the canonical and phantom case, respectively.

- **Cosmological measurements**

  The Union2.1 dataset of 580 Type Ia supernovae from Suzuki et al. (2012) (table A.2) and the compilation of Hubble parameter measurements of Farooq et al. (2013) are used and called cosmological data throughout our analysis. To a good aproximation, these measurements are insensitive to the value of α. Strictly speaking, a variation on α influences the luminosity of the Type Ia supernovae but the effect of a parts per million α variation is too small to significantly change the current data as recently reported by Calabrese et al. (2014) and therefore we will not

consider that effect in this analysis. These cosmological data will constrain and provide a prior on the dark energy equation of state.

- **Other fundamental constants measurements**

  Regarding the consistency tests, we use current joint measurements of multiple couplings on table D.1 and D.2. Measurements of the proton-electron mass ratio listed on table C.1 are also used.

χ^2 techniques

Our work relies on the comparison of the current available data with different models for dark energy equation of state. Thus, one way to measure the agreement between the model and the data is through chi-square techniques that can give the best fit parameters of that model considering the measurements made and their uncertainties (Press et al. (1988)). Each data point (x_i, y_i) has a correspondent standard deviation, σ_i. The maximum likelihood estimation is obtained by minimizing the chi-square, i.e.,

$$\chi^2 \equiv \sum_{i=1}^{N} \left(\frac{y_i - y(x_i; a_1, ..., a_M)}{\sigma_i^2} \right)^2 \tag{1.26}$$

where $y(x_i; a_1, ..., a_M)$ is the value predicted by the model regarding its M parameters $(a_1, ..., a_M)$ for the corresponding independent quantity x_i. This quantity assumes that the uncertainties of the measurements are normally distributed, and allows the extraction of relevant confidence levels. One can convert the χ^2 values into likelihood function $\mathcal{L}$ through the expression $log(\mathcal{L}) = -2\chi^2$, as some figures will present that quantity.

Chapter 2.

Time variation

Assuming that the variation of the fine structure constant is given by the same degree of freedom as the dinamical dark energy responsible for the cosmic accelerated expansion as described in section 1.3, we can choose a constant equation of state for dark energy, which is consistent with current data (if it is close to -1) and thus one gets a model close to the standard ΛCDM one, or choose a equation of state as a function of redshift. Our analysis will go through both cases: first we choose a constant equation of state $w = w_0$ which includes the case where $w = -1$, i.e., the standard ΛCDM model. Then we relax that assumption by studying one parameter redshift-dependent equations of state with examples of a thawing and a freezing model. We conclude the analysis by adding a parameter, i.e., two parameters redshift-dependent equation of state, focusing on the Chavalier-Polarinsky-Linder parametrization and Early Dark Energy model. The goal of this analysis is to get constrains with all the available measurements for the value of the equation of state today, w_0, the electromagnetic coupling to the scalar field, ζ and the additional parameter required by the models where the equation of state is a function of redshift.

2.1 $W_0 = CONSTANT$

To constrain w_0 and ζ, we will fix $H_0 = 70km/s/Mpc$, $\Omega_{m0} = 0.3$ and a flat universe that leads to $\Omega_{\phi 0} = 0.7$. This choice is consistent with the cosmological data used (see appendix A). Nevertheless,

we have explicitly verified that taking H_0, Ω_m or the curvature parameter as free parameters with an observationally motivated prior probability and marginalizing over these parameters does not significantly change our results.

Considering a 2D grid of ζ and w_0 values, we applied the standard chi-square techniques (see subsection 1.4.2) to set constraints to these parameters using different datasets as shown on figures 2.1 and 2.2. The archival dataset from Webb et al. (2011) leads to a non-zero coupling ζ at one-sigma level, however this preference vanishes at a two-sigma level. Furthermore, the recent dedicated measurements are fully consistent with the null result.

Assuming equation 1.25, the atomic clock constraint from Rosenband et al. (2008) is currently more constraining than the astrophysical measurements. This is the main result of our first analysis of constant dark energy equation of state (Martins et al. (2015)).

As aforementioned (see 1.4.1), the cosmological data considered are not sensitive to ζ and serve as a prior to w_0. Since our α measurements are independent, we obtain tighter constrains by combining all the datasets as figure 2.1 illustrates.

Marginalizing the coupling parameter ζ over the dark energy equation of state w_0, we get the 1D constrains. For the Webb et al. (2011) dataset there is a one-sigma preference for a non-zero coupling while the other datasets prefer a non-variation. The combination of all the datasets leads to a constraint of

$$|\zeta| < 5.2 \times 10^{-6} \tag{2.1}$$

which is a significant improvement over previous constrains. Note that at 3-sigma level , ζ is unconstrained even for the atomic clock measurement from Rosenband et al. (2008). This can be converted into a constraint on the Eötvös parameter, as we get

$$|\eta| < 2.7 \times 10^{-14}. \tag{2.2}$$

On the other hand, marginalizing the likelihood over the coupling parameter, the 1D likelihood gives a

best fit for w_0 with a three sigma confidence level of

$$w_0 = -1.00^{+0.12}_{-0.04}. \tag{2.3}$$

This bound should be read carefully, bearing in mind all the assumptions made for other cosmological parameters. Comparing our results to our previous ones (Martins et al. (2015)), the constraint is weaker on the dimensionless parameter ζ since the recent measurements added are consistent with no variation of α.

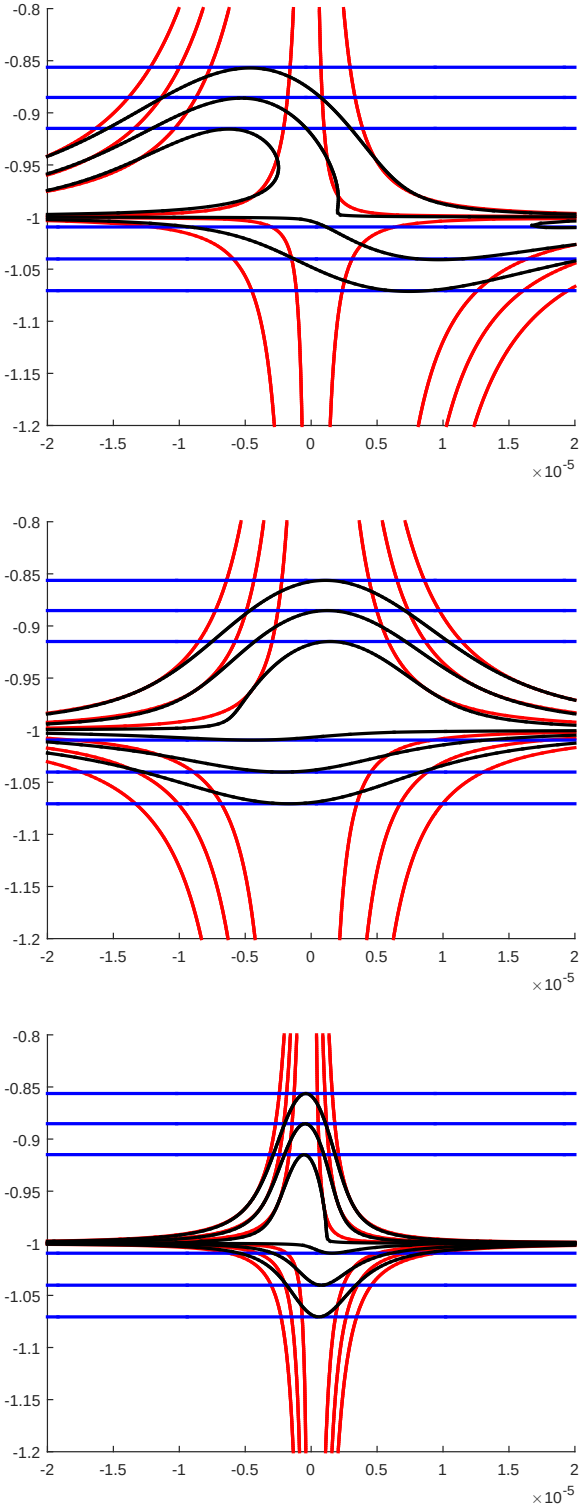

Figure 2.1: Two-dimensional likelihood contours for a constant equation of state with the one, two and three sigma constrains in the $\zeta - w_0$ plane with red for the α measurements, blue the cosmological datasets and black for the combined dataset. The red lines in the top panel corresponds to the Webb measurements, in the middle to recent dedicated measurements and in the bottom panel to the atomic clock measurement.

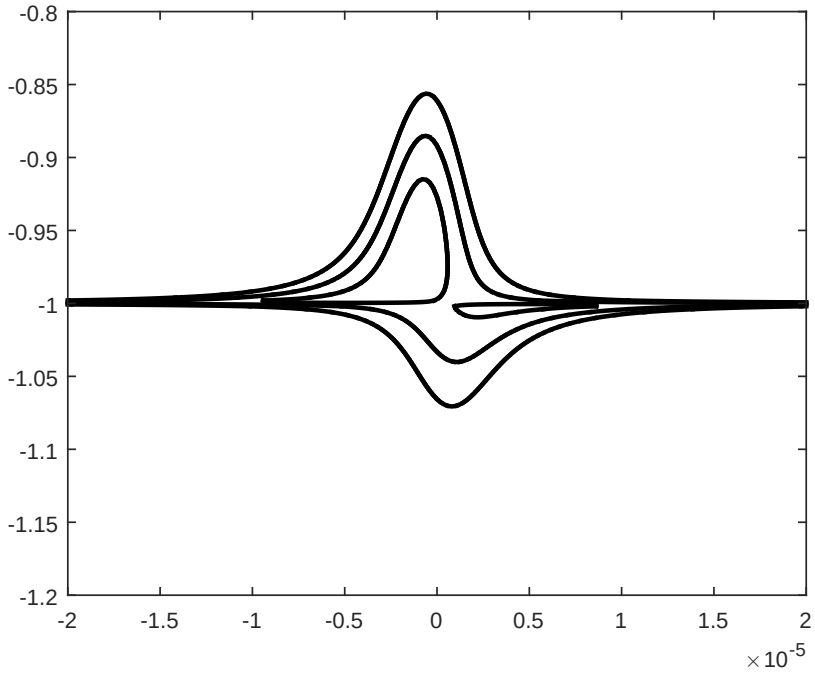

Figure 2.2: Two-dimensional likelihood contours for a constant equation of state with the one, two and three sigma constrains in the $\zeta - w_0$ plane for all the combination of all the datasets.

2.2 ONE PARAMETER REDSHIFT-DEPENDENT EQUATION OF STATE

We will now relax the assumption of a constant equation of state and study redshift-dependent models characterized by a single parameter w_0. This choice is made out of simplicity and also because the current available data weakly constrain additional free parameters and so we will work with more strict assumptions than the following case of two parameters redshift-dependent equation of state that is a more general case. We will present an example of a thawing model by Slepian et al. (2014) and a class of freezing models. A thawing model is the case where the scalar field is frozen at early times by Hubble damping until recently it starts to roll down the potential and evolving from $w < -1$. As for a freezing model, the scalar field was already rolling down the potential towards a new minimum but it slows down as it dominates leading to $w > -1$, initially (Cardwell and Linder (2005)).
Our analysis will remain on the $\zeta - w_0$ plane, which leads as well to the fixed parameters of $H_0 = 70km/s/Mpc$, $\Omega_{m0} = 0.3$ and a flat universe that gives $\Omega_{\phi 0} = 0.7$ as we will use the cosmological measurements and chi-square techniques as done in the previous section.

A thawing model by Slepian et al.

We will start with a recent model by Slepian et al. (2014) where the Friedmann equation takes form as

$$\frac{H^2(z)}{H_0^2} = \Omega_m(1+z)^3 + \Omega_\phi \left[\frac{(1+z)^3}{\Omega_m(1+z)^3 + \Omega_\phi}\right]^{\frac{1+w_0}{\Omega_\phi}} \tag{2.4}$$

As we assume a flat universe ($\Omega_m + \Omega_\phi = 1$), the model is characterized by three independent parameters: H_0, Ω_m (that will be fixed) and w_0 as the usual value of dark energy equation of state *today*. The dark energy equation of state is given by

$$w_{SGZ}(z) = -1 + (1+w_0)\frac{H_0^2}{H^2(z)} \tag{2.5}$$

where for high redshift, w_{SGZ} approaches -1 and diverges from it as the universe evolves until w_0. Therefore, this is a parametrization for thawing models. This choice is also supported by a recent result (Marsh et al. (2014)) indicating that the allowed quintessence models are mostly thawing if physical priors are used.

Comparing this model with the available data, we get figures 2.3, 2.4 and 2.5 for different comparisons between fine-structure constant measurements, cosmological measurements and the combined dataset in the same way as done on the previous analysis for the constant equation of state case. As seen in figure 2.3, we find again a preference for a non-zero coupling ζ for the Webb et al. (2011) but compatible with a null result at a two sigma level and the recent dedicated measurements fully compatible with the null result. The atomic clock constraint remains a tighter constrain than the astrophysical measurements.

Following the same line of thought of the previous analysis, the combination of all measurements provides a tighter constraint and in comparison to the constant equation of state case we find similar results. This similiarity comes from the fact that the atomic clock bound is only sensitive to the present value of dark energy equation of state and dominant over the remaining measurements.

From the marginalized likelihood function, we confirm that for the Webb et al. (2011) data there is a one sigma preference for a non zero coupling ζ while the best fit for the remaining datasets is a null result. The full dataset allows a two-sigma bound on ζ of

$$\zeta_{SGZ} = (0.2^{+1.5}_{-1.0}) \times 10^{-6} \qquad (95.4\% CL) \tag{2.6}$$

that leads to a Eötvös parameter of

$$|\eta_{SGZ}| < 2.9 \times 10^{-15} \qquad (95.4\% CL). \tag{2.7}$$

The bound on ζ is slightly weaker than the constrain found on the previous analysis for the constant equation of state case. The physical explanation for this outcome is that in a thawing model with a given w_0 the amount of α variation at a given non-zero redshift will be slightly smaller than in a constant equation of state model with the same w_0 value. Nevertheless, our indirect WEP bound is stronger than the available direct bounds (eq. 1.3 and 1.4).

Regarding the 1D constraint for the present value of dark energy equation of state by marginalizing

over the coupling, we find the three-sigma level

$$w_0 = -1.000^{+0.066}_{-0.034} \qquad (99.73\% CL) \tag{2.8}$$

which is slightly stronger than the bound found on the previous case of a constant equation of state. Note that the cosmological measurements alone constrain at a two-sigma level $-1.032 < w_0 < -0.932 (95.4\% CL)$ so the α data significantly improves this result. Therefore this is a strong constrain but that should be taken cautiously given the assumptions made on the cosmological parameters and because the likelihood is not Gaussian near the minimum which questions the choice of priors, taken into consideration in the following case.

In comparison with our previous results (Martins et al. (2015)), the constraints are slightly stronger as new tight measurements were considered (see appendix B).

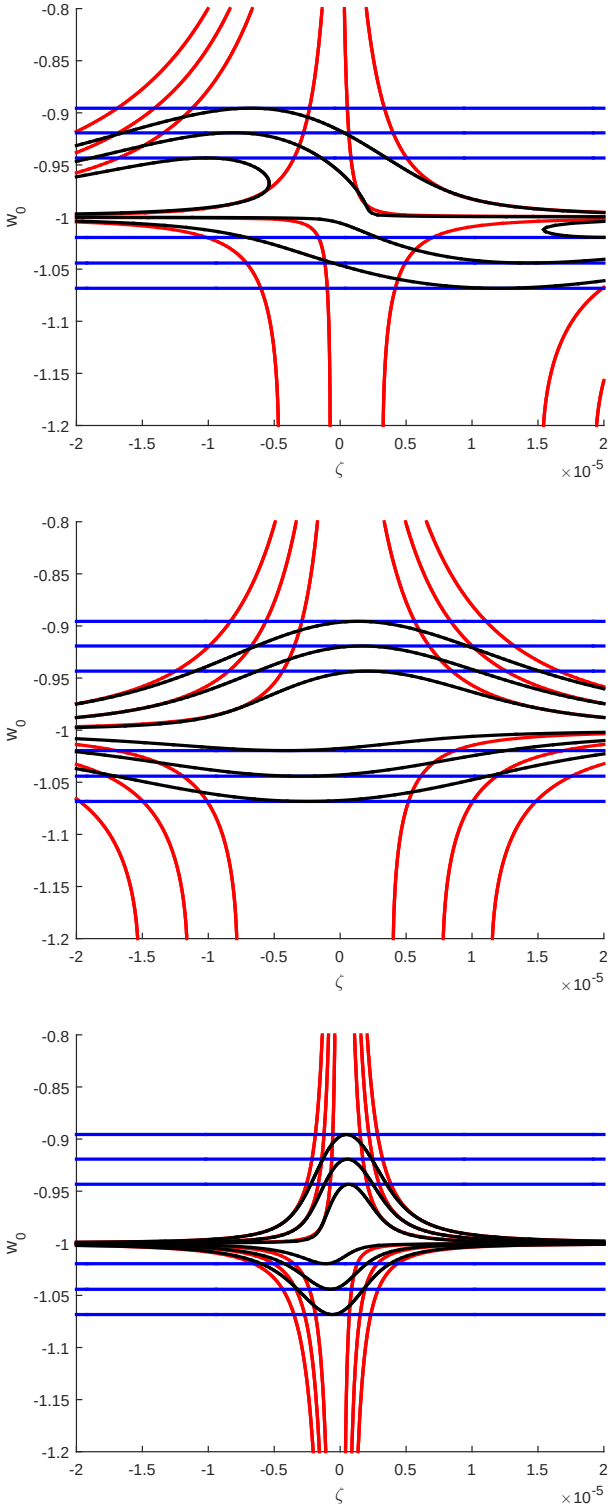

Figure 2.3: Two-dimensional likelihood contours for the Slepian et al. (2014) model with the one, two and three sigma constrains in the $\zeta - w_0$ plane with red for the α measurements, blue the cosmological datasets and black for the combined dataset. The red lines in the top panel corresponds to the Webb measurements, in the middle to recent dedicated measurements and in the bottom panel to the atomic clock measurement.

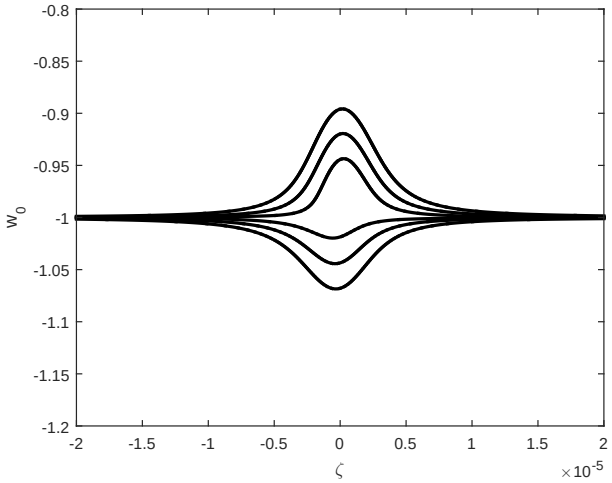

Figure 2.4: Two-dimensional likelihood contours for the Slepian et al. (2014) model with the one, two and three sigma constrains in the $\zeta - w_0$ plane for all the measurements combined.

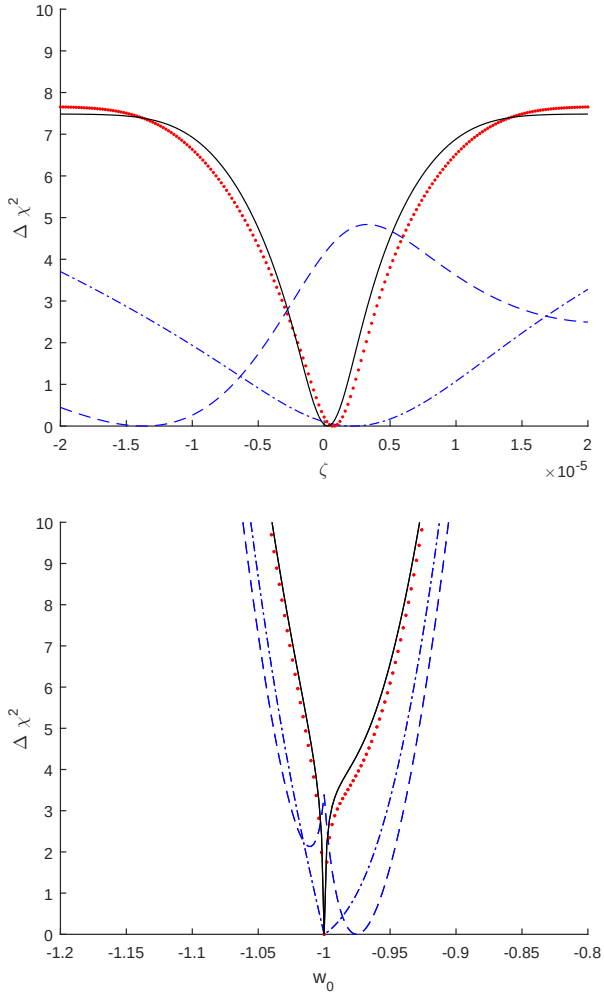

Figure 2.5: One-dimensional likelihood contours for the Slepian et al. (2014) model marginalizing over the other parameter: for ζ on the top panel and for w_0 using cosmological and Webb data (blue dashed), cosmological and dedicated measurements of α (blue dash-dotted), cosmological and atomic clocks (red dotted) and the combination of all datasets (black solid).

A class of freezing models

Now we will consider the opposite scenario, where the dark energy equation of state evolves towards -1, that is a freezing model. In many dilaton-type models the scalar field depends logarithmically on the scale factor as $\phi(z) \propto \log(1+z)$ which is our main motitvation. As we are assuming a linear gauge kinetic function, it leads to a variation of α as $\frac{\Delta\alpha}{\alpha}(z) \propto ln(1+z)$. We will calculate the condition on the dark energy equation of state for Class I models (see chapter 1) to have this $\alpha(z)$ behaviour but note that some Class II models also exhibit the same behaviour.

From equation 1.22, we take the funcion inside the square root as constant, which means

$$\Omega_\phi[1+w(z)] = const.; \tag{2.9}$$

which can be reshaped into the form

$$\frac{dw}{dz} = -3(1+w_0)\frac{w}{1+z}\left[\frac{1+w}{1+w_0} - \Omega_{\phi 0}\right]. \tag{2.10}$$

The initial condition for the first derivative is

$$\left[\frac{dw}{dz}\right]_{z=0} = -3\Omega_m w_0(1+w_0), \tag{2.11}$$

and the second derivative initial condition can be written as

$$\left[\frac{d^2w}{dz^2}\right]_{z=0} = 3\Omega_m w_0(1+w_0)[1+3w_0+3\Omega_m(1+w_0)], \tag{2.12}$$

so we have $w' \approx 3\Omega_m(1+w_0)$ and $w'' \approx 6\Omega_m(1+w_0)$ near the standard cosmological ΛCDM limit. Integrating the above equation leads to the solution,

$$w_{dil}(z) = \frac{[1-\Omega_\phi(1+w_0)]w_0}{\Omega_m(1+w_0)(1+z)^{3[1-\Omega_\phi(1+w_0)]} - w_0} \tag{2.13}$$

where we still make the assumption $\Omega_m + \Omega_\phi = 1$. The explicit form for the Friedmann equation is

$$\frac{H^2(z)}{H_0^2} = \Omega_m(1+z)^3 + \frac{\Omega_\phi}{\Omega_m(1+w_0) - w_0}\left[\Omega_m(1+w_0)(1+z)^3 - w_0(1+z)^{3\Omega_\phi(1+w_0)}\right] \tag{2.14}$$

and the evolution of α is simply

$$\frac{\Delta\alpha}{\alpha}(z) = \zeta\sqrt{3\Omega_\phi(1+w_0)}ln(1+z). \tag{2.15}$$

As previously discussed, the analysis with a flat prior on $1 + w_0$ may be too simplistic. Since in these models one expects that $w_0 \geq -1$, we will remove the phantom part of this parameter, and use this model to test the effects of choice of priors. Therefore we will assume a logarithmic prior, and figure 2.6 reports the results for each α datasets, cosmological data and their combination. There is again a one-sigma preference for a non-zero coupling for the Webb et al. (2011) data while the remaining α measurements are compatible with the null result.

Figures 2.6 and 2.7 definitely show that for a sufficiently close value of w_0 to -1 any value of the coupling ζ would be allowed. In principle that would also happen according to equation 1.22 in the orthogonal direction (for a small ζ any w_0 would be allowed) but the strong priors on w_0 from the cosmological datasets prevent that this from happening.

The 1D marginalized likelihoods are given in figure 2.8 and the bounds for the dark energy equation of state

$$w_0 < -0.954 \qquad (99.73\%CL) \tag{2.16}$$

at three-sigma confidence level (for comparision, the cosmological data alone yield $w_0 < -0.92$), while on the coupling parameter at one-sigma confidence level we get

$$\zeta_{DIL} = 0.4^{+4.2}_{-3.7} \times 10^{-6} \qquad (68.3\%CL). \tag{2.17}$$

and at the two-sigma level we have $\zeta_{DIL} = 0.4^{+19}_{-16} \times 10^{-6}(95.4\%CL)$. Transforming into WEP bounds we have a still stronger constrain than the direct ones with a one-sigma level

$$|\eta_{DIL}| < 2.1 \times 10^{-14} \qquad (68.3\%CL). \tag{2.18}$$

Though our constraints display some model dependence in class of models and also on the underlying priors, we conclude that they are generically competitive with other tests of these models. These

constraints are also stronger than our previous results (Martins et al. (2015)).

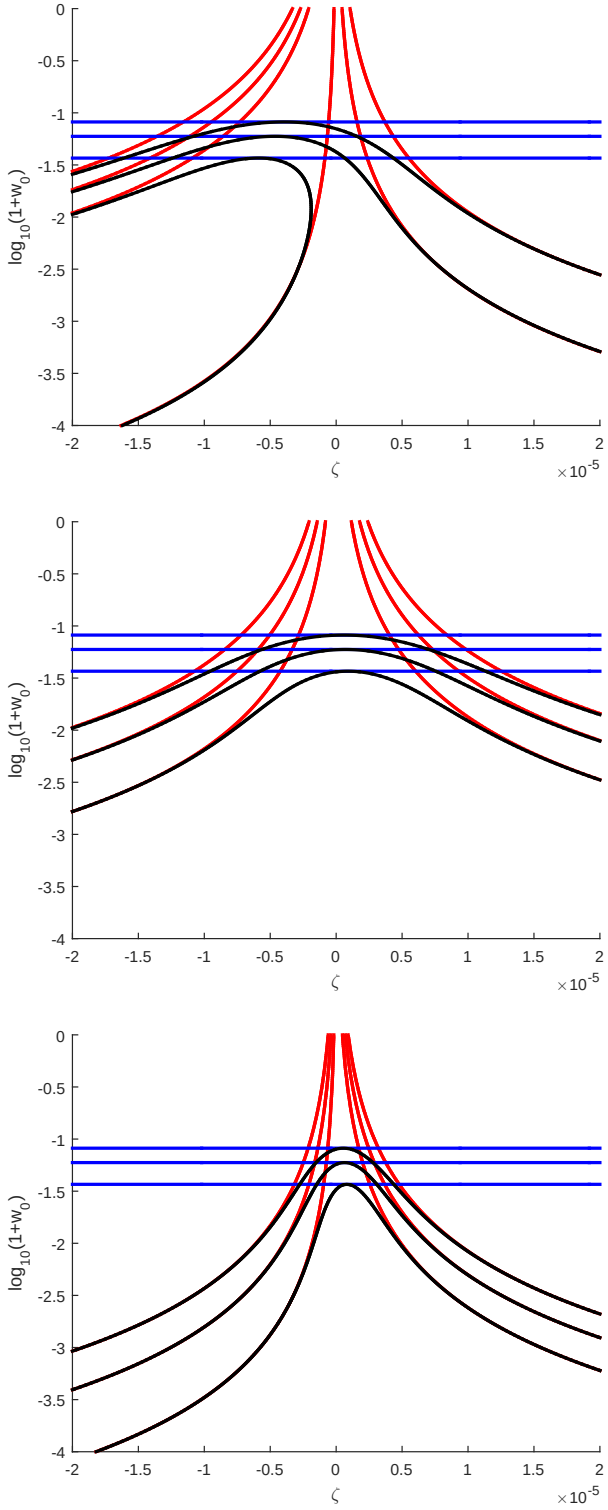

Figure 2.6: Two-dimensional likelihood contours for the dilaton model with the one, two and three sigma constrains in the $\zeta - w_0$ plane with red for the α measurements, blue the cosmological datasets and black for the combined dataset. The red lines in the top panel corresponds to the Webb measurements, in the middle to recent dedicated measurements and in the bottom panel to the atomic clock measurement.

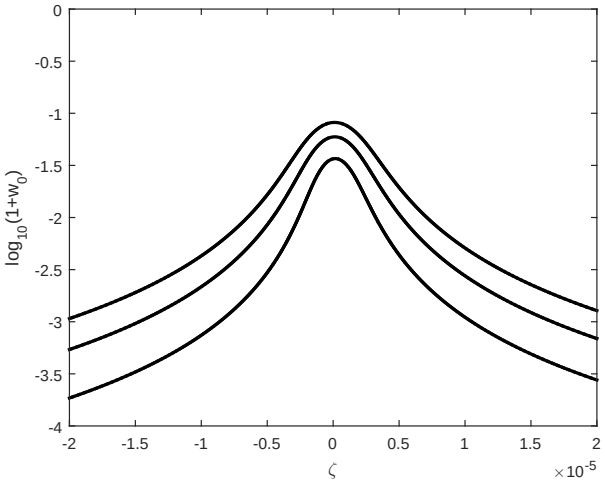

Figure 2.7: Two-dimensional likelihood contours for the dilaton model with the one, two and three sigma constrains in the $\zeta - w_0$ plane for all the measurements combined.

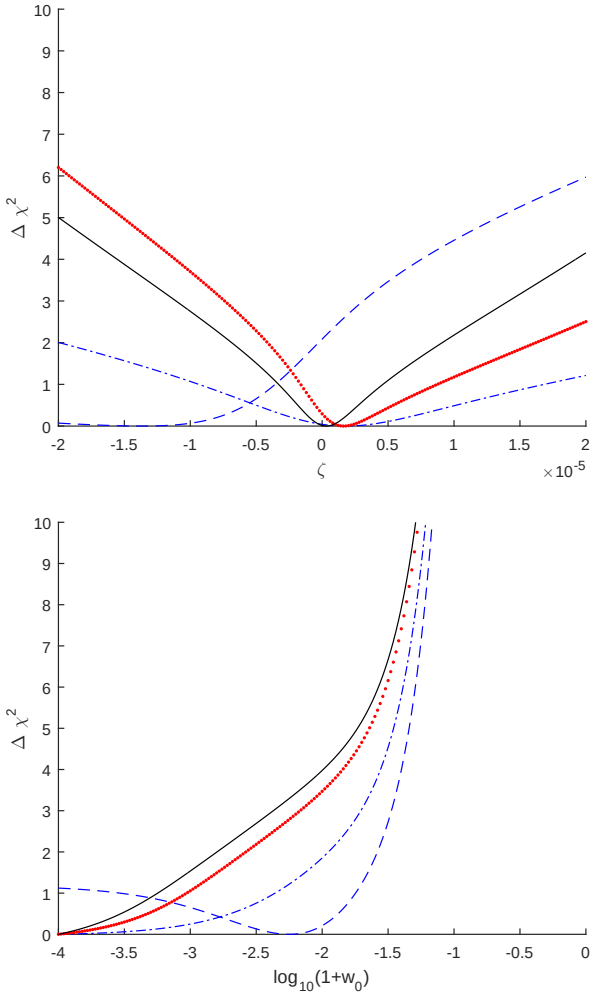

Figure 2.8: One-dimensional likelihood contours for the dilaton model: for ζ (marginalizing over w_0) on the top panel and for w_0 (marginalizing over ζ) using cosmological and Webb data (blue dashed), cosmological and dedicated measurements of α (blue dash-dotted), cosmological and atomic clocks (red dotted) and the combination of all datasets (black solid).

Including the Oklo bound

The Oklo natural nuclear reactor can provide a complementary probe of stability of fundamental constants. Particularly, it provides a strong constraint on α if one assumes that nothing else is varying. This is a very poor assumption that is documented in the literature (for a discussion see Davis et al. (2014)). As this is not as reliable as the atomic clock or QSO measurements, we have not used it previously. Yet we clarify the effect it would have on our analysis by including the constrain of Petrov et al. (2006), with an effective redshift $z_{Oklo} = 0.14$, as

$$\frac{\Delta\alpha}{\alpha} = (0.5 \pm 6.1) \times 10^{-8}. \tag{2.19}$$

Including this bound in our analysis on subsection 2.2.1 should have a larger relative effect since in thawing models the deviations from $w = -1$ are larger at low redshift whereas in freezing models like the analysis on subsection 2.2.2, the impact will be smaller.

Figures 2.9 and 2.10 show the two dimensional likelihood contours with and without the Oklo bound and table 2.1 the best-fit values obtained. The effects of the addition of the Oklo constrain are perceptible but not striking because this bound is at very low redshift and only a factor 3 stronger than the atomic clock constraint so a reasonable fraction of models that fit the latter constraint will fit the former.

Parameter	Confidence level	Without Oklo	With Oklo
Coupling	95.4%	$\zeta_{SGZ} = 0.2^{+1.5}_{-1.0} \times 10^{-6}$	$\lvert\zeta_{SGZ}\rvert = (0.2 \pm 3.4) \times 10^{-6}$
Eötvös	95.4 %	$\eta_{SGZ} < 2.9 \times 10^{-15}$	$\eta_{SGZ} < 1.3 \times 10^{-14}$
equation of state	99.7 %	$w_0 = -1.000^{-0.066}_{-0.034}$	$w_0 = -1.000^{-0.064}_{-0.032}$

Table 2.1: Obtained constrains for the Slepian et al. (2014) model for different parameters using all datasets combined with and without the Oklo bound.

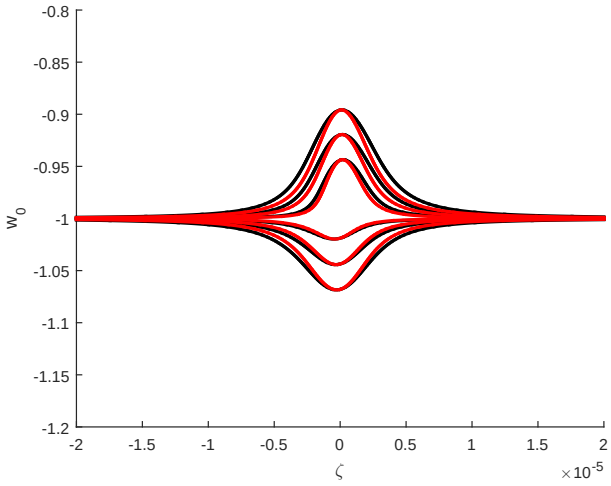

Figure 2.9: Two-dimensional likelihood contours on the $\zeta - w_0$ plane with one, two and three sigma levels for all datasets combined with the Oklo bound in red and without in black.

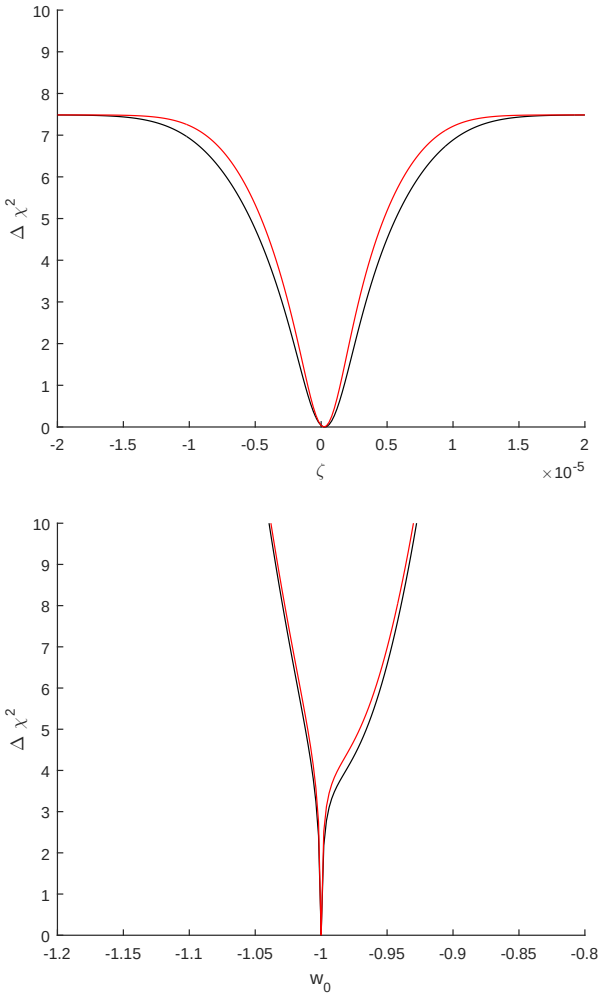

Figure 2.10: One-dimensional likelihood contours for ζ on the left panel and for w_0 on the right panel with one, two and three sigma level for all datasets combined with the Oklo bound in red and without in black.

2.3 TWO PARAMETERS REDSHIFT-DEPENDENT EQUATION OF STATE

Previously we have considered dark energy equations of state with one parameter only, its present value w_0, with or without redshift dependence. Now we will explore the addition of a free parameter such as the Chavalier-Polarsky-Linder parametrization and the Early Dark Energy model specify.

Chevalier-Polarsky-Linder parametrization

The Chavalier-Polarsky-Linder parametrization (Chevallier and Polarski (2001),Linder (2003)) has the following dark energy equation of state,

$$w_{CPL}(z) = w_0 + w_a \frac{z}{1+z} \tag{2.20}$$

where w_0 is its present value and w_a the coefficient of the time-dependent term. This redshift-dependent term allows possible variations from the standard ΛCDM without assuming a specific theory. Yet, we can assume that this kind of dark energy is produced by a scalar field which is coupled to the electromagnetic sector. The fraction of energy density is given by

$$\Omega_{CPL}(z) = \frac{1-\Omega_m}{1-\Omega_m+\Omega_m(1+z)^{-3(w_0+w_a)}e^{(3w_a z/1+z)}} \tag{2.21}$$

where Ω_m is the present matter density and a flat universe was assumed.

Using the cosmological data, the atomic clock bound and the astrophysical measurements of α, we obtain the one, two and three sigma contours for this parametrization as in figure 2.11. Degeneracies are distinctly visible and so is the unconstrained parameter w_a. That is not the case for w_0 and ζ since the cosmological data provide priors on the present value of dark energy equation of state and break the expected degeneracies with ζ. Figure 2.12 shows the 1D marginalized likelihood contours for each parameter. Note that the behaviour of the archival measurements and the recent dedicated α measurements clearly differs, as the former prefers a non zero variation that leads to a one sigma preference for a nonzero coupling ζ and the latter is compatible with the null result at a two sigma level, respectively. As previously seen, the atomic clock measurement is the most constraining one. In detail,

we get w_a *unconstrained*, while for the dark energy equation of state, the constraints at a one sigma level are weaker,

$$w_0 = -1.00 \pm 0.02 \qquad (68\% CL) \tag{2.22}$$

and for the coupling even tighter,

$$|\zeta| < 2 \times 10^{-6} \qquad (95.4\% CL) \tag{2.23}$$

that translated into WEP violation, becomes

$$|\eta| < 4 \times 10^{-15} \qquad (95.4\% CL). \tag{2.24}$$

In comparison with the previous analyses (Martins et al. (2015)), the constraint on w_0 becomes weaker as there is another free parameter though basically unconstrained. Regarding the coupling ζ, the constraints become tighter and consequently for the Eötvös parameter. This result is expected as the CPL equation of state allows larger possible variations of α and therefore the current data impose a tighter constraint on the coupling ζ.

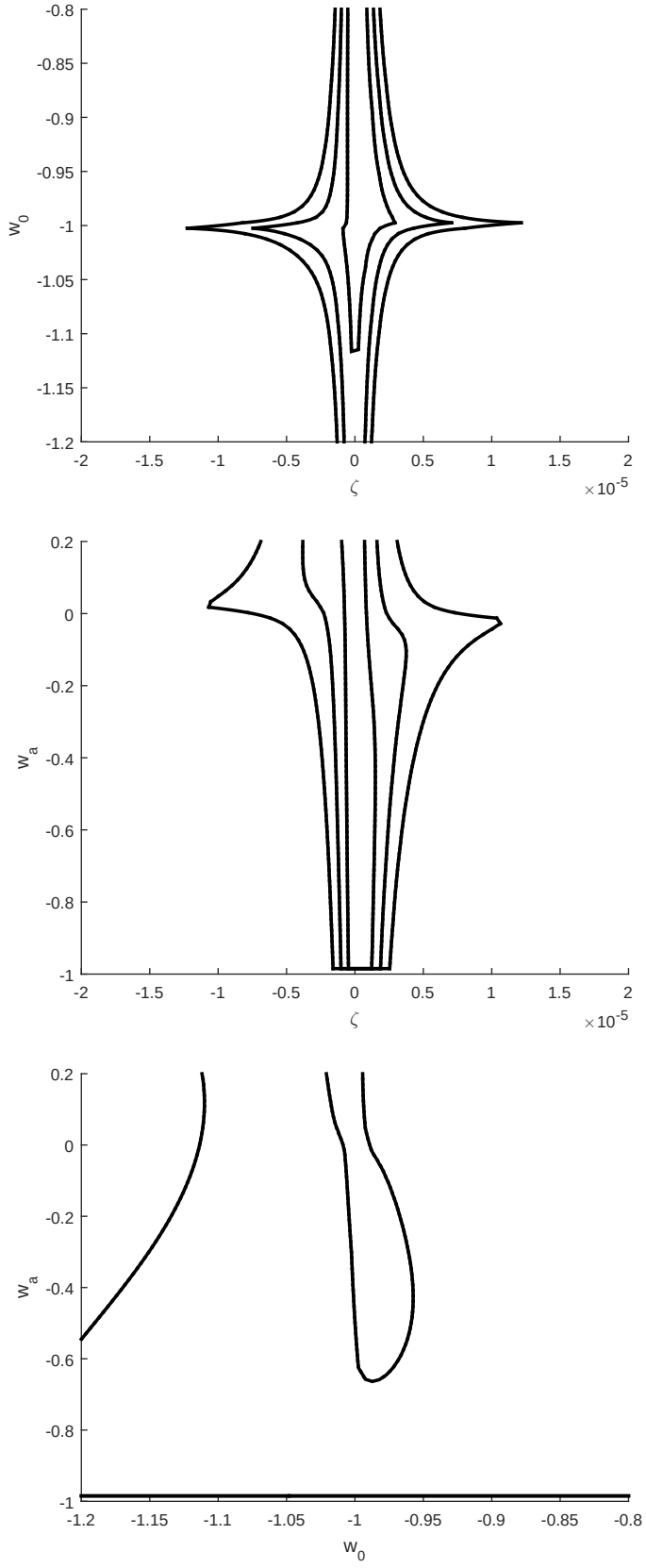

Figure 2.11: Two-dimensional likelihood contours for the CPL parametrization using all data combined. On the top panel is the $\zeta - w_0$ plane, $\zeta - w_a$ in the middle and $w_0 - w_a$ on the bottom panel marginalizing the remaining parameter. The contours correspond to the one, two and three sigma constraints.

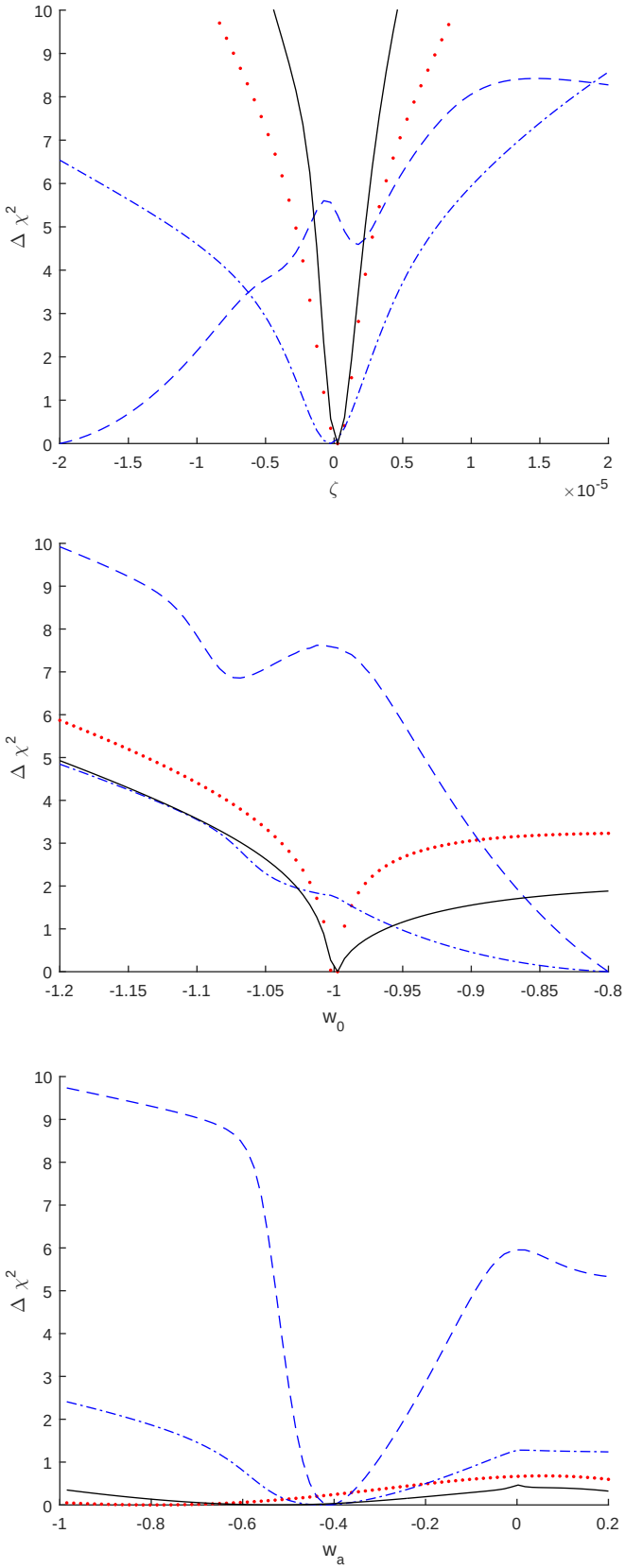

Figure 2.12: One-dimensional likelihood contours for the CPL parametrization using all data combined. From the top to the bottom panel are the one, two and three sigma constraints for ζ, w_0 and w_a parameter, marginalizing the remaining parameters.

Early Dark Energy model

For the Early Dark Energy model (EDE) (Doran and Robbers (2006)), the dark energy equation of state is

$$w_{EDE}(z) = -\frac{1}{3[1-\Omega_{EDE}(z)}\frac{d\ln\Omega_{EDE}(z)}{d\ln a} + \frac{a_{eq}}{3(a+a_{eq})} \tag{2.25}$$

and the dark energy density factor is

$$\Omega_{EDE}(z) = \frac{1-\Omega_m-\Omega_e[1-(1+z)^{3w_0}]}{1-\Omega_m+\Omega_m(1+z)^{-3w0}} + \Omega_e[1-(1+z)^{3w_0}] \tag{2.26}$$

where a_{eq} is the scale factor of matter-radiation equality, which we will translate and use $z_{eq} = 3371$ from the Planck colaboration (2015) results. The energy density evolves with time approaching a finite constant Ω_e in the past, instead of zero as for the CPL case. Also here a flat universe is assumed.
The equation of state has an adaptative behaviour as it matches the dominant component at each cosmic time, with w_0 for its present value, $w_{EDE} \approx 1/3$ and $w_{EDE} \approx 0$ for when radiation and matter dominates. Although this is a phenomenological parametrization, we will assume that this kind of dark energy is given by a scalar field that couples with the electromagnetic sector, as done for the CPL case.
Figure 2.13 stems from our analysis of this model representing the 2D likelihood contours for each pair of parameters, assuming flat priors. Here is also evident the correlation between ζ and w_0, a feature also present regarding Ω_e. We obtain the 1D constraints plotted on figure 2.14, where Ω_e is unconstrained. For the remaining parameters, we obtain for the present value of dark energy equation of state

$$w_0 = -0.90 \pm 0.02 \qquad (95.4\% CL) \tag{2.27}$$

and for the coupling

$$|\zeta| < 2.3 \times 10^{-6} \qquad (95.4\% CL) \tag{2.28}$$

that translated is

$$|\eta| < 5.3 \times 10^{-15} \qquad (95.4\% CL). \tag{2.29}$$

The constraints on the dark sector are slightly stronger than for the CPL case, corresponding to a slightly weaker constraints on the coupling ζ.

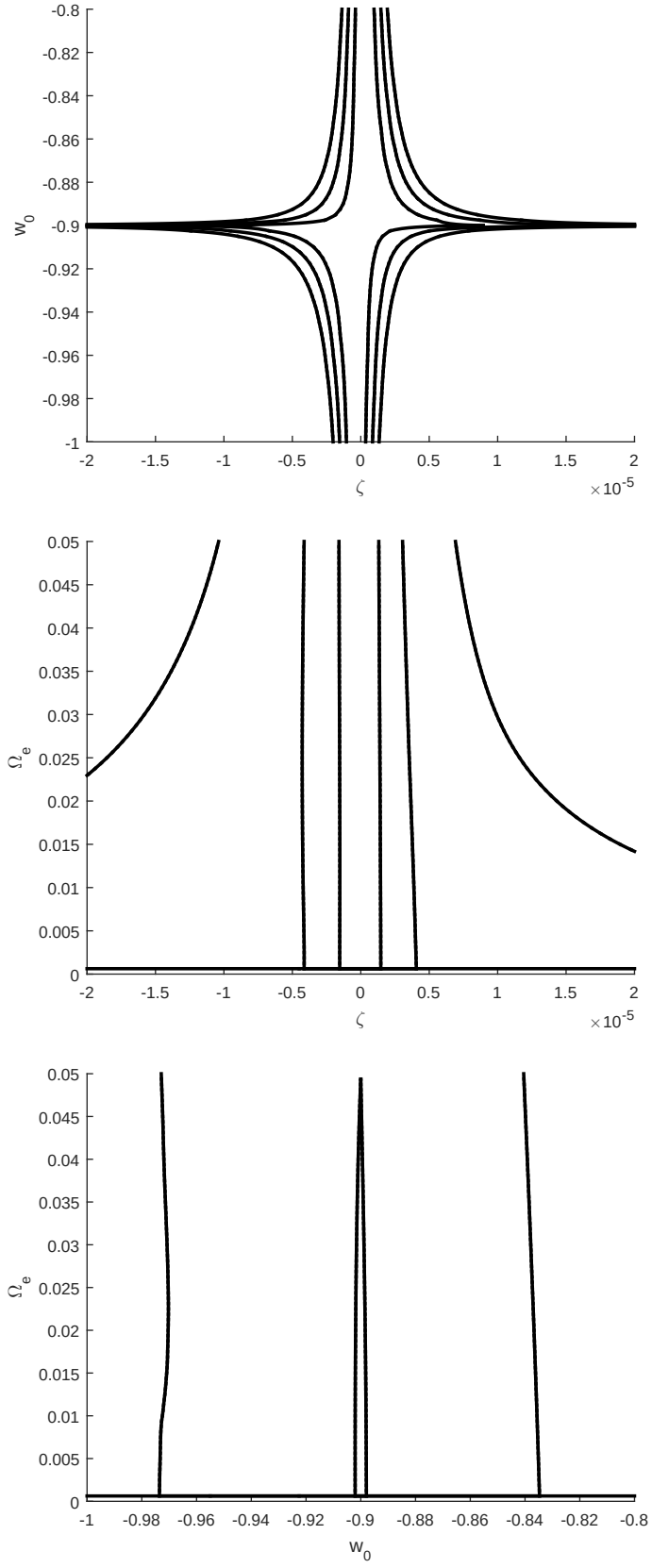

Figure 2.13: Two-dimensional likelihood contours for the EDE model parametrization using all data combined. On the top panel is the $w_0 - w_a$ plane, $w_0 - \zeta$ in the middle and $w_a - \zeta$ on the bottom panel marginalizing the remaining parameter. The contours correspond to the one, two and three sigma constraints.

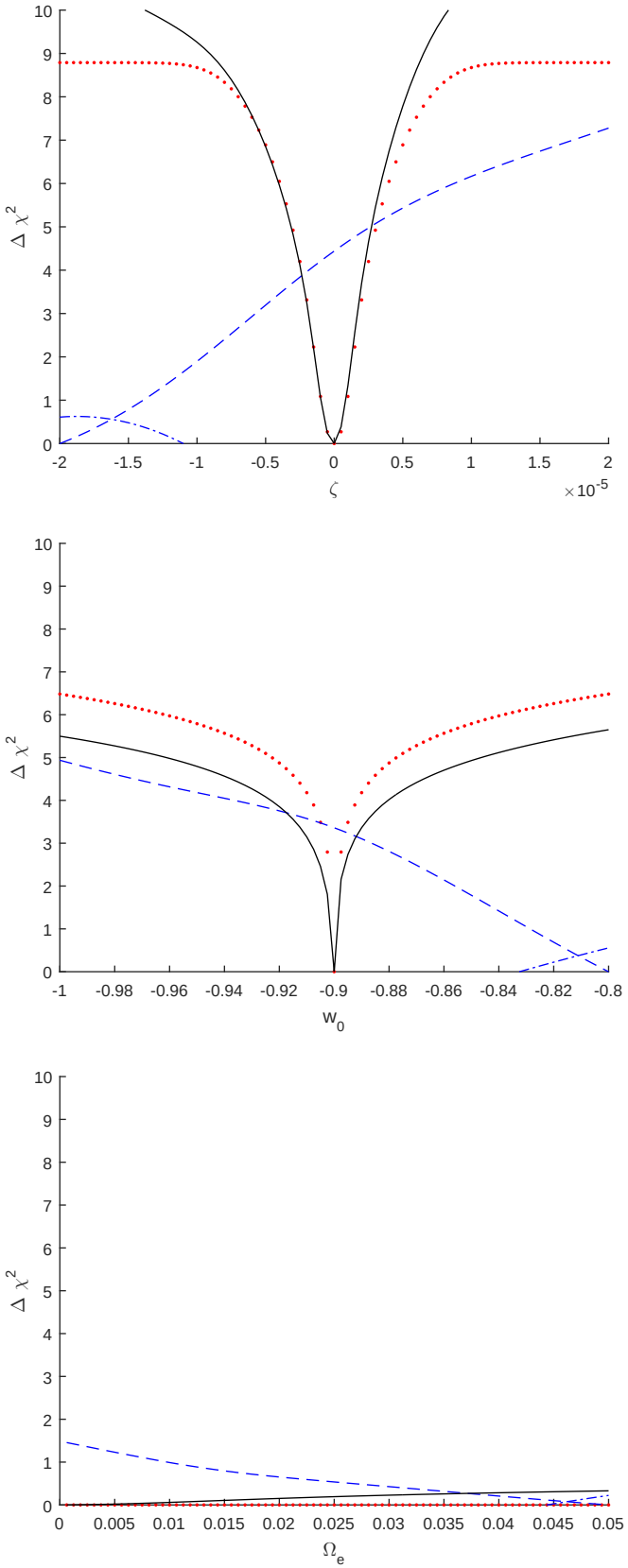

Figure 2.14: One-dimensional likelihood contours for the EDE parametrization using all data combined. From the top to the bottom panel are the one, two and three sigma constraints for ζ, w_0 and Ω_e parameter, marginalizing the remaining parameters.

Chapter 3.

Dipole variation and data consistency tests

3.1 DIPOLE VARIATION

The analysis by Webb et al. (2011) and King et al. (2012) of the archival dataset of the fine structure constant measurements (see appendix B) has found evidence for a spatial variation at the parts per million level. This analysis also points out that a pure spatial dipole is a good fit to these measurements with a statistical significance of over four standard deviations, a result confirmed by other authors as well.

The compilation of recent dedicated measurents of the fine structure constant (see table B.2) with typically smaller systematical uncertainties motivates a new analysis to assess whether a dipole is still a good fit to the data. Though there are suggestions of underestimated systematics, we simply take the published values at face value and compute each uncertainty as the systematical and statistical uncertainties added in quadrature.

To check that we recover the previously published results, in a first step we will consider the archival dataset on its own and then combine it with the smaller dataset of dedicated measurements.

Pure spatial dipole variation

In the simplest case, the relative variation of α is given by

$$\frac{\Delta\alpha}{\alpha}(A,\Psi) = Acos\Psi \tag{3.1}$$

where A is the amplitude and Ψ is the orthodromic distance between the Declination and Right Ascension of the i-th measurement (θ_i, ϕ_i) and the north pole (θ_0, ϕ_0) which can be found by

$$cos\Psi = sin\theta_i sin\theta_0 + cos\theta_i cos\theta_0 cos(\phi_i - \phi_0). \tag{3.2}$$

This parametrization was considered in all previous analyses of this archival dataset which serves as a simple test. We do not consider an additional monopole term because there is no strong statistical preference for it and because physically this term would be interpreted as due to the assumption of terrestrial isotopic abundances. This means that the monopole effect is not due to the physics of the quasar itself but an effect of using astrophysical measurements, without considering that the relative abundance of Mg^{24} is lower than on the Earth (for a discussion see Webb et al. (2014)).

To perform this analysis, we use the standard χ^2 techniques with a 200^3 grid considering the parameters amplitude, right ascension and declination of the north pole of the dipole, (A, θ_0, Ψ_0). We also choose a uniform prior for all three parameters and assumed a positive amplitude (A $\geq$ 0). Allowing negative values for the amplitude of the dipole leads to degenerate plots with two equally likely best-fit poles in two opposite points for a specific value.

The results for the pure spatial dipole can be found in table 3.1 and figures 3.1 and 3.2. For the archival data alone, we confirm the results of previous analyses. The addition of the new dedicated measurements changes significantly the outcome with a preference for a smaller non-zero amplitude and smaller corresponding uncertainty. The direction of the north pole in the sky does not change significantly. In comparison with our previous results (Pinho and Martins (2016)), the addition of recent measurements to the ones used before lead to a weaker evidence for a pure spatial dipole variation as the amplitude is smaller.

Dataset & c.l.	Amplitude (*ppm*)	Right Ascension (*h*)	Declination (°)
Webb *et al.* (68.3%)	9.2 ± 2.2	17.3 ± 1.0	-61 $^{+10}_{-11}$
Webb *et al.* (99.7%)	9.2 ± 6.4	$17.3^{+4.7}_{-5.6}$	< -27
All data (68.3%)	6.1 ± 1.8	16.3 $^{+1.0}_{-1.1}$	-58 $^{+8}_{-9}$
All data (99.7%)	6.1 $^{+5.2}_{-5.6}$	16.3 $^{+4.9}_{-7.2}$	< -32

Table 3.1: 1σ and 3σ constrains on the free parameters for a pure spatial dipole.

Redshift dependent spatial dipole variation

We also consider an implicit time dependence by assuming a logarithmic dependence on redshift *z* which takes the form as

$$\frac{\Delta\alpha}{\alpha}(A, z, \Psi) = Aln(1+z)cos\Psi. \tag{3.3}$$

This redshift dependence is typical of models with dilaton scalar fields as described in section 2.2.2. Previous analyses have considered a dependence on look-back time but this has the disadvantage of requiring a specific choice of cosmological parameters and it is not clear how this dependence would arise in realistic varying-α models. Also, choosing this parametrization holds the same number of free parameters.

Applying the same χ^2 techniques, grid size and flat priors, we obtained the results for a dipole variation with a redshift dependence as illustrated by table 3.2 figures 3.3 and 3.4. The statistical preference non-zero amplitude remains with a slightly higher value. There is also a increase on the uncertainties for each parameter relatively to the ones found for the case of a pure dipole variation. In agreement with previous works, we find that the current data cannot strongly distinguish the two considered parametrizations that represent different classes of models.

Dataset & c.l.	Amplitude (*ppm*)	Right Ascension (*h*)	Declinarion (°)
Webb *et al.* (68.3%)	9.6 $\pm$ 2.4	17.3 $\pm$ 1.0	-61 $^{+11}_{-12}$
Webb *et al.* (99.7%)	9.6 $\pm$ 6.9	$17.3^{+5.6}_{-6.4}$	< -27
All data (68.3%)	6.3 $\pm$ 1.9	16.3 $^{+1.0}_{-1.2}$	-61 $^{+10}_{-11}$
All data (99.7%)	6.3 $\pm$ 5.7	16.3 $^{+6.2}_{-9.4}$	< -30

Table 3.2: 1σ and 3σ constrains on the free parameters for a spatial dipole with redshift dependence.

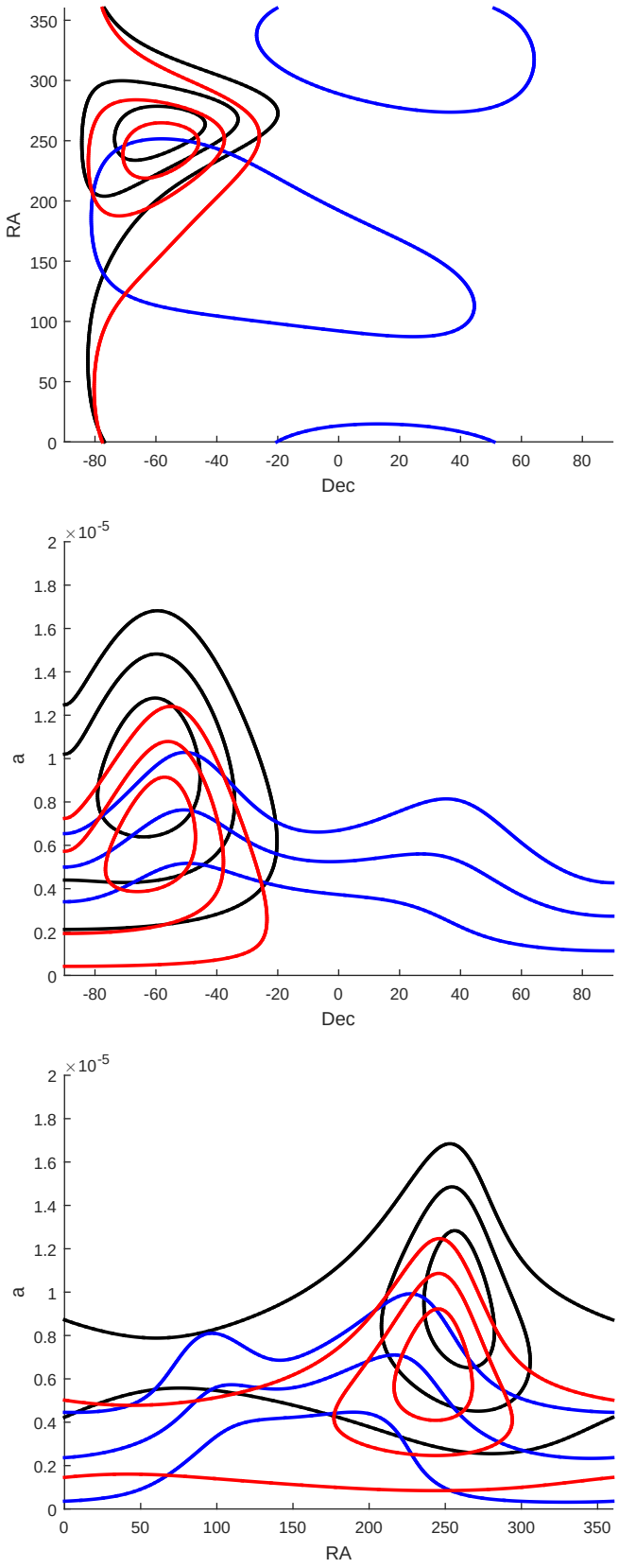

Figure 3.1: Two-dimensional likelihood contours for a pure spatial dipole parametrization. Webb *et al.* dataset in black, recent measurements in blue and all data in red.

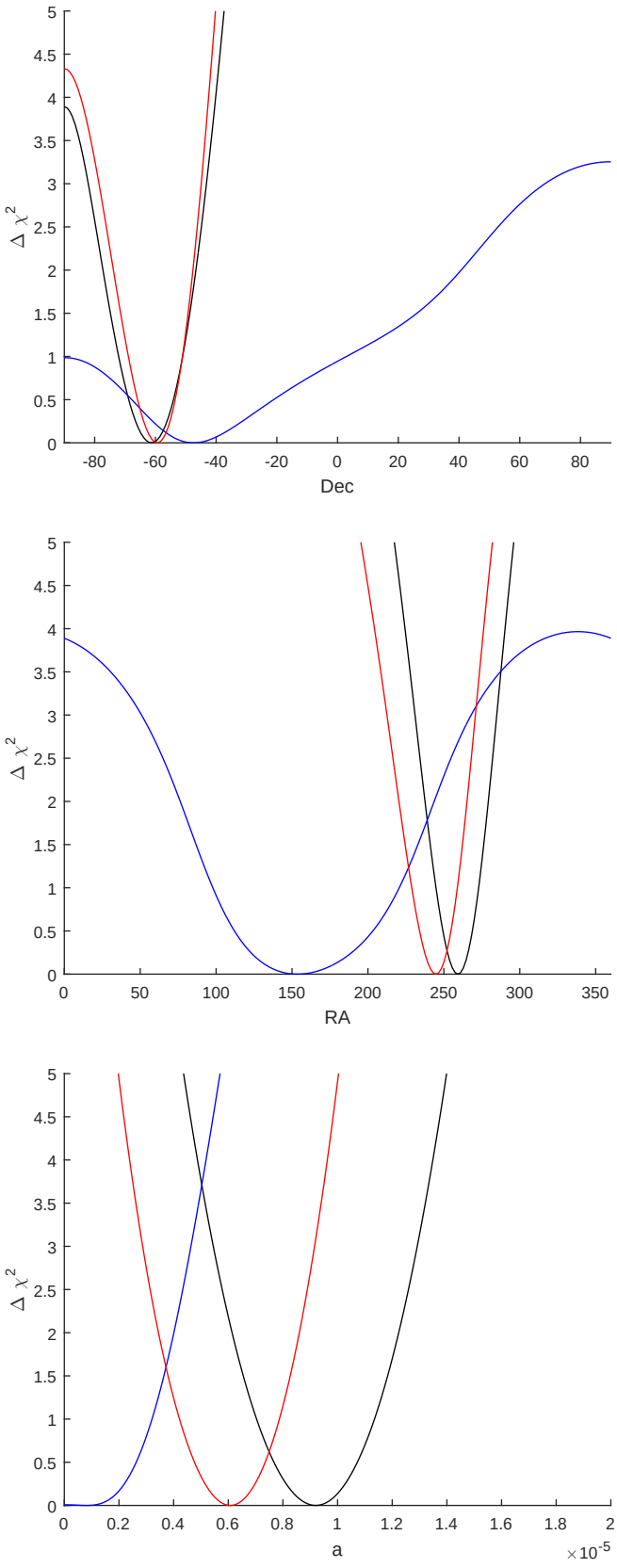

Figure 3.2: One-dimensional likelihood contours for a pure spatial dipole parametrization. Webb *et al.* dataset in black, recent measurements in blue and all data in red.

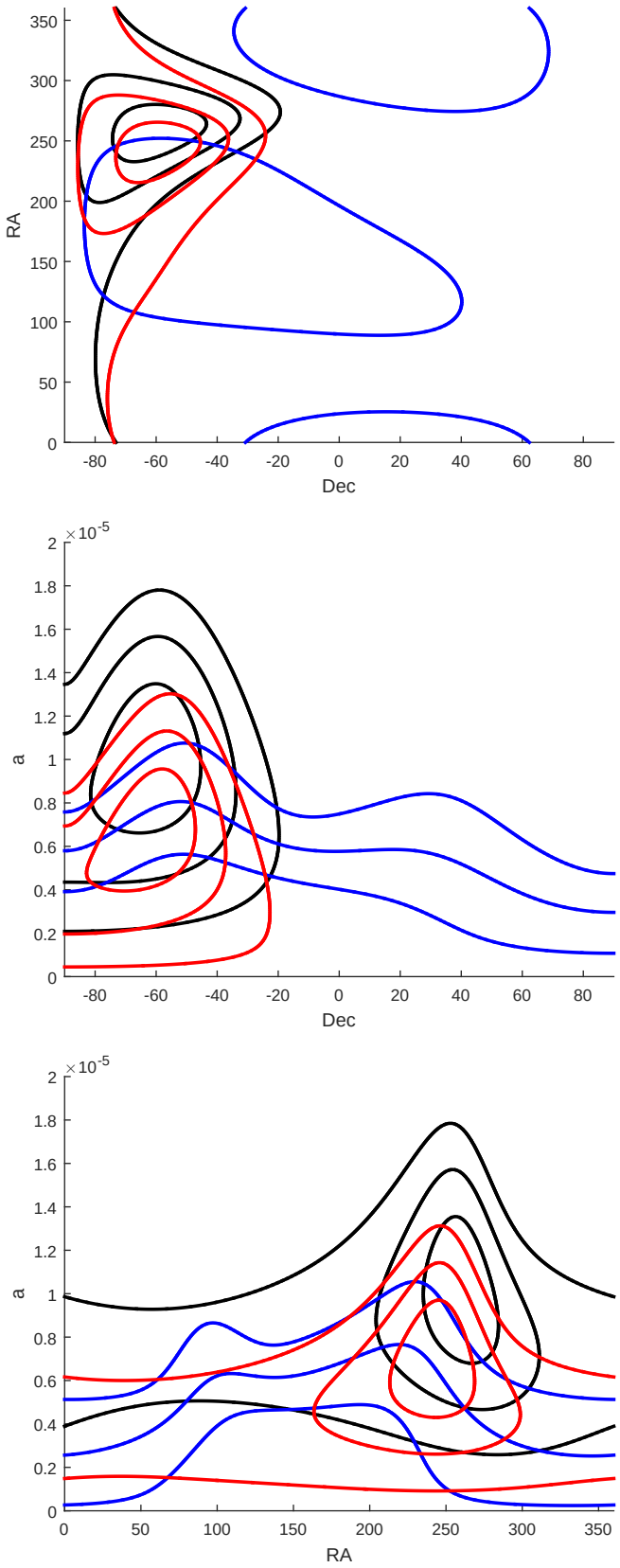

Figure 3.3: Two-dimensional likelihood contours for a spatial dipole with redshift dependence parametrization. Webb *et al.* dataset in black, recent measurements in blue and all data in red.

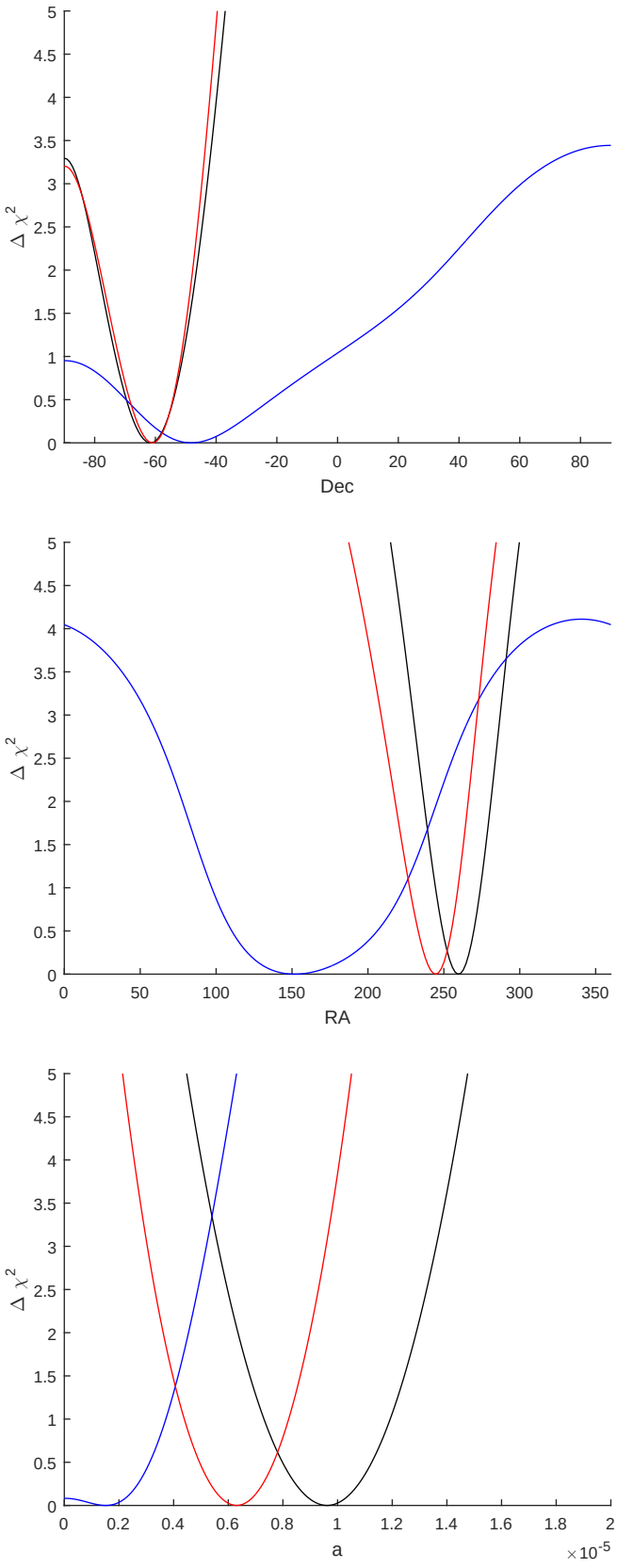

Figure 3.4: One-dimensional likelihood contours for a spatial dipole with redshift dependence parametrization. Webb *et al.* dataset in black and all data in red.

3.2 DATA CONSISTENCY TESTS

Further data available and the updated constrains on spatial variations of the fine structure constant can be used in consistency tests. Previous analyses (Ferreira et al. (2012), Ferreira et al. (2014), Ferreira et al. (2015)) have used fundamental constants measurements (for example, proton-electron mass ratio μ or combined measurements of α, μ and the proton g-factor g_p) to constrain a broad class of unification scenarios. We will extend the data used on previous analyses to constraint a relation between fundamental couplings as predicted by the same class of grand unification models. Note that this analysis will include all the available measurements of each fundamental constant, the archival dataset (table B.3) and the dedicated measurements (table B.2 for α, table C.1 for μ and tables D.1 and D.2).

Consistency tests

It is known that fundamental couplings run with energy (Martins (2002), Uzan (2011)). Any Grand-Unified theory predicts a specific relation between fundamental couplings. As this relation will be highly model-dependent, its measurements can therefore provide key consistency tests (Ferreira et al. (2012)).

The simplest way to use simultaneous variations of several fundamental couplings is to relate their specific variations to a particular dimensionless one, in this case, the fine structure constant α. If one writes $\alpha = \alpha_0(1 + \delta_\alpha)$ and the variation of the combination of couplings as

$$\frac{\Delta X}{X} = k_X \frac{\Delta \alpha}{\alpha} \tag{3.4}$$

we have $X = X_0(1 + k_X \delta_\alpha)$ and so forth, for each fundamental coupling.

Our combined measurements are from the fine structure constant α, the proton-electron mass ratio μ and g-factor g_p so we can use them explicitly through the expression

$$\frac{\Delta Q}{Q} = \lambda_\alpha \frac{\Delta \alpha}{\alpha} + \lambda_\mu \frac{\Delta \mu}{\mu} + \lambda_g \frac{\Delta g}{g} \tag{3.5}$$

where the couplings $\lambda_\alpha, \lambda_\mu$ and λ_g will be model-dependent.

We assume the simplest case where the relation between the variation of the couplings is given by

$$\frac{\Delta\mu}{\mu} = P\frac{\Delta\alpha}{\alpha}, \qquad \frac{\Delta g_p}{g_p} = Q\frac{\Delta\alpha}{\alpha} \tag{3.6}$$

where P and Q are as free parameters. We take the usual χ^2 techniques aforementioned to constrain these parameters by taking all the available measurements of each fundamental constant. For a grid size of 1000^3, we compute the variation for μ and $\frac{\Delta Q}{Q}$ taking the all data of the variation of α as a prior and marginalizing over it, that is, the combination of the archival dataset (table B.3) and the dedicated measurements (table B.2. The results of this analysis are reported by figure 3.5 from which we obtained the constraints

$$P = -0.72^{+1.44}_{-1.32}\ (68.3\%\ c.l.) \qquad Q = 0.25^{+0.11}_{-0.17}\ (68.3\%\ c.l.). \tag{3.7}$$

As depicted by figure 3.5, the constraints are quite tight. With 68.3$\%$ confidence level, the best fit value for the Q parameter is a positive value but this preference is lost at 3σ level (99.7$\%$ confidence level). Though it is an approximation to use a constant relation between varying fundamental couplings, we can further study the case where α is given by a dipole variation. Also we can substitute the constant by a phenomenological parametrization such as the work by Coc et al. (2007), Luo et al. (2011) and Ferreira et al. (2015).

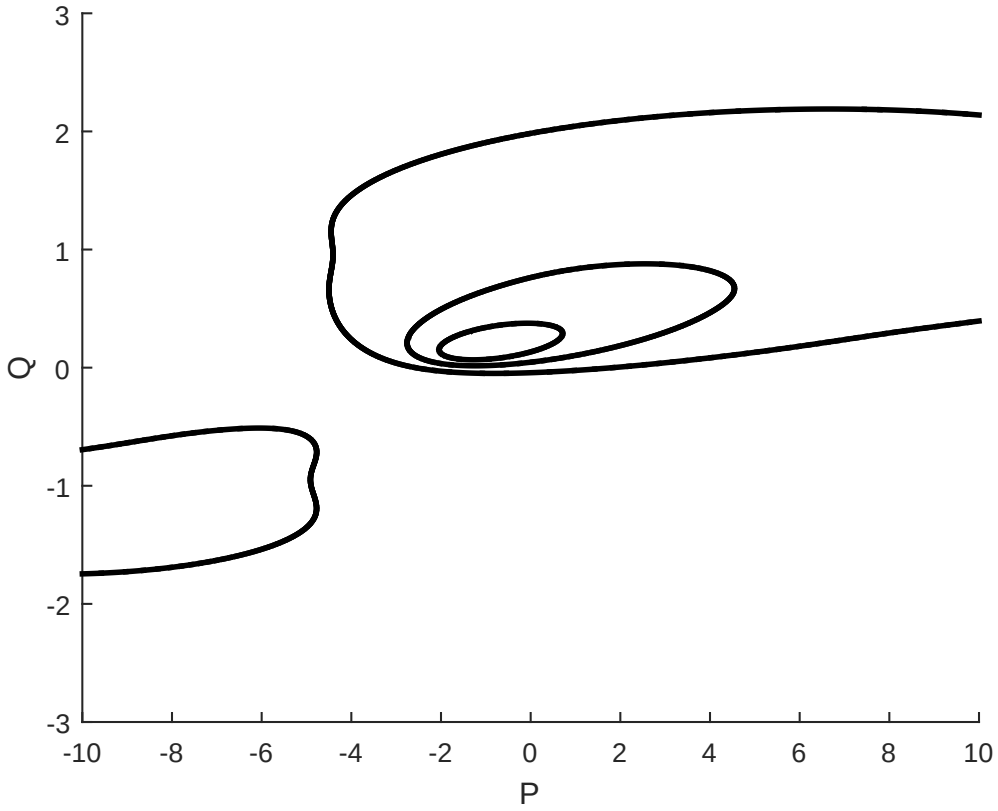

Figure 3.5: Two dimensional likelihood contours for the parameters (P, Q) using all datasets available combined.

Chapter 4.

Spatial variation

Another observational approach to constrain variations of the fine structure constant is to search for a spatial variation. For instance, one can compute the correlation function of the α measurements which can be easily related to a theoretical model, since we will only compare the statistical values of these measurements. This means that we will use a power spectrum analysis and, since we are working on a sphere, we will expand the spatial correlation of α measurements in spherical harmonics.

4.1 OBSERVED ANGULAR POWER SPECTRUM

Spherical harmonics can be defined as (Bonometto et al. (1997))

$$Y_{\ell m}(\theta,\phi) = \sqrt{\frac{2\ell+1}{4\pi}\frac{(\ell-m)!}{(\ell+m)!}} P_\ell^m(cos\theta) exp[im\phi] \tag{4.1}$$

where $\ell > 0$ and $|m| \leq \ell$ are integers and P_ℓ^m are the associated Legendre functions. These functions form a set of orthonormal functions on a sphere, meaning

$$\int Y_{\ell m} Y^*_{\ell' m'} d\Omega = \delta_{\ell\ell'}\delta_{mm'} \tag{4.2}$$

with $\delta_{\ell\ell'}$ corresponding to the Kronecker delta. One can expand any square integrable function $\Delta(\theta,\phi)$ (in this case $\frac{\Delta\alpha}{\alpha}(RA,Dec)$) as

$$\Delta(\theta,\phi)=\sum_{\ell=0}^{\infty}\sum_{m=-\ell}^{\ell}a_{\ell m}Y_{\ell m}(\theta,\phi) \tag{4.3}$$

from which one can calculate the multipole coefficients $a_{\ell m}$ as

$$a_{\ell m}\equiv\int Y^{*}_{\ell m}(\theta,\phi)\Delta(\theta,\phi)d\Omega \qquad \text{using} \quad d\Omega=sin\theta\ d\theta\ d\phi. \tag{4.4}$$

The angular power spectrum is defined as the variance of the function $\Delta(\theta,\phi)$ (Kurki-Suonio (2009)) obtained by

$$C_\ell\equiv<|a_{\ell m}|^2>=\frac{1}{2\ell+1}\sum_m|a_{\ell m}|^2. \tag{4.5}$$

This analysis is similar to what is done in the context of the Cosmic Microwave Background (CMB). Since we are using a discrete sample without a continuous sky coverage as it is the case of the CMB surveys, one should include the size and coverage of the sky into this analysis. For that reason, Nusser et al. (2012) account for discrete data through the parameters f_{sky} and $\bar{n}$, where $4\pi f_{sky}$ steradians is the assumed partial coverage of the sky of the dataset considered and $\bar{n}=N/(4\pi f_{sky})$ is the corresponding mean number density over the observed part of the sky with N as the number of sources. This leads to

$$C_\ell\equiv\frac{1}{(2\ell+1)f_{sky}}\sum_m|a_{\ell m}|^2 \qquad \text{with} \qquad a_{\ell m}=\frac{1}{f_{sky}^{1/2}}\int\Delta(\theta,\phi)Y_{\ell m}(\theta,\phi). \tag{4.6}$$

On the data side and using a similar approach to the CMB power spectrum (Dodelson (2003)), one should start by taking the two point correlation function of the measurements, i.e., to obtain the product and the angular distance, θ, between each unique pair of sources in the sky. The correlation function is then averaged for each angular distance as the follow expression shows

$$c(\theta)=<\frac{\Delta\alpha}{\alpha}(RA,Dec)\frac{\Delta\alpha}{\alpha}(RA',Dec'))>, \tag{4.7}$$

where $\frac{\Delta\alpha}{\alpha}(RA, Dec)$ is the measurement of the relative variation of the fine structure constant in a specific line of sight given by the celestial coodinates right ascension (RA) and declination (DEC) and the brackets $< . >$ correspond to the average taken over all possible pairs of separation θ.

Introducing the Nusser et al. (2012) modifications and rewriting this equation, one gets

$$c(\theta) = \frac{1}{\bar{n}^2 f_{sky}} < \frac{\Delta\alpha}{\alpha}(RA, Dec)\frac{\Delta\alpha}{\alpha}(RA', Dec')) > . \tag{4.8}$$

We take $f_{sky} = 1$ as we are dealing with wide spread point sources instead of patch of the sky inside a full sky survey.

The angular correlation function is the Legendre transform of the power spectrum. With the angular correlation function $c(\theta)$, one can determine the power spectrum C_l as

$$C_l = \int c(\theta) P_l(cos\theta) d\Omega. \tag{4.9}$$

where $P_l(cos\theta)$ is the Legendre polynom and Ω the solid angle. The power spectrum estimator $\hat{C}_l$ is computed as

$$\widehat{C}_l = 2\pi \sum_{\theta} c(\theta) P_l(cos\theta) sin\theta \Delta\theta \tag{4.10}$$

with $\Delta\theta$ being the difference between consecutive values of the angular distance θ.

The expected error of the power spectrum estimator can be obtained through the expression

$$\Sigma^2 = \frac{2}{(2l+1) f_{sky}} \Big(\frac{\sigma_f^2}{\bar{n}} + \hat{C}_l \Big)^2 \tag{4.11}$$

which includes both contributions of the shot noise Σ_{SN} and cosmic variance Σ_{CV} that can be ex-

pressed as

$$\Sigma_{SN} = \sqrt{\frac{2}{(2l+1)f_{sky}}}\frac{\sigma_f^2}{\bar{n}}, \qquad \Sigma_{CV} = \sqrt{\frac{2}{(2l+1)f_{sky}}}\hat{C}_l. \tag{4.12}$$

To minimize the effects of the shot noise, each measurement is weighted by a factor w_i^2 given by

$$w_i^2 = \frac{N\sigma_i^{-2}}{\sum_j \sigma_j^{-2}} \tag{4.13}$$

which yields the aforementioned quantity σ_f as

$$\sigma_f^2 = \frac{N}{\sum_j \sigma_j^{-2}} \tag{4.14}$$

where the σ_j is the error of the measurement (in the case of systematic and statistical errors we use the combined error obtained by adding them in quadrature).

We will consider different datasets: from the archival dataset (table B.3), we consider both Keck and VLT data separatly and as a single dataset (labeled Webb). We further consider the recent dedicated measurements (labeled as New) separatly and all datasets combined (labeled all).

The data analysis considering Keck, VLT and the New datasets can be found on figure 4.1 where it shows the estimated power spectrum $\hat{C}_l$ and its corresponding expected error Σ plotted simultaneously. Here one can see how the various datasets show a similiar behaviour though the measurements have been taken in different hemispheres, and the diverse quality of its systimatic estimations.

Figure 4.2 each dataset aforementioned. The New dataset is included in this analysis for its tighter uncertainties but the small number of measurements leads to a not robust statistical analysis illustrated by its peculiar features as seen in figure 4.2. The logarithm of expected error of this estimation and its explicit contributions can be found in figure 4.3.

Often there is more than one measurement of the deviation of the fine structure constant in the same line of sight as the light from the quasar goes through more than one absorption cloud until it reaches the Earth. For that reason and to avoid null angular separations, we chose to use the weighted mean measurement for measurements in the same line of sight. Before computing the correlation function,

the dataset is analysed and replaced by new values of weighted redshift, z_w, weighted relative variation of the fine structure constant, $\frac{\Delta\alpha}{\alpha}_w$ and its corresponding weighted error, σ_w described by

$$z_w = \frac{\sum_i w_i \times z_i}{\sum_i w_i}, \qquad \left.\frac{\Delta\alpha}{\alpha}\right|_w = \frac{\sum_i w_i \times \frac{\Delta\alpha}{\alpha}_i}{\sum_i w_i}, \qquad \sigma_w^2 = \frac{1}{\sum_i w_i} \tag{4.15}$$

where w is the weight given by

$$w_i = \frac{1}{\sigma_i^2}. \tag{4.16}$$

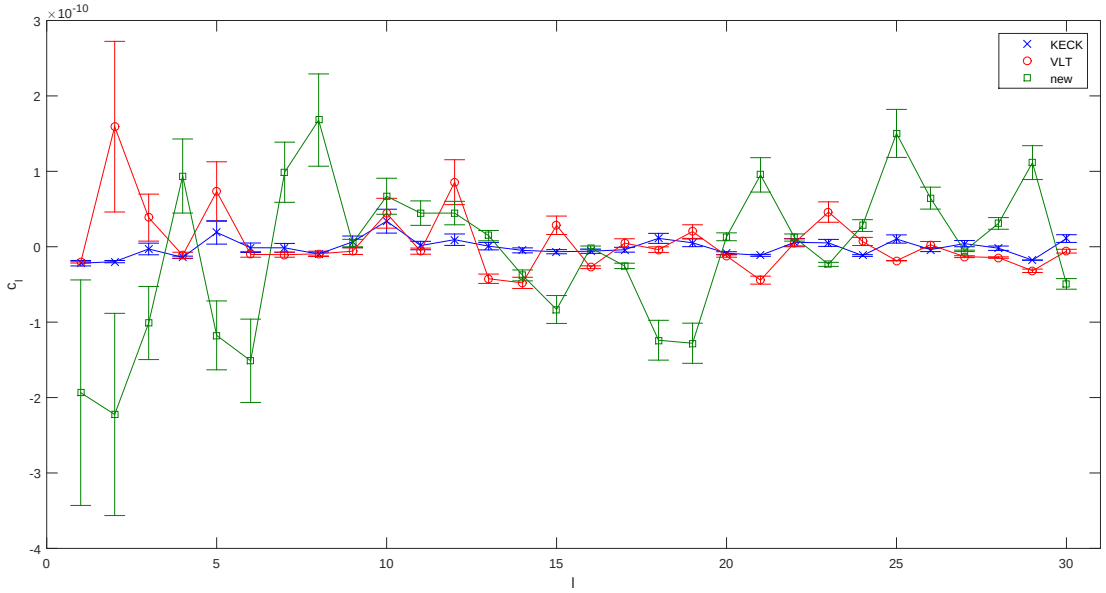

Figure 4.1: Angular power spectrum $\widehat{C_l}$ for the Keck dataset (blue), VLT dataset (red) and recent dedicated measurements (green) plotted together.

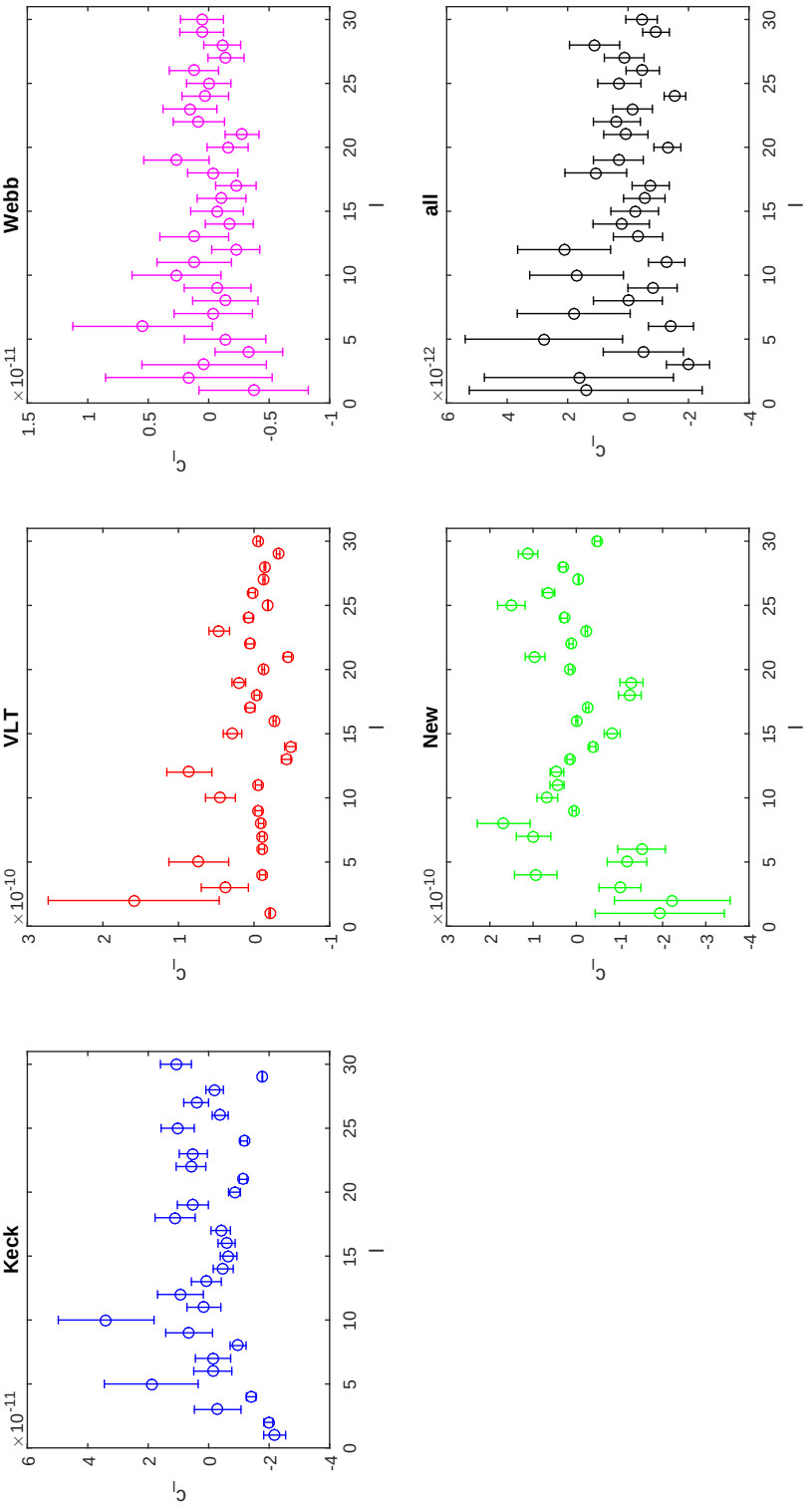

Figure 4.2: Angular power spectrum estimation $\widehat{C_l}$ as a function of the multipole ℓ with its expected error Σ for the datasets considered: Keck, VLT, Webb (Keck+VLT), recent dedicated measurements (New) and all datasets combined.

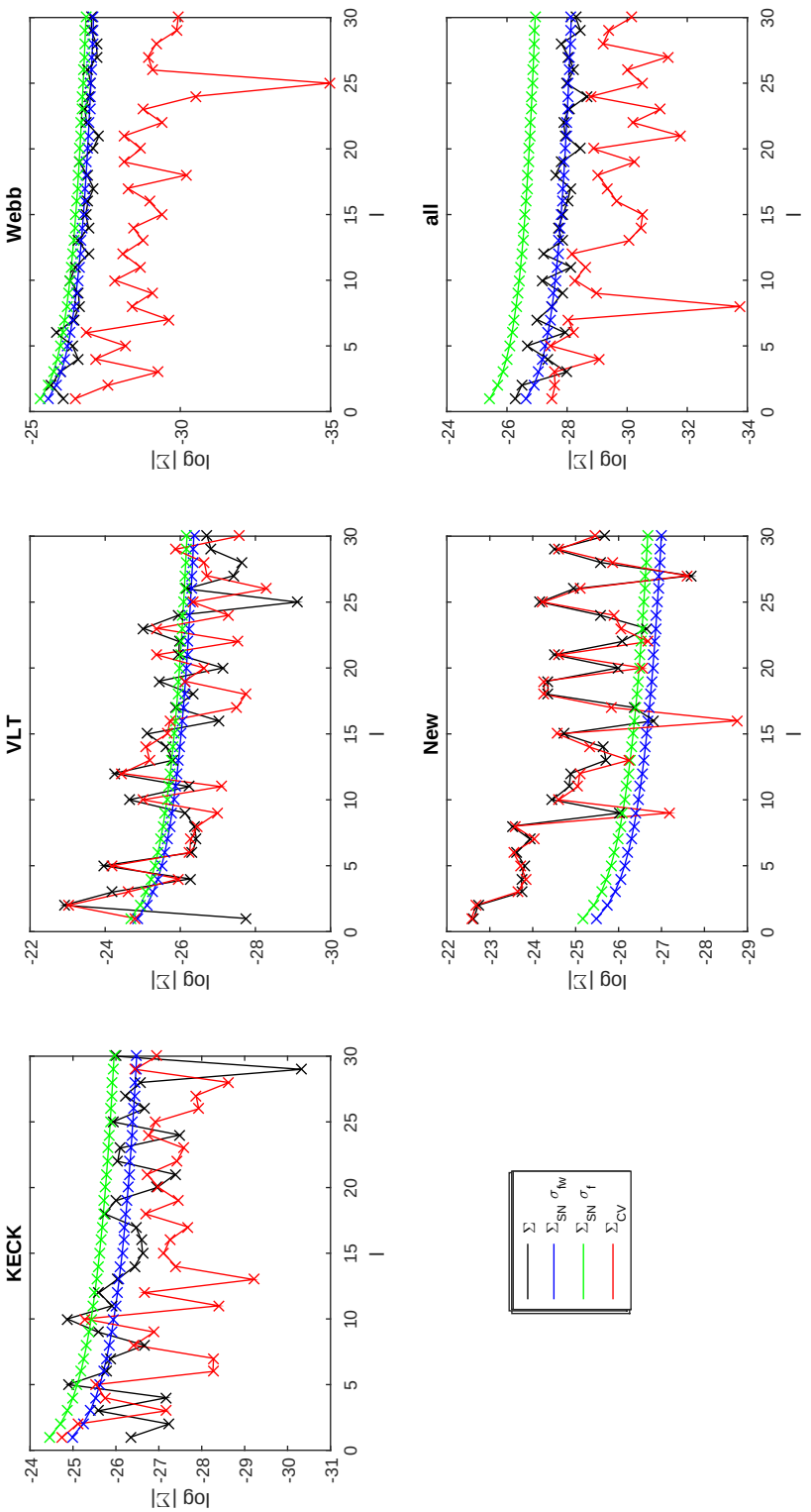

Figure 4.3: The logarithm of the expected error Σ of the estimator $\widehat{C_l}$ and the individual contributions of the shot noise Σ_{SN} and cosmic variance Σ_{CV} for each considered dataset.

4.2 THEORETICAL POWER SPECTRUM

Our goal is to compare the power spectrum that we obtain from the fine-structure constant measurements with some theoretical prediction by running Monte Carlo Markov chains simulations using of the software COSMOMC (Lewis et al. (2002)). For that purpose we chose the symmetron model which will be briefly introduced.

The symmetron model (Hinterbitchler et al. (2011)) is a modified gravity model where α variations arise from the spacetime variation of a scalar field which acts according to the field-strength tensor $F^2_{\mu\nu} \rightarrow f(\phi)F^2_{\mu\nu}$ (see section 1.3). In this particular model, the scalar field couples with gravitational strength in regions of low density and it is screened in regions of high density. This feature of dependence on the environment is one of the motivations for the choice of this model. After the indications of a spatial dipole by Webb et al. (2011), it is useful to pursue the possibility of spatial variations of α though the argument in the literature points to the dominance of the time variations (Olive et al. (2008)).

Symmetron model

The symmetron model is a scalar-tensor modification of gravity described by the action

$$S = \int dx^4\sqrt{-g}\Big[\frac{R}{2}M_{pl}^2 - \frac{1}{2}(\partial\phi)^2 - V(\phi)\Big] + S_m(\Psi_m; g_{\mu\nu}A^2(\phi)) \tag{4.17}$$

where g =det$g_{\mu,\nu}$, $M_{pl} = 1/\sqrt{8\pi G}$ and S_m is the matter-action (Silva et al. (2013)). The conformal coupling between the scalar field and the matter fields Ψ_m expressed by $\tilde{g}_{\mu,\nu} = g_{\mu,\nu}A^2(\phi)$ leads to the experience of a fifth force. In a non-relativistic limit this is given by

$$\overrightarrow{F}_\phi \equiv \frac{dA(\phi)}{d\phi}\overrightarrow{\nabla}\phi = \frac{\phi\overrightarrow{\nabla}\phi}{M^2}. \tag{4.18}$$

The potential is chosen to be of the symmetry breaking form

$$V(\phi) = -\frac{1}{2}\mu^2\phi^2 + \frac{1}{4}\lambda\phi^4 \tag{4.19}$$

and the conformal coupling as the simplest one consistent with the potential symmetry as $A(\phi) = 1 + \frac{1}{2}\left(\frac{\phi}{M}\right)^2$.

The dynamics of the scalar field ϕ is determined by the effective potential

$$V_{eff}(\phi) = V(\phi) + A(\phi)\rho_m = \frac{1}{2}\Big(\frac{\rho_m}{\mu^2 M^2} - 1\Big)\mu^2\phi^2 + \frac{1}{4}\lambda\phi^4 \tag{4.20}$$

this means that in the early Universe when the matter density is high, the effective potential has a minimum $\phi = 0$ where the field will reside. As the Universe expands, the matter density dilutes until it reaches a critical density $\rho_{SSB} = \mu^2 M^2$ for which the symmetry breaks and the field moves to one of the two new minima $\phi = \pm\phi_0 = \pm\mu/\sqrt{\lambda}$.

The fifth-force between two test particles residing in a region of space where $\phi = \phi_{local}$ can be found to be

$$\frac{F_\phi}{F_{gravity}} = 2\beta^2\Big(\frac{\phi_{local}}{\phi_0}\Big)^2, \qquad \beta = \frac{\phi_0 M_{pl}}{M^2} \tag{4.21}$$

for separations of the Compton wavelength $\lambda_{local} = 1/\sqrt{V_{eff,\phi\phi}(\phi_{local})}$, where the coupling strength to gravity is given by β. For larger separations or in the cosmological background before symmetry breaking $\phi_{local} \approx 0$, the force is supressed. After symmetry breaking, the field moves towards $\phi = \pm\phi_0$ and the force is comparable to gravity for $\beta = \mathcal{O}(1)$. Non-linear effects in the field-equation ensure that the force is effectively screened in high density regions supporting the local gravity constrains found.

The symmetry breaks at the scale factor a_{SSB}

$$a_{SSB} = \Big(\frac{\rho_{m,0}}{\rho_{SSB}}\Big), \qquad \lambda_{\phi,0} = \frac{1}{\sqrt{2}\mu}. \tag{4.22}$$

and the range of the fifth-force when the symmetry is broken $\lambda_{\phi 0}$ is given by

$$\lambda_{\phi 0} = \frac{1}{\sqrt{2}\mu} \tag{4.23}$$

where local gravity constraints satisfy $\lambda_{\phi 0} \lesssim$ Mpc$/h$ for symmetry breaking close to today, i.e. $a_{SSB} \approx 1$.

Considering generalizations where the electromagnetic field is coupled as

$$S_{EM} = -\int dx^4 \sqrt{g} A_\gamma^{-1}(\phi) \frac{1}{4} F^2_{\mu,\nu}, \tag{4.24}$$

this coupling leads to

$$\alpha = \alpha_0 A_\gamma(\phi) \tag{4.25}$$

as the electromagnetic field is unaffected by the conformal coupling and this coupling does not affect the Klein-Gordon equation for the scalar field.
Chosing the quadratic coupling $A_\gamma(\phi) = 1 + \frac{1}{2}\left(\frac{\beta_\gamma \phi}{M}\right)^2$ as Silva et al. (2013), one gets a variation of the fine structure constant as

$$\frac{\Delta\alpha}{\alpha} = A_\gamma(\phi) - 1 = \frac{1}{2}\left(\frac{\beta_\gamma \phi}{M}\right)^2. \tag{4.26}$$

Taking perturbations of the scalar field in the Fourier space, one can derive its power spectrum as

$$P_{\Delta\alpha}(k,a) = \left[\frac{3\Omega_m H_0^2 \beta_\gamma^2 \beta^2}{a(k^2 + a^2 m_\phi^2)} \left(\frac{\overline{\phi}}{\phi_0}\right)^2\right]^2 P_m(k,a). \tag{4.27}$$

where Ω_m is the matter density today, H_0 is the Hubble parameter today, β_γ is the scalar-photon coupling relative to the scalar-matter coupling, $\beta = \phi_0 M_{pl}/M^2$ is the coupling strength to gravity, a is the scale factor, k is the co-moving wavenumber, $m_\phi^2 = V_{eff,\phi\phi}(\bar{\phi})$ is the scalar mass in the cosmological background, $(\overline{\phi}/\phi_0)$ is the background scalar field value and $P_m(k,a)$ is the matter power spectrum. For $a \geq a_{SSB}$,

$$\left(\frac{\overline{\phi(a)}}{\phi_0}\right)^2 = \left(1 - \left(\frac{a_{SSB}}{a}\right)^3\right), \qquad m_\phi^2(a) = \frac{1}{\lambda_{\phi 0}^2} = \left(1 - \left(\frac{a_{SSB}}{a}\right)^3\right). \tag{4.28}$$

Equation 4.27 is plotted in figure 4.4. Using these expressions and the Hubble parameter as $H_0 =$

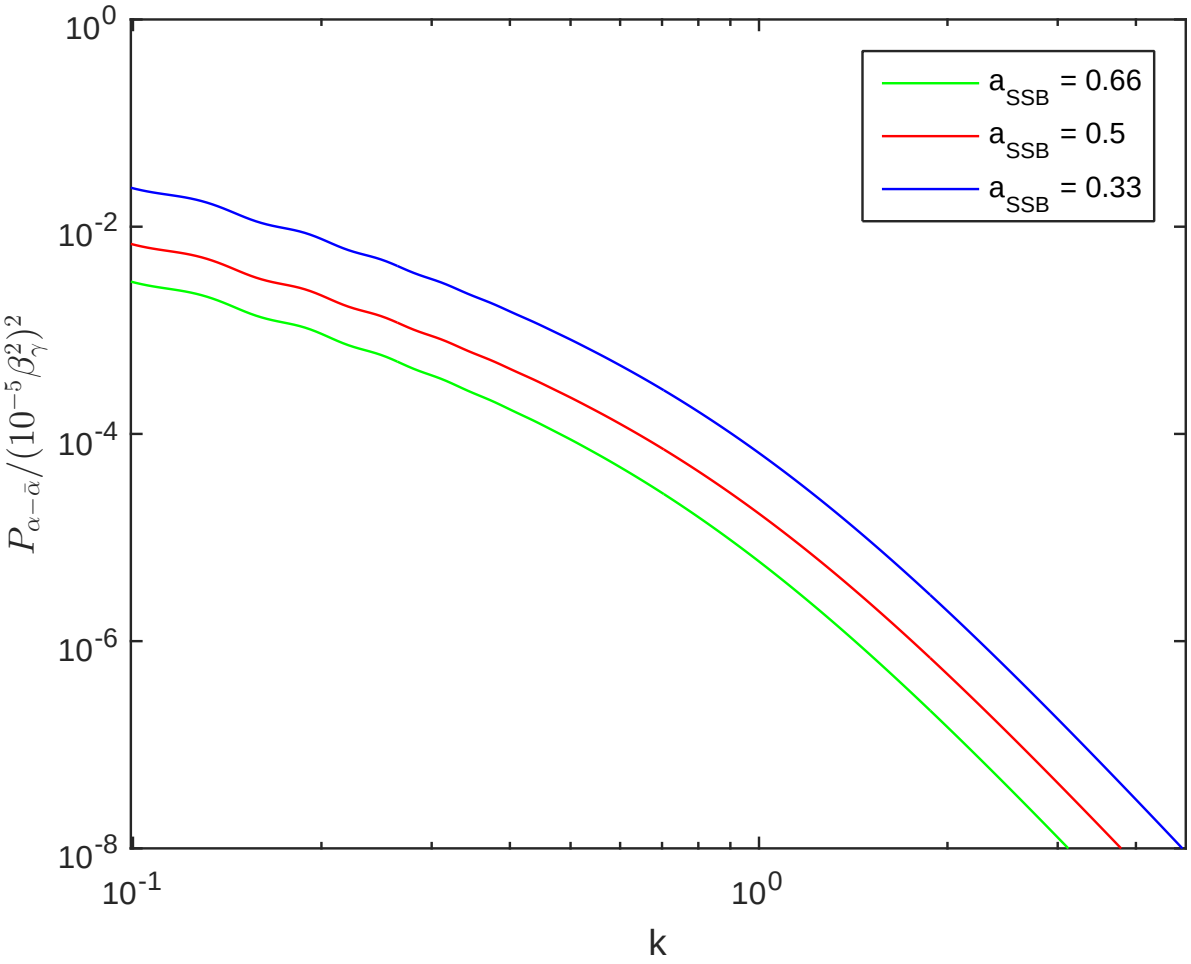

Figure 4.4: Theoretical power spectrum $P_{\alpha-\bar{\alpha}}(k,a)$ given by eq. 4.27 as a function of the wavenumber k for $a=1$ and different symmetry breaking scale factors $a_{SSB}=[0.33,0.5,0.66]$. In this plot a normalization factor was used $x=0.06(0.5/a_{SSB})$.

$\frac{h}{2.998\times10^3 Mpc}$, we can rewrite it as

$$P_{\Delta\alpha}(k,a)=\left[\frac{0.33\Omega_m 10^{-6}\beta_\gamma^2\beta^2}{a((k/m_\phi)^2+a^2)}\left(\frac{\lambda_{\phi 0}}{Mpc/h}\right)^2\right]^2 P_m(k,a). \tag{4.29}$$

In order to compare with the fine structure constant measurements, we want to express equation 4.27 in the form of an angular power spectrum. The angular power spectrum can be written as a kernel projection $W_i(z)$ (Jeong (2010)) of the 3D density field (White (2008)) which in this case is the linear power spectrum $P^{s_i,s_j}(k,z)$.

For our purpose, the approach described by Jeong (2010) is useful to start with. The use of the Limber approximation simplifies the calculations (LoVerde et al. (2008)) allowing to avoid the expensive computational cost of integrating the Bessel function. Assuming that the linear power spectrum is a slow-varying function, that is the behaviour of this function at infinity is similar to the behaviour of a

function converging at infinity, one gets

$$C_l^{x_i,x_j} \approx \int dz W_i(z) W_j(z) \frac{H(z)}{d_A^2(z)} P^{s_i,s_j}\left(k = \frac{l+1/2}{r}; z\right) \tag{4.30}$$

where $W_i(z)$ and $W_j(z)$ is the normalized galaxy distribution function in redshift space, H(z) is the Hubble parameter function, $d_A(z)$ is the angular diameter distance function and P^{s_i,s_j} is the linear power spectrum obtained before (equation 4.27) with $k = \frac{l+1/2}{r}$ as the Limber approximation and r is the comoving distance.

For the source distribution function, a 20 bins histogram was computed with MATLAB for each dataset considered. The example of the archival dataset source distribution can be found in figure 4.5. It is then normalized in COSMOMC with a simple overall integral.

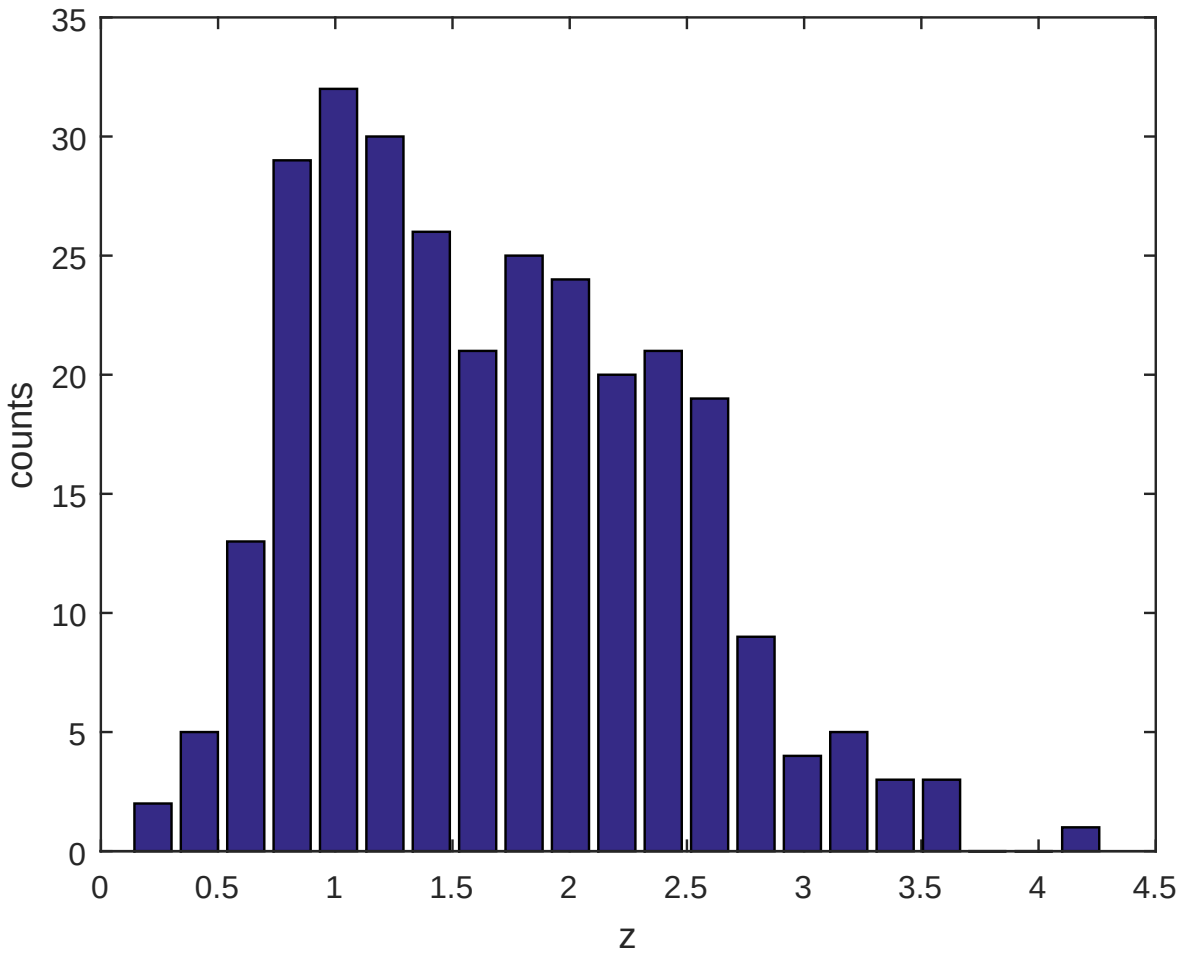

Figure 4.5: Source distribution function in redshift space for the archival dataset (Webb et al. (2011)).

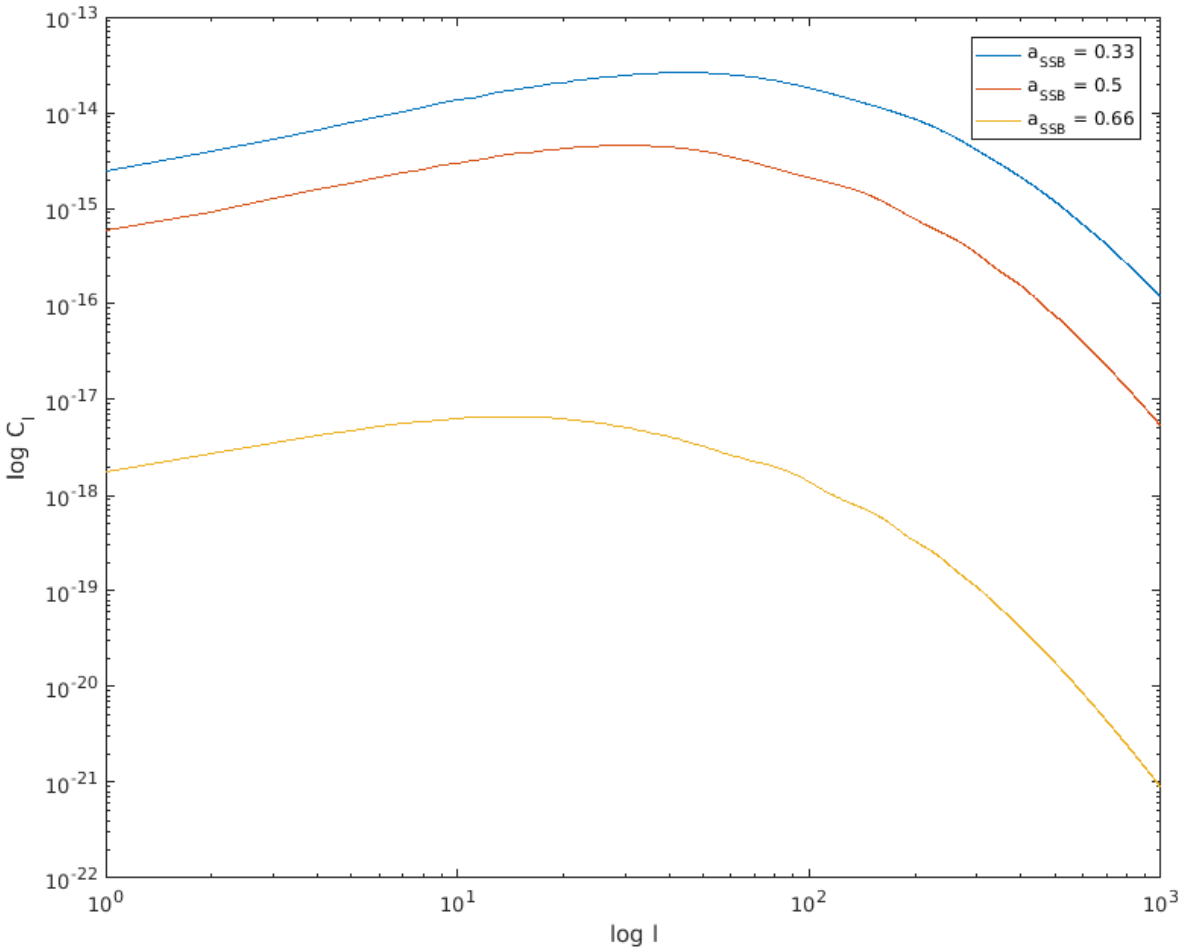

Figure 4.6: Theoretical power spectrum C_l for the symmetron model for different values of the scale factor for the symmetry breaking a_{SSB} in loglog scale.

4.3 DATA ANALYSIS

Our approach to analyse the α measurements on the previous chapters was to use the standard χ^2 techniques on a grid. We aim to drop the grid use and expand the parameter space without compromising the accuracy of the results or lengthening the computational time. For that reason, a Markov-Chain Monte Carlo (MCMC) method is the chosen tool for the following analysis.

The Monte Carlo method intends to overcome hard integrations that usual arise in Bayesian statistics analyses with non-linear models and multiple parameters. Generically (Gregory (2005)), the MCMC algorithms obtain a sample of the *target distribution* by using Markov chains that randomly walk through the model's parameter space. In the end, we get a sample with a probability of being in a region of this

parameter space proportional to the posterior density of that region. The Markov chain generates a new sample based on the previous one acording to a transition probability. After an initial burn-in period that is removed later, the chain is generating samples with a probability density distribution equal to the necessary posterior probability distribution.

The usual Monte Carlo integration procedure is to choose *n* points of the parameter space *X* uniformely and randomly distributed. These points are chosen in a multi-dimensional volume *V* that must be large enough to include the sectors where the weighted likelihood distribution contributes significantly.

The process of MCMC method using a Metropolis-Hastings algortihm starts with choosing a proposed value, Y, for the first iteration, X_{t+1}, from a given proposal distribution, $q(Y|X_t)$. The next step is to accept or reject Y for X_{t+1}based on the Metropolis ratio

$$r = \frac{p(Y|D,I)}{p(X_t|D,I)} \frac{q(X_t|Y)}{q(Y|X_t} \tag{4.31}$$

where $p(X|D,I)$ is the desired posterior density distribution. If the proposal distribution is symmetric, then $\frac{q(X_t|Y)}{q(Y|X_t} = 1$. If $r \geq 1$, then Y is accepted and $X_{t+1} = Y$. If $r < 1$, Y is accepted with probability equal to r. This step is done by sampling a random variable U from a uniform distribution from 0 to 1 which if $U \leq r$, then the proposed value Y is accepted, $X_{t+1} = Y$, otherwise it is set $X_{t+1} = X_t$. We can also reframe this step by calling the acceptance probability $\alpha(X_t, Y)$ given by

$$\alpha(X_t, Y) = min(1, r). \tag{4.32}$$

The original Metropolis algorithm considered only symmetric proposal distributions, which later Hastings generalized to asymmetric proposal distributions, giving rise to the known Metropolis-Hastings algorithm.

For our purposes, we use COSMOMC, which is a MCMC engine designed for cosmological purposes (Lewis et al. (2002)). Written in Fortran and Python, the code uses a simple Metropolis algorithm by default but has also an optimized fast-slow sampling method (Lewis (2013)) usually used with large surveys like Planck (Planck colaboration (2015)). To compute the ΛCDM matter power spectrum,

CAMB (Code for Anisotropies in the Microwave Background - Lewis et al. (2000), Howlett et al. (2012)) is used.

We implemented the symmetron model in COSMOMC considering as free parameters the scale factor when the symmetry breaks, a_{SSB}, the coupling strength to gravity, β and the range of the fifth force when the symmetry is broken, $\lambda_{\phi 0}$. For other cosmological values necessary to run these chains, we use the latest results from Planck colaboration (2015).
On a first stage, we will allow to vary a_{SSB} and β (which we reframe and sample $log\beta^2$ for numerical purposes). The parameter $\lambda_{\phi 0}$ is fixed to 1. Table 4.1 describes the 1 sigma bounds obtained and figure 4.9 and 4.10 show the posterior density distribution for both and each free parameter using different datasets, the archival α measurements from Webb et al. (2011) and all data combined which includes the recent dedicated measurements.

	a_{SSB}	$log\beta^2$	β
Webb data	> 0.392	< 1.82	< 8.13
All data	> 0.410	< 1.74	< 7.41

Table 4.1: Constrains on the symmetron parameters a_{SSB} and $log\beta^2$ with $\lambda_{\phi 0} = 1$ given by the archival dataset of α measurements of Webb et al. (2011) and all datasets combined (archival and recent dedicated measurements, table B.2).

As the recent dedicated measurements are consistent with a non-varying fine-structure constant, the constraints found are less strong than the ones found using the archival dataset. Later, we do this analysis with only one free paramter. Fixing $log\beta^2 = 1$ and $\lambda_{\phi 0} = 1$, we find a upper bound by the archival dataset,

$$a_{SSB} < 0.610 \tag{4.33}$$

and for all data combined, this parameter is unconstrained, as displayed in figure 4.7.
Considering $log\beta^2$ as the only free parameter, we run chains fixing $\lambda_{\phi 0} = 1$ and different values of $a_{SSB} = 0.33, 0.5$ and 0.66. The values on table 4.2 demonstrate that, if the symmetry breaks more recently, a larger coupling value is allowed by the archival data. The bounds considering all data are

slightly better than the ones from the archival measurements.

	$a_{SSB} = 0.33$	$a_{SSB} = 0.50$	$a_{SSB} = 0.66$
Webb	< 2.86	< 3.53	< 4.51
All data	< 2.83	< 3.39	< 4.39

Table 4.2: 2 σ constraints on the symmetron parameter $log\beta^2$ given by the Webb et al. (2011) dataset and all datasets combined (archival and recent dedicated measurements, table B.2) for different values of a_{SSB} and fixing $\lambda_{\phi 0} = 1$.

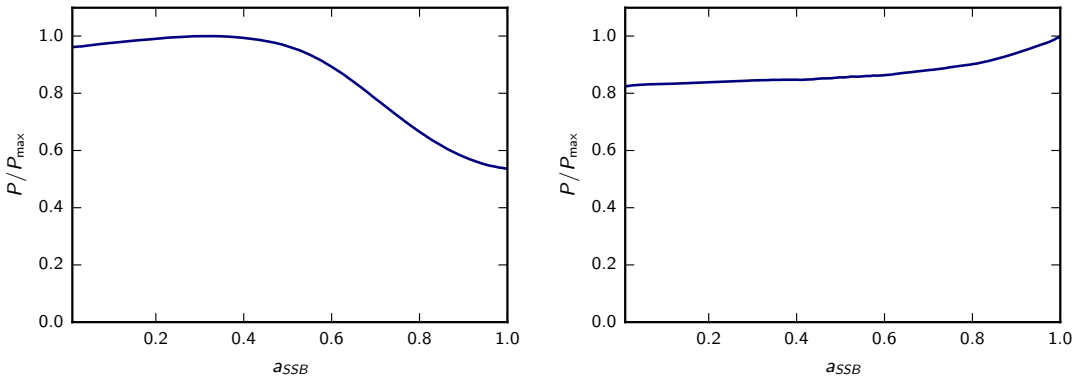

Figure 4.7: Normalized posterior probability distribution contours from COSMOMC sampling only the a_{SSB} parameter. In the right panel, we use the archival dataset and in the left panel all data combined, with $log(\beta^2) = 1$ and $\lambda_{\phi 0} = 1$ fixed.

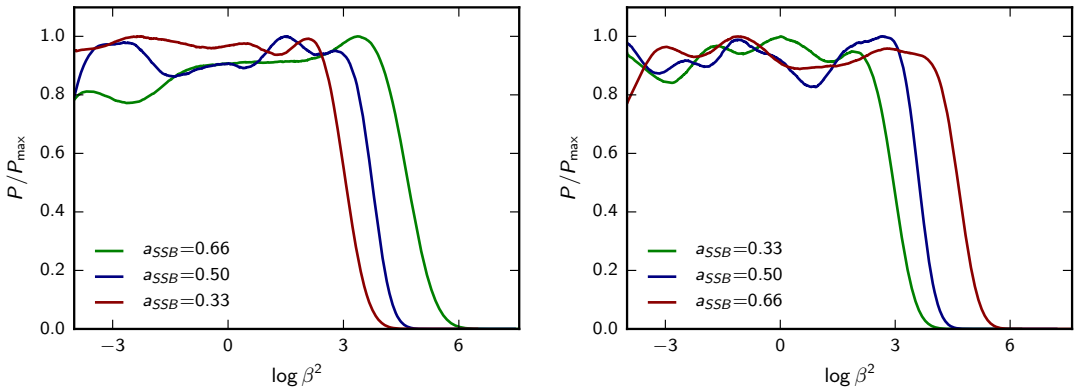

Figure 4.8: Normalized posterior probability distribution contours from COSMOMC sampling only the $log\beta^2$ parameter with different values of a_{SSB}. On the right panel, we use the archival dataset and on the left panel all data combined, with $\lambda_{\phi 0} = 1$ fixed.

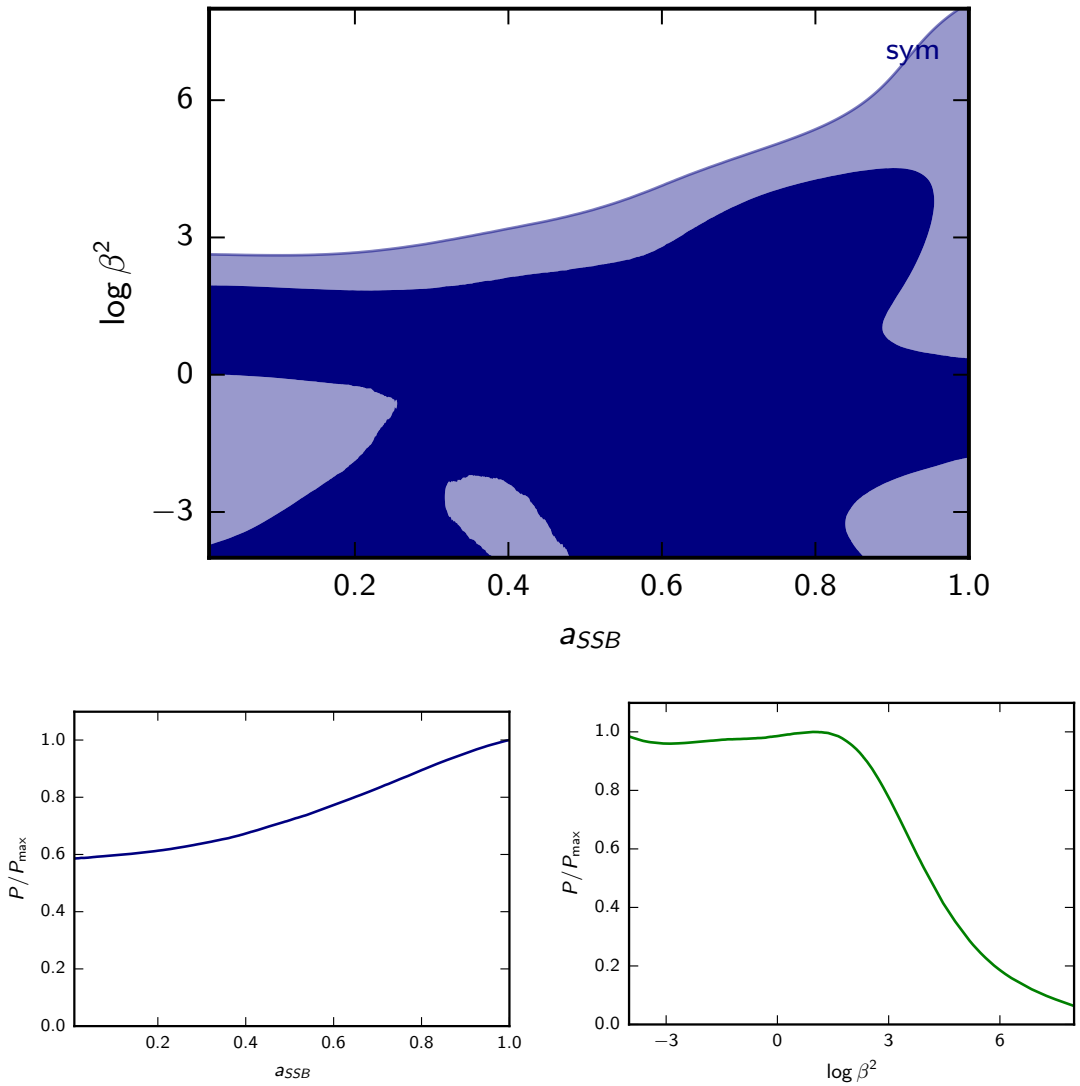

Figure 4.9: Posterior probability distribution contours from COSMOMC sampling a_{SSB} and $log(\beta^2)$ using the archival dataset of α measurements (Webb et al. (2011)). On the top panel is the two-dimensional contours and on the bottom the one-dimensional normalized contours for the scale factor where the symmetry breaks a_{SSB} on the left and for logorithm of the strength of the coupling to gravity $log(\beta^2)$.

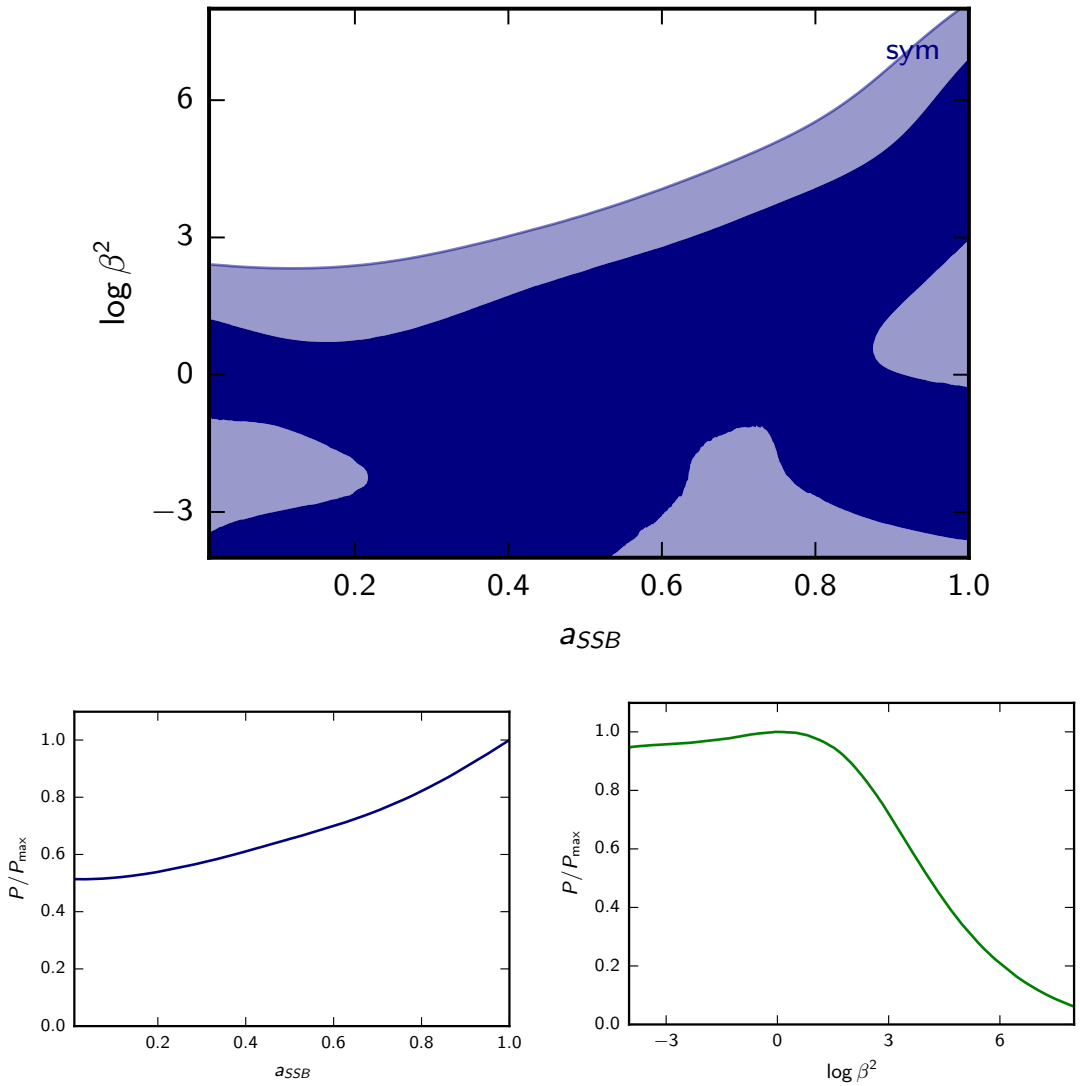

Figure 4.10: Posterior probability distribution contours from COSMOMC sampling a_{SSB} and $log\beta^2$ using all the datasets of α measurements combined. On the top panel is the two-dimensional contours and on the bottom the one-dimensional normalized contours for the scale factor where the symmetry breaks a_{SSB} on the left and for logorithm of the strength of the coupling to gravity $log(\beta^2)$.

Chapter 5.

Conclusions

The Equivalence Principle tests span over a wide range of parameters and models that measure or predict its violation. Hence we have explored several approaches to this subject and some conclusions will be drawn regarding each one.

Considering the case of time variations of α, we note that the constraints found are dominated by atomic clocks tests, which are only sensitive to the dark energy equation of state today. Thus a constant equation of state cosmological model is a reasonable assumption. We also pointed out how different currently available datasets lead to somewhat different constraints. This later statement as well as the dominance of the atomic clocks measurement are common results to every equation of state that was studied.

Upgrading the simplest scenario with the a redshift-dependent term, the constraints found remain consistent with standard paradigm. The addition of a free parameter shows that the constraints are somewhat model-dependent but they are competitive and tight though yet compatible with the current cosmological model where $w_0 = -1$ and $\zeta = 0$. This explains why additional parameters such as w_a in the CPL parametrization are weakly constrained by the present data.

In the classes of models we have studied, the dynamical degree of freedom responsible for the dark energy and the α variation inevitable couples to nucleons (through the α dependence of their masses) and leads to violations of the Weak Equivalence Principle. Our bounds on the coupling ζ can therefore be used to obtain indirect bounds on the Eötvös parameter η. Despite the aforementioned model de-

pendence, these bounds are stronger than the current direct ones, typically by as much as one order of magnitude, around $\eta \approx \mathcal{O}(10^{-14})$.

Improvements in astrophysical measurements both in terms of statistical uncertainties and control over possible systematics will allow significantly stronger constraints on a larger parameter space. The ongoing UVES Large Program should further improve the status quo but also the new generation of high resolution ultrastable spectrographs such as ESPRESSO and ELT-HIRES would be ideal for this task. Specifically for Class I models, we may conservativly expect a sensitivity of $\eta \approx \mathcal{O}(10^{-16})$ for ESPRESSO (Leite et al. (2014)) and $\eta \approx 10^{-18}$ for ELT-HIRES (Leite and Martins (2015)).

Launched April 25, 2016, the MICROSCOPE mission should reach $\eta \approx 10^{-15}$ sensitivity. If a larger value than our bounds arises, that would mean one can rule out this Class I models that we analysed, in particular, that would rule out the assumption of a coupling between dynamic dark energy and the electromagnetic sector. Otherwise, a detection of a large η by MICROSCOPE would underly that α measurements have unaccounted systematics.

We have revisited the dipole analysis from Webb et al. (2011) and added recent tighter measurements. We confirm that a small number of tight measurements have a significant impact (Pinho and Martins (2016)). Our analysis also shows weaker evidence for a dipole, in addition to the fact that the current data cannot identify different classes of models. The combined dataset also decreases the uncertainties on each parameter. There are still possible hidden systematics but further measurements from the UVES Large Program will clarify this question. Also, the new generation of high-resolution ultra-stable spectropraphs such as ESPRESSO will allow measurements with smaller uncertainties and a better control over systematics.

Regarding the consistency tests of all available data, there is a tight constraint if considered a simple constant relation between varying fundamental constants. Although it is a first approximation, it induces further analysis by taking phenomenological parametrizations such as the work of Ferreira et al. (2015).

Ultimately, regarding the spatial variation chapter, there is a degeneracy direction between a_{SSB}, the scalar factor when the symmetry breaks and $log\beta^2$, the logarithm of the squared coupling strength rel-

ative to gravity. This means that if the symmetry breaks earlier, the prefered value for β is lower. Also, as α measurements are consistent with a no variation, the constraints found serve an upper bound for symmetron's parameters.

We aim to introduce the α measurements survey by Albareti et al. (2015) on the studies of spatial variation. This is a large dataset of low redshift measurements with uncertainties roughly not as tight as the recent measurements used in our present analysis. However, it will assess the impact of sky coverage and put to test the assumptions and approximations made. Furthermore we would like to extend our COSMOMC tool for other models where α is expected to vary and to investigate the degeneracies of the models with standard cosmological parameters.

The next decade will produce tests of these essential principles with unprecedented accuracy. If null results arise, for instance, from the E-ELT, it would imply that any supposed coupling of light scalar fields to the standard model would need to be unnaturally small. In turn, it would indicate that either WEP violating fields do not exist at all in nature or that these couplings are supressed by some yet unknown mechanism. Anyhow, our analysis shows that astrophysical tests of stability of fundamental couplings are a crucial probe of fundamental physics and cosmology.

Bibliography

Aad, G., Abajyan, T., Abbott, B., Abdallah, J., Abdel Khalek, S., Abdelalim, A. A., Abdinov, O., Aben, R., Abi, B., Abolins, M. and et al. (ATLAS Collaboration), 2012, Phys. Lett. B **716**, 1, http://dx.doi.org/10.1016/j.physletb.2012.08.020

Agafonova, I. I., Molaro, P., Levshakov, S. A. and Hou, J. L., 2011, A&A**529**, A28, http://dx.doi.org/10.1051/0004-6361/201016194

Albareti, F. D., Comparat, J., Gutiérrez, C. M., Prada, F., Pâris, I., Schlegel, D., López-Corredoira, M., Schneider, D. P., Manchado, A., García-Hernández, D. A., Petitjean, P. and Ge, J., 2015, Mon. Not. Roy. Astron. Soc. **4520**, 4153, http://dx.doi.org/10.1093/mnras/stv1406

Albornoz Vásquez, D., Rahmani, H., Noterdaeme, P., Petitjean, P., Srianand, R. and Ledoux, C., 2014, A&A**562**, A88, http://dx.doi.org/10.1051/0004-6361/201322544

Amendola, L. and Tsujikawa, S., *Dark Energy - Theory and Observations*, 2010, Cambridge University Press, http://dx.doi.org/10.1063/1.3603920

Bagdonaite, J., Murphy, M. T., Kaper, L. and Ubachs, W., 2012, Mon. Not. Roy. Astron. Soc. **421**, 419, http://dx.doi.org/10.1111/j.1365-2966.2011.20319.x

Bagdonaite, J., Daprà, M., Jansen, P., Bethlem, H. L., Ubachs, W., Muller, S., Henkel, C., and Menten, K. M., 2011, Phys.Rev.Lett. **111**, 231101, http://dx.doi.org/10.1103/PhysRevLett.111.231101

Bagdonaite, J., Ubachs, W., Murphy, M. T. and Whitmore, J., 2015, Phys.Rev.Lett. **114**, 071301, http://dx.doi.org/10.1103/PhysRevLett.114.071301

Bonometto, S., Primack, J. and Provenzale, A., *Dark Matter in the Universe*, 1997, Proc. Int. Sch. Phys. Fermi, **132** ISBNprint978-90-5199-294-6

Calabrese, E., Martinelli, M., Pandolfi, S., Cardone, V. F., Martins, C. J. A. P, Spiro, S. and Vielzeuf, P. E., 2014, Phys. Rev. D **89**, 083509 http://dx.doi.org/10.1103/PhysRevD.89.083509

Campbell, B. A. and Olive, K. A., 1995, Phys. Lett. B **345**, 429-434, http://dx.doi.org/10.1016/0370-2693(94)01652-S

Cardwell, R. R. and Linder, E. V., 2005, Phys. Rev. Lett. **95**, 141301, http://dx.doi.org/10.1103/PhysRevLett.95.141301

Carroll, S. M., 1998, Phys. Rev. Lett. **81**, 3067 http://dx.doi.org/10.1103/PhysRevLett.81.3067

Chand, H., Srianand, R., Petitjean, P., Aracil, B., Quast, R. and Reimers, D., 2006, A&A**451**, 45, http://dx.doi.org/10.1051/0004-6361:20054584

Chatrchyan, S., Khachatryan, V., Sirunyan, A. M., Tumasyan, A., Adam, W., Aguilo, E., Bergauer, T., Dragicevic, M., Erö, J., Fabjan, C. and et al. (CMS Collaboration), 2012, Phys. Lett. B **716**, 30 http://dx.doi.org/10.1016/j.physletb.2012.08.021

Chevallier, M. and Polarski, D., 2001, Int. J. Mod. Phys. D **10**, 213, http://dx.doi.org/10.1142/S0218271801000822

Chiba, T. and Kohri, K., 2002, Prog.Theor.Phys. **107**, 631, http://dx.doi.org/10.1143/PTP.107.631

Coc, A., Nunes, N. J., Olive, K. A., Uzan, J. and Vangioni, E., 2007, Phys. Rev. D **76**, 023511, http://dx.doi.org/10.1103/PhysRevD.76.023511

Curran, S., Tanna, A., Koch, F., Berengut, J., Webb, J. K., Stark, A. A. and Flambaum, V. V., 2011, A&A**533**, A55, http://dx.doi.org/10.1051/0004-6361/201117457

Damour, T. and Donoghue, J. F., 2010, Class.Quant.Grav. **27**, 202001, http://dx.doi.org/10.1088/0264-9381/27/20/202001

Dàpra, M., Bagdonaite, J., Murphy, M. T. and Ubachs, W., 2015, Mon. Not. Roy. Ast., **454**, 1, 489-506, http://dx.doi.org/10.1093/mnras/stv1998

Darling, J., 2004, Astrophys. J. **612**, 58, http://dx.doi.org/10.1086/422450

Darling, J., 2012, Ap. J., **761**, 2, 26, http://dx.doi.org/10.1088/2041-8205/761/2/L26

Davis, E. D., Gould, C. R. and Sharapov, E. I., 2014, Int. J. Mod. Phys. E **23**, 1430007, http://dx.doi.org/10.1142/S0218301314300070

Dodelson, S., *Modern Cosmology*, 2003, Academic Press, ISBN-10:0122191412

Doran,M. and Robbers, G., 2006, J. Cosmol. Astropart. Phys. **06**, 026 http://dx.doi.org/10.1088/1475-7516/2006/06/026

Dvali, G. and Zaldarriaga, M., 2002, Phys.Rev.Lett. **88**, 091303, http://dx.doi.org/10.1103/PhysRevLett.88.091303

Evans, T. M., Murphy, M. T., Whitmore, J. B., Misawa, T., Centurion, M., D'Odorico, S., Lopez, S, Martins, C. J. A. P., Molaro, P., Petitjean, P., Rahmani, H., Srianand, R., and Wendt, M., 2014, Mon. Not. Roy. Astron. Soc. **445**, 128, http://dx.doi.org/10.1093/mnras/stu1754

Farooq, O. and Ratra, B., 2013, Astrophys. J. L., **766**, 1, http://dx.doi.org/10.1088/2041-8205/766/1/L7

Ferreira, M. C., Julião, M. D., Martins, C. J. A. P and Monteiro, A. M. R. V. L., 2012, Phys. Rev. D **86**, 125025, http://dx.doi.org/10.1103/PhysRevD.86.125025

Ferreira, M. C., Frigola, O., Martins, C. J. A. P., Monteiro, A. M. R. V. L., and Solà, J., 2014, Phys. Rev. D **89**, http://dx.doi.org/10.1103/PhysRevD.89.083011

Ferreira, M. C. and Martins, C. J. A. P., 2015, Phys. Rev. D **91**, 124032, http://dx.doi.org/10.1103/PhysRevD.91.124032

Flambaum, V. V., 2003, e-print physics/0302015

Flambaum, V. V., Leinweber, D. B. Thomas, A. W. and Young, R. D. 2004, Phys. Rev. D **69**, 115006, http://dx.doi.org/10.1103/PhysRevD.69.115006

Flambaum, V. V. and Tedesco, A. V., 2006, Phys. Rev. C **73**, 055501, http://dx.doi.org/10.1103/PhysRevC.73.055501

Gregory, P. C., *Bayesian Logical Data Analysis for the Physical Sciences*, 2005, Cambridge University Press, http://adsabs.harvard.edu/abs/2005blda.book.....G

Heaston, R. J., 2008, 15th Natural Philosophy Alliance Conference, http://worldnpa.org/wp-content/uploads/2014/08/Why-Did-Einstein-Put-So-Much-Emphasis-on-the-Equivalence-Principle.pdf

Henkel, C., Menten, K. M., Murphy, M. T., Jethava, N., Flambaum, V. V., Braatz, J. A., Muller, S., Ott, J. and Mao, R. Q., 2009, A&A**500**, 725, http://dx.doi.org/10.1051/0004-6361/200811475

Hinterbichler, K., Khoury, J., Levy, A. and Matas, A., 2011, Phys. Rev. D **84**, 103521, http://dx.doi.org/10.1103/PhysRevD.84.103521

Howlett, C., Lewis, A., Hall, A. and Challinor, A., 2012, JCAP, **1204**, 027, http://dx.doi.org/10.1088/1475-7516/2012/04/027

Ilyushin, V. V., Jansen, P., Kozlov, M. G., Levshakov, S. A., Kleiner, I., Ubachs, W. and Bethlem, H. L., 2012, Phys. Rev. **A 85**, 032505, http://dx.doi.org/10.1103/PhysRevA.85.032505

Kanekar, N., Chengalur, J. N. and Ghosh, T., 2010, Astrophys. J. Lett. **716**, L23, http://dx.doi.org/10.1088/2041-8205/716/1/L23

Kanekar, N., 2011, Astrophys. J. L. **728**, L12, http://dx.doi.org/10.1088/2041-8205/728/1/L12

Kanekar, N., Langston, G. I., Stocke, J. T., Carilli, C. L. and Menten, K. M., 2012, Ap.J.Lett. **746**, L16, http://dx.doi.org/10.1088/2041-8205/746/2/L16

King, J. A., Webb, J. K., Murphy, M. T. and Carswell, R. F., 2008, Phys. Rev. Lett. **101**, 251304, http://dx.doi.org/10.1103/PhysRevLett.101.251304

King, J. A., Murphy, M. T., Ubachs, W. and Webb, J. K., 2011, Mon. Not. Roy. Astron. Soc. **417**, 3010, http://dx.doi.org/10.1111/j.1365-2966.2011.19460.x

King, J. A., Webb, J. K., Murphy, M. T., Flambaum, V. V., Carswell, R. F., Bainbrige, M. B., Wilczynska, M. R., Koch, F. E., 2012, Mon. Not. Roy. Ast. Soc., **422**, 4, 3370-3414, http://dx.doi.org/10.1111/j.1365-2966.2012.20852.x

Kurki-Suonio, H. 2009, Lecture notes "Cosmology I & II", Chapter 12 http://theory.physics.helsinki.fi/~cpt/Cosmo12.pdf

Jeong, D. 2010, PhD thesis "*Cosmology with high (z > 1) redshift galaxy surveys*", University of Texas at Austin

Leite, A. C. O., Martins, C. J. A. P., Pedrosa, P. O. J. and Nunes, N. J., 2014, Phys. Rev. D **90**, 063519, http://dx.doi.org/10.1103/PhysRevD.90.063519

Leite, A. C. O. and Martins, C. J. A. P., 2015, Phys. Rev D **91**, 103519, http://dx.doi.org/10.1103/PhysRevD.91.103519

Lentati, L., Carilli, C., Alexander, P., Maiolino, R., Wang, R., Cox, P., Downes, D., McMahon, R., Menten, K. M., Neri, R., Riechers, D., Wagg, J., Walter, F. and Wolfe, A., 2012, Mon. Not. Roy. Astron. Soc. **430**, 2454, http://dx.doi.org/10.1093/mnras/stt070

Lewis, A., Challinor, A. and Lasenby, A., 2000, Astrophys. J., **538**, 473-476, http://dx.doi.org/10.1086/309179

Lewis, A. and Bridle, S., 2002, Phys. Rev. D, **66**, 103511, http://dx.doi.org/10.1103/PhysRevD.66.103511

Lewis, A., 2013, Phys. Rev. D, **87**, 103529, http://dx.doi.org/10.1103/PhysRevD.87.103529

Levshakov, S. A., Combes, F., Boone, F., Agafonova, I. I., Reimers, D. and Kozlov, M. G., 2012, A&A**540**, L9, http://dx.doi.org/10.1051/0004-6361/201219042

Liddle, A., *An Introduction to Modern Cosmology*, 2003, Wiley, ISBN:978-1-118-50214-3

Linder, E. V., 2003, Phys. Rev. Lett. **90**, 091301, http://dx.doi.org/10.1103/PhysRevLett.90.091301

LoVerde, M. and Afshordi, N., 2008, Phys. Rev. D, **78**, 123506, http://dx.doi.org/10.1103/PhysRevD.78.123506

Luo, F., Olive, K. A. and Uzan, J., 2011, Phys. Rev. D **84**, 096004, http://dx.doi.org/10.1103/PhysRevD.84.096004

Malec, A. L., Buning, R., Murphy, M. T., Milutinovic, N., Ellison, S. L., Prochaska, J. X., Kaper, L., Tumlinson, J., Carswell, R. F. and Ubachs, W., 2010, Mon. Not. Roy. Astron. Soc. **403**, 1541, http://dx.doi.org/10.1111/j.1365-2966.2009.16227.x

D.J.E. Marsh, P. Bull, P.G. Ferreira and A. Pontzen, 2014, Phys. Rev. D **90**, 105023, http://dx.doi.org/10.1103/PhysRevD.90.105023

Martins, C. J. A. P., 2002, Phil.Trans.Roy.Soc.Lond. **A360**, 2861, http://dx.doi.org/10.1098/rsta.2002.1087

Martins, C. J. A. P., 2014, Gen. Rel. and Grav. **47**, 1843, http://dx.doi.org/10.1007/s10714-014-1843-7

Martins, C. J. A. P and Pinho, A. M. M., 2015, Phys. Rev. D **91**, 103501, http://dx.doi.org/10.1103/PhysRevD.91.103501

Martins, C. J. A. P, Pinho, A. M. M., Alves, R. F. C., Pino, M., Rocha, C. I. S. A. and von Wietersheim, M., 2015, J. C. A. P. **08**, 08, 047 http://dx.doi.org/10.1088/1475-7516/2015/08/047

Martins, C. J. A. P, Pinho, A. M. M., Carreira, P., Gusart, A., López, J., Rocha, C. I. S. A., 2015, Phys. Rev. D **93**, 023506, http://dx.doi.org/10.1103/PhysRevD.93.023506

Mo, H., van der Bosch, F. and White, S., 2010, Cambridge University Press, http://dx.doi.org/10.1017/CBO9780511807244.001

Molaro, P., Reimers, D., Agafonova, I. I. and Levshakov, S. A., 2008, Eur. Phys. J. ST **163**, 173, http://dx.doi.org/10.1140/epjst/e2008-00818-4

Molaro, P., Centurion, M., Whitmore, J. B., Evans, T. M., Murphy, M. T., Agafonova, I. I., Bonifacio, P., D'Odorico, S., Levshakov, S. A., Lopez, S., Martins, C. J. A. P., Petitjean, P., Rahmani, H., Reimers, D., Srianand, R., Vladilo, G. and Wendt, M. 2014, A&A**555**, A68, http://dx.doi.org/10.1051/0004-6361/201321351

Muller, S., Beelen, A., Guélin, M., Aalto, S., Black, J. H., Combes, F., Curran, S. J., Theule, P. and Longmore, S. N., 2011, A&A**535**, A103, http://dx.doi.org/10.1051/0004-6361/201117096

Müller, J., Hofmann, F. and Biskupek, L., 2012, Class. Quant. Grav. **29**, 184006, http://dx.doi.org/10.1088/0264-9381/29/18/184006

Murphy, M. T., Webb, J., Flambaum, V., Drinkwater, M., Combes, F. and Wiklind, T., 2001, Mon. Not. Roy. Astron. Soc. **327**, 1244, http://dx.doi.org/10.1046/j.1365-8711.2001.04843.x

Murphy, M. T., Webb, J. K. and Flambaum, 2003, Mon. Not. Roy. Astron. Soc. **345**, 609-638, http://dx.doi.org/10.1046/j.1365-8711.2003.06970.x

Murphy, M. T., Flambaum, V. V., Webb, J. K., Dzuba, V. A., Prochaska, J. X. and Wolfe, A. M., 2004, L.N.P., **648**, p.131-150, http://adsabs.harvard.edu/abs/2004LNP...648..131M

Murphy, M. T., Flambaum, V. V., Muller, S. and Henkel, C., 2008, Science **320**, 1611, http://dx.doi.org/10.1126/science.1156352

Murphy, M. T., Webb, J. K. and Flambaum, V. V., 2009, Mem. Soc. Astron. Italiana**80**, p.833, http://adsabs.harvard.edu/abs/2009MmSAI..80..833M

Murphy, M. T., Malec, A. L., Prochaska, J. X, 2016, Mon. Not. Roy. Astron. Soc. **461**, 3, http://dx.doi.org/10.1093/mnras/stw1482

Nusser, A., Branchini, E. and Felix, M., 2012, JCAP, Issue **01**, 018 http://dx.doi.org/10.1088/1475-7516/2013/01/018

Nunes, N. J. and Lidsey, J. E., 2004, Phys. Rev. D **69**, 123511 http://dx.doi.org/10.1103/PhysRevD.69.123511

Olive, K. and Pospelov, M., 2008, Phys. Rev. D, **77**, 043524 http://dx.doi.org/10.1103/PhysRevD.77.043524

Perlmutter, S., Aldering, G., Goldhaber, G., Knop, R. A., Nugent, P., Castro, P. G., Deustua, S., Fabbro, S., Goobar, A., Groom, D. E., Hook, I. M., Kim, A. G., Kim, M. Y., Lee, J. C., Nunes, N. J., Pain, R., Pennypacker, C. R., Quimby, R., Lidman, C., Ellis, R. S., Irwin, M., McMahon, R. G., Ruiz-Lapuente, P., Walton, N., Schaefer, B., Boyle, B. J., Filippenko, A. V., Matheson, T., Fruchter, A. S., Panagia, N., Newberg, H. J. M., Couch, W. J., Project, T. S. C., 1999, Astron. J. **517**, 565, http://dx.doi.org/10.1086/307221

Petrov, Yu. V., Nazarov, A. I., Onegin, M. S., Petrov, V. Yu. and Sakhnovsky, E. G., 2006 Phys. Rev. C **74**, 064610 http://dx.doi.org/10.1103/PhysRevC.74.064610

Pinho, A. M. M. and Martins, C. J. A. P, 2016, Phys. Lett. B, **756**, 121-125, http://dx.doi.org/10.1016/j.physletb.2016.03.014

Planck Collaboration: Ade, P. A. R., Aghanim, N., Arnaud, M., Ashdown, M., Aumont, J., Baccigalupi, C., Banday, A. J., Barreiro, R. B., Bartlett, J. G. and et al., 2015, Arxiv e-prints, http://adsabs.harvard.edu/abs/2015arXiv150201589P

Planck Collaboration: Ade, P. A. R., Aghanim, N., Arnaud, M., Ashdown, M., Aumont, J., Baccigalupi, C., Banday, A. J., Barreiro, R. B., Bartlett, J. G. and et al., 2015, Arxiv e-prints, http://adsabs.harvard.edu/abs/2015arXiv150201590P

Press, W. H., Teukolsky, S. A., Vetterling, W. T. and Flannery, B.P., *Numerical Recipes in C: The Art of Scientific Computing*, 1988, Cambridge University Press, ISBN0-521-43108-5

Rahmani, H., Srianand, R., Gupta, N., Petitjean, P., Noterdaeme, P. and Vásquez, D. A., Mon. Not. Roy. Astron. Soc. **425**, 556, http://dx.doi.org/10.1111/j.1365-2966.2012.21503.x

Rahmani, H., Wendt, M., Srianand, R., Noterdaeme, P., Petitjean, P., Molaro, P., Whitmore, J. B., Murphy, M. T., Centurion, M., Fathivavsari, H., D'Odorico, S., Evans, T. M., Levshakov, S. A., Lopez, S., Martins, C. J. A. P., Reimers, D. and Vladilo, G., 2011, Mon. Not. Roy. Astron. Soc. **435**, 861, http://dx.doi.org/10.1093/mnras/stt1356

Riess, A. G., Filippenko, A. V., Challis, P., Clocchiatti, A., Diercks, A., Garnavich, P. M., Gilliland, R. L., Hogan, C. J., Jha, S., Kirshner, R. P., Leibundgut, B., Phillips, M. M., Reiss, D., Schmidt, B. P., Schommer, R. A., Smith, R. C., Spyromilio, J., Stubbs, C., Suntzeff, N. B. and Tonry, J., 1998, Astrophys. J. **116**, 1009, http://dx.doi.org/10.1086/300499

Rosenband, T., Hume, D., Schmidt, P., Chou, C., Brusch, A., Lorini, L., Oskay, W., Drullinger, R., Fortier, T., Stalnaker, J., Diddams, S., Swann, W., Newbury, N., Itano, W., Wineland, D. and J. Bergquist, 2008, Science **319**, 1808 http://dx.doi.org/10.1126/science.1154622

Silva, M. F., Winther, H. A., Mota, D. F. and Martins, C. J. A. P, 2013, Phys. Rev. D, **89**, 024025 http://dx.doi.org/10.1103/PhysRevD.89.024025

Slepian, Z., Gott III, J. R. and Zinn, J., 2014, Mon. Not. Roy. Astron. Soc. **438**, 3, 1948, http://dx.doi.org/10.1093/mnras/stt2195

Songaila, A. and Cowie, L. L., 2014, Astrophys. J. **793**, 103, http://dx.doi.org/10.1088/0004-637X/793/2/103

Suzuki, N., Rubin, D., Lidman, C., Aldering, G., Amanullah, R., Barbary, K., Barrientos, L. F., Botyanszki, J., Brodwin, M. and Connolly, N., 2012, Astrophys. J. **746**, 85, http://dx.doi.org/10.1088/0004-637X/746/1/85

Srianand, R., Gupta, N., Petitjean, P., Noterdaeme, P. and Ledoux, C., 2011, Mon. Not. Roy. Astron. Soc. **405**, 1888, http://dx.doi.org/10.1111/j.1365-2966.2010.16574.x

Uzan, J. P., 2011, Living Rev.Rel. **14**, 2, http://dx.doi.org/10.12942/lrr-2011-2

Wagner, T. A., Schlamminger, S., Gundlach, J. H. and Adelberger, E. G., 2012, Class. Quant. Grav. **29**, 184002, http://dx.doi.org/10.1088/0264-9381/29/18/184002

Webb, J. K., King, J. .A, Murphy, M. T., Flambaum, V. V., Carswell, R. F. and Bainbridge, M. B., 2011, Phys. Rev. Lett., **101**, 191101 L15 http://dx.doi.org/10.1103/PhysRevLett.107.191101

Webb, J. K., Wright, A., Koch, F. E. and Murphy, M. T., 2014, Mem. Soc. Astron. Italiana**85**, p.57, http://adsabs.harvard.edu/abs/2014MmSAI..85...57W

Weiss, A., Walter, F., Downes, D., Carrili, C., Henkel, C., Menten, K. M., Cox, P., 2012, Astrophys.J. **753**, 102, http://dx.doi.org/10.1088/0004-637X/753/2/102

Wendt, M. and Reimers, D., Eur. Phys. J. ST **163**, 197, http://dx.doi.org/10.1140/epjst/e2008-00820-x

White, M., 2008, notes "Angular power spectra and correlation functions", http://mwhite.berkeley.edu/DES/two_point.pdf

Will, C. M., 2014, Liv. Rev. Rel. **17**, 4, http://dx.doi.org/10.12942/lrr-2014-4

van Weerdenburg, F., Murphy, M. T., Malec, A., Kaper, L., and Ubachs, W., 2011, Phys.Rev.Lett. **106**, 180802, http://dx.doi.org/10.1103/PhysRevLett.106.180802

Appendix A.

Cosmological measurements

A.1 MEASUREMENTS OF THE HUBBLE PARAMETER, $H(Z)$

Table A.1: Compilation of measurements by Farooq et al. (2013) of the Hubble parameter and its error, σ_H for a given redshift, z.

z	H(z) $\pm\sigma_H$ (km $s^{-1}Mpc^{-1}$)
0.070	69.0 $\pm$ 19.6
0.100	69.0 $\pm$ 12.0
0.120	68.6 $\pm$ 26.2
0.170	83.0 $\pm$ 8.0
0.179	75.0 $\pm$ 4.0
0.199	75.0 $\pm$ 5.0
0.200	72.9 $\pm$ 29.6
0.270	77.0 $\pm$ 14.0
0.280	88.8 $\pm$ 36.6
0.350	76.3 $\pm$ 5.6
0.352	83.0 $\pm$ 14.0
0.400	95.0 $\pm$ 17.0

Continued on next page

Table A.1 – *Continued from previous page*

z	H(z) $\pm\sigma_H$ (km $s^{-1}Mpc^{-1}$)
0.440	82.6 $\pm$ 7.8
0.480	97.0 $\pm$ 62.0
0.593	104.0 $\pm$ 13.0
0.600	87.9 $\pm$ 6.1
0.680	92.0 $\pm$ 8.0
0.730	97.3 $\pm$ 7.0
0.781	105.0 $\pm$ 12.0
0.875	125.0 $\pm$ 17.0
0.880	90.0 $\pm$ 40.0
0.900	117.0 $\pm$ 23.0
1.037	154.0 $\pm$ 20.0
1.300	168.0 $\pm$ 17.0
1.430	177.0 $\pm$ 18.0
1.530	140.0 $\pm$ 14.0
1.750	202.0 $\pm$ 40.0
2.300	224.0 $\pm$ 8.0

A.2 MEASUREMENTS OF LUMINOSITY DISTANCE

Table A.2: Supernovae Type Ia luminosity distance measurements, its redshift and uncertainty from Suzuki et al. (2012), with the provided number of significant digits.

z	$D_L(z) \pm \sigma$
0.015	68.03 ±5.05816
0.015	75.1544 ±7.52241
0.015	66.4174 ±6.52679
0.015027	61.6649 ±5.05812
0.0151	80.385 ±7.91023
0.015166	66.1201 ±6.55391
0.0152	63.5888 ±6.29809
0.0152	71.068 ±7.90299
0.0153	87.3851 ±8.58139
0.0154363	61.403 ±4.20464
0.016	68.3602 ±6.96094
0.016	58.1998 ±5.57374
0.0163	77.7411 ±7.62173
0.016321	63.604 ±6.00357
0.0163456	64.3881 ±4.23763
0.01645	68.5898 ±7.92501
0.016559	73.9208 ±8.55053
0.01673	70.0273 ±6.75498
0.016743	63.175 ±7.22631
0.016991	75.1198 ±10.7203
0.017173	71.1433 ±8.13223
0.017227	85.2853 ±7.82903
0.0173	70.7859 ±7.02517

Continued on next page

Table A.2 – *Continued from previous page*

z	$D_L(z) \pm \sigma$
0.0173	70.1477 ±7.13905
0.017605	73.9195 ±9.24731
0.0179313	74.1249 ±5.30517
0.0183152	74.8774 ±5.53321
0.0187	102.249 ±9.2855
0.0189	74.9791 ±7.23633
0.0192	88.58 ±8.07053
0.0192	79.1248 ±7.18169
0.019264	97.8414 ±10.8424
0.0195	89.4092 ±8.13304
0.019599	82.6121 ±7.02644
0.0203747	85.3668 ±5.72408
0.0205	83.8409 ±7.39048
0.0208	91.0105 ±8.45066
0.0209	87.2127 ±7.80072
0.0211	85.535 ±7.42087
0.0212	93.2024 ±8.2207
0.0215	96.9499 ±8.35082
0.021793	98.8001 ±10.5762
0.0219	93.2821 ±8.09273
0.02198	93.4533 ±8.07133
0.0221	96.0086 ±8.39884
0.0221	96.4775 ±8.39783
0.0224	97.5927 ±10.7419
0.0229	109.49 ±9.3512
0.0229	106.592 ±8.9839

Continued on next page

Table A.2 – *Continued from previous page*

z	$D_L(z) \pm \sigma$
0.0229712	106.36 ±6.64375
0.023	103.307 ±8.88922
0.023208	104.018 ±11.0884
0.0233	94.7165 ±8.00072
0.0233	109.565 ±9.37172
0.023536	108.123 ±11.6863
0.0239	101.624 ±8.48906
0.023953	98.5694 ±4.85891
0.024	108.452 ±9.76467
0.0241853	102.439 ±6.29164
0.0242	109.113 ±9.05349
0.024314	105.172 ±8.79854
0.024525	102.715 ±4.84555
0.0247	96.1034 ±8.03804
0.0248	112.521 ±9.56589
0.0249	91.3569 ±8.14182
0.0251	97.6461 ±8.05923
0.0255	139.327 ±12.5866
0.0256	137.071 ±11.7519
0.0259	121.114 ±9.95526
0.026	119.195 ±10.0964
0.026038	118.427 ±5.91735
0.0261	118.055 ±10.4638
0.026489	124.778 ±10.9932
0.0266	116.064 ±9.49889
0.0268092	112.728 ±6.63861

Continued on next page

Table A.2 – *Continued from previous page*

z	$D_L(z) \pm \sigma$
0.027342	104.029 ±8.40819
0.0275	134.878 ±10.9546
0.0275687	124.479 ±7.3443
0.0277	138.357 ±11.679
0.027865	104.394 ±10.6932
0.0283	127.073 ±10.5408
0.028396	128.715 ±7.42123
0.028488	117.305 ±12.0956
0.0292	157.948 ±12.716
0.0298021	124.218 ±6.99192
0.029955	156.477 ±16.1681
0.0303	133.553 ±10.8705
0.030529	131.78 ±5.386
0.030604	128.839 ±10.2821
0.0308	133.597 ±10.974
0.0308	143.162 ±11.4261
0.0308	131.432 ±10.4404
0.0309	153.424 ±12.9785
0.0312	133.463 ±11.0765
0.0312	150.166 ±12.0164
0.0315	134.967 ±10.628
0.031528	139.879 ±14.5171
0.032	146.332 ±13.013
0.032	131.129 ±10.4739
0.0321	151.077 ±12.095
0.0321	134.777 ±10.8633

Continued on next page

Table A.2 – *Continued from previous page*

z	$D_L(z) \pm \sigma$
0.0321	149.304 ±11.9459
0.032134	119.022 ±6.98912
0.0325	145.418 ±11.4109
0.0327	165.514 ±12.919
0.0329	154.296 ±12.1074
0.0329124	156.16 ±8.49413
0.0334	149.964 ±12.1391
0.0335	156.591 ±12.2945
0.0336	158.884 ±13.7938
0.0337	147.482 ±12.2074
0.0341	147.36 ±11.8909
0.0341	154.351 ±12.2853
0.0341	142.592 ±11.6603
0.0345	156.909 ±15.2874
0.03572	155.635 ±12.2694
0.036	145.95 ±11.284
0.036	136.726 ±11.2721
0.036	169.535 ±13.8191
0.0362	157.534 ±12.4594
0.036457	168.596 ±16.8969
0.03648	151.728 ±11.8907
0.0366	156.408 ±12.1702
0.0377	144.226 ±19.5341
0.0393	184.875 ±8.43724
0.0402	188.324 ±14.7988
0.0406	187.554 ±14.8834

Continued on next page

Table A.2 – *Continued from previous page*

z	$D_L(z) \pm \sigma$
0.0421	190.587 ±14.9145
0.042233	185.051 ±14.2464
0.0423	189.918 ±15.0066
0.0425	153.328 ±13.7898
0.0437189	189.371 ±11.0942
0.0449767	204.211 ±10.1888
0.045295	212.841 ±16.1709
0.0469673	199.014 ±10.1097
0.0483922	217.354 ±11.9329
0.048818	188.974 ±13.9502
0.048948	221.983 ±17.639
0.0491	221.834 ±17.9638
0.049922	205.776 ±15.3805
0.050043	217.007 ±16.6721
0.0522	216.204 ±18.8296
0.052926	230.961 ±16.5664
0.05371	197.373 ±20.1511
0.0544	245.973 ±9.75242
0.0546	209.851 ±17.072
0.0566834	247.016 ±12.5211
0.0576	260.646 ±19.4275
0.0583	254.992 ±24.2203
0.0583	258.023 ±19.973
0.0589	264.441 ±20.1768
0.0618358	266.808 ±14.2136
0.062668	313.821 ±22.5595

Continued on next page

Table A.2 – *Continued from previous page*

z	$D_L(z) \pm \sigma$
0.0638641	290.528 $\pm$16.0037
0.0643	272.333 $\pm$20.8197
0.0651	289.293 $\pm$21.6901
0.0664403	298.141 $\pm$16.1439
0.0684	351.754 $\pm$27.6339
0.0688	314.288 $\pm$28.6612
0.069	325.994 $\pm$26.4467
0.070086	308.565 $\pm$22.5181
0.074605	329.324 $\pm$24.2307
0.0753501	328.109 $\pm$15.4537
0.0784	343.913 $\pm$13.8132
0.078577	314.509 $\pm$22.5417
0.0800481	344.462 $\pm$16.1753
0.0843	407.724 $\pm$37.6004
0.0856895	397.633 $\pm$21.3084
0.0856961	396.971 $\pm$21.5665
0.0858546	389.483 $\pm$20.1945
0.087589	442.396 $\pm$38.2496
0.0890194	367.867 $\pm$19.8941
0.0929368	425.761 $\pm$23.3226
0.0931494	453.088 $\pm$23.8813
0.0939086	431.086 $\pm$23.4163
0.100915	491.303 $\pm$37.8597
0.102715	498.255 $\pm$27.5099
0.106712	533.744 $\pm$28.9112
0.108638	537.156 $\pm$29.5581

Continued on next page

Table A.2 – *Continued from previous page*

z	$D_L(z) \pm \sigma$
0.113043	513.205 ±28.1805
0.114713	541.775 ±28.286
0.116349	561.342 ±29.0294
0.117277	561.289 ±29.3902
0.117625	519.857 ±27.1986
0.119672	563.777 ±28.7513
0.122829	575.384 ±32.0792
0.1241	581.309 ±29.8794
0.124274	554.622 ±28.3853
0.1244	644.107 ±48.7257
0.126473	552.197 ±30.3123
0.126688	606.795 ±34.6329
0.128727	592.714 ±29.8922
0.129278	607.575 ±37.6057
0.1299	624.938 ±37.2536
0.141788	715.751 ±39.3963
0.142405	665.726 ±34.846
0.143706	687.312 ±36.815
0.1441	585.071 ±42.2414
0.144621	721.383 ±37.449
0.145669	647.654 ±37.5057
0.14629	816.21 ±45.1989
0.147025	725.633 ±37.3121
0.151858	677.888 ±35.5407
0.154632	732.47 ±37.7953
0.155247	730.237 ±38.8128

Continued on next page

Table A.2 – *Continued from previous page*

z	$D_L(z) \pm \sigma$
0.1561	701.214 ±27.1719
0.159	764.316 ±85.4003
0.15989	741.51 ±39.1836
0.160862	730.862 ±39.9328
0.163796	756.681 ±39.4235
0.170628	785.2 ±42.0815
0.172	725.179 ±143.504
0.172742	795.403 ±41.5593
0.17391	806.099 ±47.8757
0.177601	1033.08 ±59.3806
0.178	777.962 ±84.4595
0.179686	879.411 ±47.377
0.18	1091.2 ±223.844
0.18012	846.673 ±45.0578
0.181	864.127 ±90.3688
0.182218	829.399 ±45.5801
0.182549	905.325 ±47.5632
0.183568	875.304 ±49.8931
0.185812	922.188 ±51.2456
0.186	875.858 ±76.2501
0.188853	908.673 ±50.1071
0.189707	972.551 ±53.6031
0.19215	1018.22 ±56.7791
0.194317	982.435 ±57.1751
0.196716	965.792 ±60.0356
0.200612	934.283 ±57.1666

Continued on next page

Table A.2 – *Continued from previous page*

z	$D_L(z) \pm \sigma$
0.202609	985.262 ±58.4438
0.20498	1011.35 ±57.5317
0.205	956.652 ±95.7201
0.210938	992.63 ±55.2291
0.211587	1294.39 ±94.9716
0.21163	990.88 ±52.5838
0.212549	1041.16 ±63.0876
0.213	1051.5 ±108.155
0.214568	1097.41 ±59.1228
0.215	1190.18 ±106.295
0.215543	1146.32 ±74.0156
0.216	1204.99 ±119.425
0.216	1291.84 ±145.219
0.216583	1180.47 ±82.892
0.218	1035.34 ±105.954
0.218347	1107.06 ±63.4324
0.218585	1096.02 ±59.1117
0.228528	1124.31 ±63.1732
0.232781	1098.77 ±76.8051
0.239	1126.75 ±105.94
0.24	1407.47 ±261.109
0.242505	1061.91 ±73.8019
0.244379	1097.45 ±62.8257
0.248508	1133.54 ±65.5885
0.2486	1325.06 ±94.2879
0.249511	1432.8 ±87.3104

Continued on next page

Table A.2 – *Continued from previous page*

z	$D_L(z) \pm \sigma$
0.250668	1409.68 ±78.5321
0.25174	1283.35 ±69.9985
0.252486	1269.65 ±84.8102
0.255491	1250.8 ±86.9596
0.256476	1324.86 ±95.3532
0.257498	1314.72 ±79.5523
0.25774	1349.88 ±84.4758
0.258028	1345.66 ±84.9661
0.26	1461.08 ±134.47
0.260533	1450.86 ±99.0725
0.260586	1272.43 ±82.9712
0.263	1339.47 ±83.0083
0.263491	1423.85 ±83.467
0.263648	1287.17 ±82.8822
0.265762	1257.85 ±72.2943
0.266	1197.13 ±137.95
0.269	1429.66 ±168.81
0.270434	1360.81 ±91.1674
0.271	1277.79 ±126.673
0.273455	1397.76 ±105.352
0.274	1396.14 ±134.165
0.27544	1408.25 ±92.7006
0.277853	1470.96 ±114.477
0.278	1297.92 ±118.618
0.278925	1424.18 ±85.3649
0.279455	1259.67 ±80.4742

Continued on next page

Table A.2 – *Continued from previous page*

z	$D_L(z) \pm \sigma$
0.284	1469.19 ±139.793
0.285	1482 ±93.2237
0.286	1746.73 ±207.651
0.286619	1613.18 ±99.3995
0.288418	1474.2 ±101.562
0.2912	1471.68 ±99.3722
0.29247	1526.9 ±99.4276
0.295586	1688.15 ±167.196
0.297519	1427.06 ±134.845
0.298409	1631.1 ±162.112
0.298777	1606.47 ±114.327
0.3	1557.97 ±225.907
0.300313	1476.96 ±103.046
0.301755	1989.58 ±226.092
0.302	1828.77 ±229.365
0.302402	1609.31 ±99.9839
0.308581	1518.88 ±124.263
0.309	1716.96 ±186.463
0.309	1486.47 ±147.083
0.309493	1598.23 ±99.3321
0.309547	1731.85 ±122.832
0.312883	1595.47 ±102.501
0.314	1763.57 ±196.837
0.31643	1901.14 ±168.856
0.32	1773.87 ±343.911
0.320447	1661.72 ±102.834

Continued on next page

Table A.2 – *Continued from previous page*

z	$D_L(z) \pm \sigma$
0.326396	1564.81 ±104.049
0.329	1853.75 ±230.33
0.330512	1760.3 ±127.048
0.330635	1623.5 ±114.165
0.331	1643.21 ±104.205
0.332	1782.77 ±196.96
0.3373	1815.09 ±114.717
0.338803	1824.21 ±143.577
0.3396	1647.38 ±171.855
0.34	1748.38 ±183.73
0.34	1644.4 ±175.078
0.3402	1843.39 ±115.067
0.341	1578.71 ±163.22
0.342	1891.99 ±187.163
0.344	1716.22 ±165.794
0.346	1874.67 ±131.409
0.348	2079.34 ±208.2
0.348345	1826.24 ±183.152
0.348584	1820.49 ±148.703
0.352	1926.44 ±198.894
0.355	1855.51 ±172.153
0.357	1927.99 ±122.279
0.357507	1844.03 ±172.039
0.3578	1936.34 ±121.359
0.360034	1703.96 ±137.361
0.361934	1891.87 ±145.01

Continued on next page

Table A.2 – *Continued from previous page*

z	$D_L(z) \pm \sigma$
0.363	2043.6 $\pm$195.914
0.366603	2354.89 $\pm$215.163
0.368	1965.8 $\pm$187.558
0.369	2122.29 $\pm$149.187
0.3709	2156.95 $\pm$153.799
0.374	4335.34 $\pm$1843.16
0.378966	2071.56 $\pm$188.026
0.379662	1934.69 $\pm$131.167
0.38	2586.04 $\pm$390.422
0.380359	2145.36 $\pm$215.29
0.380417	1796.67 $\pm$164.287
0.383	2130.13 $\pm$246.232
0.387297	2390.52 $\pm$205.236
0.388	2763.9 $\pm$591.886
0.389289	2091.83 $\pm$193.5
0.391599	2003.3 $\pm$158.277
0.393974	2271.07 $\pm$157.62
0.3965	1984.19 $\pm$184.921
0.399	1984.34 $\pm$267.706
0.399601	2216.97 $\pm$209.431
0.4	2901.04 $\pm$638.048
0.401	2183.16 $\pm$230.543
0.401	3242.83 $\pm$552.392
0.401	2438.52 $\pm$373.771
0.40246	2411.18 $\pm$234.601
0.408319	2333.77 $\pm$221.794

Continued on next page

Table A.2 – *Continued from previous page*

z	$D_L(z) \pm \sigma$
0.41	1859.94 $\pm$220.113
0.412	1926.38 $\pm$276.835
0.415	2373.31 $\pm$154.208
0.416	3052.98 $\pm$782.188
0.416	2048.84 $\pm$286.126
0.420927	2671.22 $\pm$248.884
0.421	2674.28 $\pm$396.565
0.421	2728.51 $\pm$293.742
0.422	2216.47 $\pm$235.495
0.423	2056.39 $\pm$230.67
0.425	1739.51 $\pm$391.844
0.426	2250.69 $\pm$233.126
0.429	2387.85 $\pm$236.943
0.43	1835.57 $\pm$302.476
0.43	3017.92 $\pm$636.987
0.43	2255.42 $\pm$631.846
0.43	2292.91 $\pm$484.463
0.43	2734.17 $\pm$186.567
0.43	2302.42 $\pm$160.193
0.436	2376.86 $\pm$237.015
0.436	2427.47 $\pm$255.173
0.44	2569.84 $\pm$378.463
0.44	2524.23 $\pm$124.946
0.449	2538.71 $\pm$183.626
0.45	2324.87 $\pm$485.752
0.45	2845.74 $\pm$773.133

Continued on next page

Table A.2 – *Continued from previous page*

z	$D_L(z) \pm \sigma$
0.45	3023.36 ±707.697
0.451	2287.36 ±150.691
0.453	3666.42 ±886.288
0.455	2915.99 ±308.359
0.46	2689.61 ±260.227
0.4607	2596.17 ±216.714
0.4627	2561.28 ±174.059
0.463	2452.17 ±300.909
0.465	2317.57 ±640.401
0.468	3234.3 ±244.143
0.469	2957.31 ±385.622
0.47	2672.46 ±188.594
0.472	2476.47 ±586.733
0.475	2636.19 ±310.736
0.477	2575.53 ±217.764
0.479	2953.6 ±487.131
0.48	2703.89 ±649.267
0.49	2277.65 ±468.316
0.493	2687.71 ±326.71
0.495	2653.27 ±542.09
0.495	2816.65 ±301.382
0.496	2772.91 ±195.14
0.497	2916.83 ±225.639
0.497	2601.09 ±265.488
0.498	3951.34 ±1168.96
0.5	2968.93 ±433.878

Continued on next page

Table A.2 – *Continued from previous page*

z	$D_L(z) \pm \sigma$
0.5043	2935.22 ±202.186
0.508	2746.97 ±293.192
0.51	2377.59 ±248.287
0.511	2983.54 ±122.368
0.514	3607.77 ±820.312
0.519	4114.36 ±595.822
0.521	2729.14 ±202.343
0.521	2989.85 ±274.456
0.522	3431.36 ±390.548
0.526	2461.59 ±582.309
0.526	3020.24 ±232.197
0.528	3096.49 ±348.355
0.528	2978.09 ±415.079
0.532	3259.59 ±250.159
0.539	2788.26 ±310.478
0.54	3054.39 ±156.909
0.54	3178.58 ±414.172
0.543	3131.56 ±141.534
0.548	2879.12 ±249.758
0.55	7390.84 ±3426.79
0.55	2851.87 ±203.835
0.5516	2888.26 ±198.523
0.552	3178.24 ±151.361
0.557	3246.4 ±235.4
0.561	3753.1 ±529.782
0.562	4074.78 ±625.281

Continued on next page

Table A.2 – *Continued from previous page*

z	$D_L(z) \pm \sigma$
0.564	2982.49 ±401.088
0.568	3482.17 ±464.317
0.57	3146.46 ±563.592
0.57	3422.11 ±741.293
0.571	3018.79 ±242.207
0.579	4337.83 ±1285.08
0.58	4581.68 ±1097.09
0.581	2586.33 ±601.521
0.581	3535.61 ±253.126
0.581	5416.71 ±975.936
0.5817	3423.01 ±251.907
0.582	4293.21 ±642.967
0.583	3021.52 ±398.631
0.591	4383.5 ±617.728
0.592	6768.17 ±2237.79
0.592	3276.91 ±260.155
0.599	3537.47 ±622.572
0.603	3382.52 ±434.023
0.604	3201.81 ±235.456
0.61	3810.6 ±274.192
0.612	3654.17 ±476.273
0.613	3969.58 ±301.807
0.613	3336.89 ±399.87
0.615	3224.98 ±826.079
0.619	4085.11 ±466.219
0.62	4421.73 ±794.852

Continued on next page

Table A.2 – *Continued from previous page*

z	$D_L(z) \pm \sigma$
0.62	3998.07 ±312.199
0.623	3183.5 ±353.947
0.6268	3562.23 ±257.927
0.631	2988.66 ±337.165
0.631	3770.21 ±406.923
0.633	4073.55 ±318.829
0.633	2756.35 ±329.875
0.64	3571.49 ±310.541
0.64	4294.14 ±383.143
0.64	3844.63 ±495.948
0.643	4001.78 ±306.601
0.645	3659.27 ±394.787
0.655	2904.14 ±664.799
0.656	4255.71 ±1229.21
0.657	3935.95 ±1193.99
0.67	4252.48 ±410.574
0.671	3948.22 ±219.179
0.679	4914.52 ±443.521
0.68	3808.96 ±510.357
0.687	3974.45 ±521.982
0.687	3689.5 ±463.062
0.688	4081.29 ±311.579
0.691	4147.18 ±484.8
0.695	4388.75 ±415.232
0.698	5672.12 ±1132.3
0.707	4534.04 ±535.059

Continued on next page

Table A.2 – *Continued from previous page*

z	$D_L(z) \pm \sigma$
0.71	4021.68 ±341.298
0.711	5167.85 ±872.763
0.721	4316.54 ±372.084
0.73	4522.71 ±405.923
0.735	4153.06 ±383.612
0.74	4544.74 ±415.243
0.741	5539.24 ±569.586
0.75	4452.46 ±283.613
0.752	4574.74 ±436.246
0.756	5791.6 ±514.158
0.763	7843.05 ±3244.04
0.772	5034.99 ±507.412
0.78	5250.03 ±414.202
0.781	4869.07 ±720.557
0.791	5192.5 ±481.46
0.799	4739.86 ±508.97
0.8	5531.11 ±548.062
0.81	4720.4 ±462.341
0.811	4796.31 ±465.213
0.812	5379.16 ±938.898
0.815	6529.51 ±2191.83
0.816	5472.89 ±1153.98
0.817	5374.19 ±520.44
0.818	4770.66 ±587.819
0.821	5347.96 ±477.821
0.8218	5795.26 ±569.01

Continued on next page

Table A.2 – *Continued from previous page*

z	$D_L(z) \pm \sigma$
0.83	5110.7 $\pm$1108.64
0.83	6458.5 $\pm$621.129
0.833	5465.37 $\pm$1311.08
0.839	4782.04 $\pm$489.164
0.84	5951.42 $\pm$609.397
0.84	5045 $\pm$484.867
0.85	4998.64 $\pm$395.468
0.854	5268.57 $\pm$547.293
0.859	6585.38 $\pm$900.599
0.86	6086 $\pm$483.22
0.868	4996.4 $\pm$566.247
0.87	7018.77 $\pm$901.21
0.874	4561.17 $\pm$815.179
0.882	4731.6 $\pm$1272.5
0.885	6868.58 $\pm$905.373
0.905	5342.54 $\pm$633.456
0.91	7262.79 $\pm$893.824
0.9271	6139.03 $\pm$810.559
0.93	5134.36 $\pm$685.5
0.935	5105.51 $\pm$535.167
0.936	4585.86 $\pm$1490.94
0.949	4886.32 $\pm$640.486
0.95	6241.97 $\pm$837.19
0.95	5341.5 $\pm$732.433
0.95	5981.77 $\pm$649.685
0.953	7156.89 $\pm$3146.62

Continued on next page

Table A.2 – *Continued from previous page*

z	$D_L(z) \pm \sigma$
0.96	5280.1 ±669.935
0.961	7125.91 ±1115.93
0.97	3666.41 ±1359.55
0.97	7807.65 ±1047.94
0.974	5845.59 ±469.05
0.975	7357.75 ±720.979
0.978	5012.04 ±675.468
0.983	6783.55 ±1358.91
1.01	6345.92 ±1097.87
1.01	9603.46 ±1476.02
1.017	7224.27 ±569.054
1.02	7457.36 ±758.843
1.02	6804.76 ±728.085
1.03	7047.23 ±458.422
1.057	6762.79 ±743.044
1.092	6332.42 ±718.874
1.11	8415.25 ±1735.52
1.12	7996.15 ±825.141
1.124	8194.15 ±744.381
1.14	7321.35 ±771.09
1.14	6908.61 ±1172.09
1.188	8346.96 ±1924.05
1.19	7457.04 ±848.592
1.192	7793.82 ±718.764
1.215	11202.2 ±2890.57
1.23	10095.7 ±1092.7

Continued on next page

Table A.2 – *Continued from previous page*

z	$D_L(z) \pm \sigma$
1.241	8247.85 $\pm$1816.98
1.265	9745.9 $\pm$1056.83
1.3	10075.2 $\pm$1126.16
1.305	8872.25 $\pm$1060.43
1.307	12082.3 $\pm$1751
1.315	9868.96 $\pm$852.195
1.34	10315.8 $\pm$1306.48
1.35	9234.49 $\pm$789.739
1.37	10231.6 $\pm$1238.02
1.39	9445.98 $\pm$1090.26
1.414	9135.94 $\pm$1456.47

Appendix B.

Measurements of the fine structure constant, α

B.1 ATOMIC CLOCK MEASUREMENTS

Table B.1: Atomic clock constrain on the current drift of α by Rosenband et al. (2008) where we assume $H_0 = 70 kms^{-1} Mpc^{-1}$.

$\frac{1}{H_0}\frac{\dot{\alpha}}{\alpha}$	σ
-2.2 $\times 10^{-7}$	3.2 $\times 10^{-7}$

B.2 RECENT DEDICATED MEASUREMENTS

Table B.2: Dedicated measurements of $\Delta\alpha/\alpha(z)$ in ppm from the UVES Large Program and other recent measurements. Note that the second measurement on table B.3 is the weighted mean from measurements in several absorption systems along lines of sight that are widely separated on the sky whose individual values were not reported by the authors. For that reason, this measurement will not be included in our analysis. The uncertainties of the measurements from Murphy et al. (2016) presented are the systematical and statistical uncertainties added in quadrature.

Object	z	$< \Delta\alpha/\alpha >$	Spectrograph	Reference
J0226-2857	1.023	3.55 $\pm$ 8.72	UVES	Murphy et al. (2016)
3 sources	1.080	4.3 $\pm$ 3.4	UVES	Songaila et al. (2014)
J0058+0041	1.072	-1.39 $\pm$ 7.14	HIRES	Murphy et al. (2016)

Continued on next page

Table B.2 – *Continued from previous page*

Object	z	$<\Delta\alpha/\alpha>$	Spectrograph	Reference
HS1549+1919	1.140	-7.5 $\pm$ 5.5	UVES-HIRES-HDS	Evans et al. (2014)
HE0515-4414	1.150	-0.1 $\pm$ 1.8	UVES	Molaro et al. (2008)
HE0515-4414	1.150	0.5 $\pm$ 2.4	HARPS-UVES	Chand et al. (2006)
J1237+0106	1.305	-4.46 $\pm$ 8.59	HIRES	Murphy et al. (2016)
HS1549+1919	1.340	-0.7 $\pm$ 6.6	UVES-HIRES-HDS	Evans et al. (2014)
J0841+0312	1.342	2.98 $\pm$ 3.67	HIRES	Murphy et al. (2016)
J0814+0312	1.342	5.38 $\pm$ 5.20	UVES	Murphy et al. (2016)
J0108-0037	1.371	-3.96 $\pm$ 3.46	UVES	Murphy et al. (2016)
HE0001-2340	1.580	-1.5 $\pm$ 2.6	UVES	Agafonova et al. (2011)
J1029+1039	1.622	-1.52 $\pm$ 10.13	HIRES	Murphy et al. (2016)
HE1104-1805A	1.660	-4.7 $\pm$ 5.3	HIRES	Songaila et al. (2014)
HE2217-2818	1.690	1.3 $\pm$ 2.6	UVES	Molaro et al. (2013)
HS1946+7658	1.740	-7.9 $\pm$ 6.2	HIRES	Songaila et al. (2014)
HS1549+1919	1.800	-6.4 $\pm$ 7.2	UVES-HIRES-HDS	Evans et al. (2014)
Q1101-264	1.840	5.7 $\pm$ 2.7	UVES	Molaro et al. (2008)
Q2206-1958	1.921	-4.60 $\pm$ 6.42	UVES	Murphy et al. (2016)
Q1755+57	1.971	4.68 $\pm$ 4.68	HIRES	Murphy et al. (2016)
PHL957	2.309	-1.44 $\pm$ 6.85	HIRES	Murphy et al. (2016)
PHL957	2.309	-1.94 $\pm$ 13.17	UVES	Murphy et al. (2016)

B.3 ARCHIVAL MEASUREMENTS

Table B.3: Archival measurements dataset of $\Delta\alpha/\alpha$ and its statistical uncertainty $\sigma_{\Delta\alpha/\alpha}$ used by Webb et al. (2011). σ_{flag} is the systematical error described on table B.4. The measurements are sorted by observational sub-samples within the telescope used as defined by Murphy et al. (2009). A is the previous low redshift sample from Murphy et al. (2003), B1 is the previous high redshift sample from Murphy et al. (2003), B2 is the addition of 15 absorbers from Murphy et al. (2004) and C is the labeled new sample from Murphy et al. (2003). D is for the VLT sample.

z_{abs}	$\Delta\alpha/\alpha(10^{-5})$	$\sigma_{\Delta\alpha/\alpha}(10^{-5})$	Sample	Telescope	σ_{flag}
J000520+052410	0.85118	-0.340 $\pm$ 1.284	A	Keck	1
J012017+213346	0.72913	0.041 $\pm$ 1.297	A	Keck	1
J012017+213346	1.0479	-0.202 $\pm$ 2.199	A	Keck	1
J012017+213346	1.3246	0.703 $\pm$ 0.804	A	Keck	1
J012017+213346	1.3428	-1.290 $\pm$ 0.949	A	Keck	1
J042315-012033	0.63308	4.282 $\pm$ 4.088	A	Keck	1
J045312-130546	1.1743	-3.033 $\pm$ 1.093	A	Keck	1
J045312-130546	1.2294	-1.472 $\pm$ 0.818	A	Keck	1
J045312-130546	1.2324	0.981 $\pm$ 2.757	A	Keck	1
J045647+040052	0.85929	0.578 $\pm$ 1.205	A	Keck	1
J045647+040052	1.1534	-0.743 $\pm$ 1.787	A	Keck	1
J082601-223027	0.91059	-0.391 $\pm$ 0.609	A	Keck	1
J115129+382552	0.55339	-1.837 $\pm$ 1.716	A	Keck	1
J120858+454035	0.92741	-0.218 $\pm$ 1.390	A	Keck	1
J121549-003432	1.3196	-0.725 $\pm$ 0.761	A	Keck	1
J121549-003432	1.5541	-1.870 $\pm$ 0.878	A	Keck	1
J122527+223512	0.66802	0.075 $\pm$ 1.475	A	Keck	1
J122824+312837	1.7954	-1.295 $\pm$ 1.050	A	Keck	1
J125048+395139	0.77292	2.228 $\pm$ 1.179	A	Keck	1
J125048+395139	0.85452	-0.021 $\pm$ 1.270	A	Keck	1
J125659+042734	0.51934	-3.365 $\pm$ 3.256	A	Keck	1

Continued on next page

Table B.3 – *Continued from previous page*

Object	z_{abs}	$\Delta\alpha/\alpha(10^{-5})$	Sample	Telescope	σ_{flag}
J125659+042734	0.93426	1.877 $\pm$ 1.796	A	Keck	1
J131956+272808	0.66004	0.444 $\pm$ 1.505	A	Keck	1
J142326+325220	0.84324	0.102 $\pm$ 0.846	A	Keck	1
J142326+325220	0.90301	-0.999 $\pm$ 1.783	A	Keck	1
J142326+325220	1.1726	-3.204 $\pm$ 1.546	A	Keck	1
J163429+703132	0.9901	1.156 $\pm$ 2.399	A	Keck	1
J002208-150538	3.4388	0.937 $\pm$ 3.912	B1	Keck	1
J010311+131617	2.3095	-3.949 $\pm$ 1.370	B1	Keck	2
J015234+335033	2.1408	-5.418 $\pm$ 2.160	B1	Keck	2
J020455+364917	1.4761	-0.658 $\pm$ 1.216	B1	Keck	1
J020455+364917	1.9550	1.992 $\pm$ 1.048	B1	Keck	2
J020455+364917	2.3240	0.017 $\pm$ 1.640	B1	Keck	1
J020455+364917	2.4563	-5.853 $\pm$ 2.597	B1	Keck	1
J020455+364917	2.4628	0.576 $\pm$ 1.729	B1	Keck	2
J034943-381031	3.0247	-2.835 $\pm$ 3.422	B1	Keck	1
J084424+124548	2.3742	2.265 $\pm$ 3.827	B1	Keck	2
J084424+124548	2.4761	-4.664 $\pm$ 1.973	B1	Keck	2
J121732+330538	1.9990	5.498 $\pm$ 3.178	B1	Keck	2
J175746+753916	2.6253	-0.751 $\pm$ 1.388	B1	Keck	2
J175746+753916	2.6253	-0.591 $\pm$ 1.773	B1	Keck	2
J220852-194359	0.94841	-3.664 $\pm$ 1.857	B1	Keck	1
J220852-194359	1.0172	-0.318 $\pm$ 0.734	B1	Keck	1
J220852-194359	1.9204	1.399 $\pm$ 0.703	B1	Keck	2
J223235+024755	1.8585	-5.480 $\pm$ 1.174	B1	Keck	2
J223235+024755	1.8640	-1.012 $\pm$ 0.492	B1	Keck	2
J223408+000001	2.0653	-2.614 $\pm$ 1.017	B1	Keck	2

Continued on next page

Table B.3 – *Continued from previous page*

Object	z_{abs}	$\Delta\alpha/\alpha(10^{-5})$	Sample	Telescope	σ_{flag}
J235129-142748	2.2794	1.366 $\pm$ 4.161	B1	Keck	1
J000149-015940	2.0951	0.034 $\pm$ 0.727	B1	Keck	2
J000149-015940	2.1539	3.605 $\pm$ 3.954	B1	Keck	1
J025518+004847	3.2534	-2.494 $\pm$ 3.066	B2	Keck	2
J074521+473436	1.6111	-2.489 $\pm$ 2.022	B2	Keck	1
J074521+473436	3.0173	1.226 $\pm$ 2.782	B2	Keck	2
J083943+104321	2.4673	6.973 $\pm$ 4.395	B2	Keck	1
J095500-013006	2.6238	2.141 $\pm$ 7.358	B2	Keck	1
J095744+330820	4.1798	1.237 $\pm$ 3.933	B2	Keck	1
J111113-080402	1.9746	0.286 $\pm$ 2.326	B2	Keck	1
J111113-080402	3.6061	-0.420 $\pm$ 4.402	B2	Keck	1
J121303+171423	0.69404	-1.920 $\pm$ 3.916	B2	Keck	1
J121303+171423	0.84142	0.579 $\pm$ 0.804	B2	Keck	1
J121303+171423	1.8918	-0.445 $\pm$ 0.903	B2	Keck	2
J122607+173649	2.4653	-1.306 $\pm$ 1.656	B2	Keck	2
J122607+173649	2.5577	-0.253 $\pm$ 3.503	B2	Keck	1
J235057-005209	2.4264	-4.879 $\pm$ 3.485	B2	Keck	1
J235057-005209	2.6147	-0.697 $\pm$ 3.801	B2	Keck	2
J000322-260316	1.4342	-1.253 $\pm$ 1.167	C	Keck	1
J000322-260316	3.3897	-7.843 $\pm$ 3.548	C	Keck	1
J000520+052410	0.59137	-3.105 $\pm$ 2.433	C	Keck	1
J000520+052410	0.85118	0.475 $\pm$ 1.022	C	Keck	1
J005757-264314	1.2679	2.057 $\pm$ 2.521	C	Keck	1
J005757-264314	1.3192	-2.587 $\pm$ 2.410	C	Keck	1
J005757-264314	1.5337	-1.345 $\pm$ 1.156	C	Keck	1
J010054+021136	0.61256	0.372 $\pm$ 1.191	C	Keck	1

Continued on next page

Table B.3 – *Continued from previous page*

Object	z_{abs}	$\Delta\alpha/\alpha(10^{-5})$	Sample	Telescope	σ_{flag}
J010054+021136	0.72508	-2.634 $\pm$ 3.523	C	Keck	1
J012227-042127	0.65741	7.123 $\pm$ 4.608	C	Keck	1
J015734+744243	0.7455	-2.056 $\pm$ 0.745	C	Keck	1
J020944+051714	3.6663	-0.599 $\pm$ 3.503	C	Keck	1
J021857+081727	1.7680	0.046 $\pm$ 1.235	C	Keck	1
J024008-230915	1.3650	-0.222 $\pm$ 0.523	C	Keck	1
J024401-013402	2.0994	-0.813 $\pm$ 2.621	C	Keck	1
J030450-221157	1.0092	-0.193 $\pm$ 1.009	C	Keck	1
J045142-132032	1.2667	-1.268 $\pm$ 1.462	C	Keck	1
J053007-250329	0.94398	0.758 $\pm$ 2.337	C	Keck	1
J053007-250329	2.1406	-0.865 $\pm$ 0.867	C	Keck	2
J053007-250329	b2.8114	0.919 $\pm$ 0.863	C	Keck	2
J064204+675835	1.2938	-1.393 $\pm$ 0.624	C	Keck	1
J074521+473436	1.6112	-1.298 $\pm$ 1.727	C	Keck	1
J074521+473436	3.0173	0.822 $\pm$ 2.196	C	Keck	1
J080117+521034	2.6021	-1.629 $\pm$ 2.272	C	Keck	1
J080117+521034	2.8677	-1.878 $\pm$ 3.977	C	Keck	1
J084424+124548	1.0981	-3.570 $\pm$ 1.220	C	Keck	1
J084424+124548	1.1314	0.561 $\pm$ 0.789	C	Keck	1
J084424+124548	1.2189	-0.521 $\pm$ 0.542	C	Keck	1
J084424+124548	2.3742	1.411 $\pm$ 1.164	C	Keck	2
J093337+284532	3.2351	0.855 $\pm$ 1.824	C	Keck	1
J094253-110425	1.0598	-0.751 $\pm$ 1.643	C	Keck	1
J095852+120245	2.3103	-2.245 $\pm$ 6.439	C	Keck	1
J101155+294141	1.1117	-5.459 $\pm$ 2.508	C	Keck	1
J101447+430030	1.4162	-0.904 $\pm$ 0.560	C	Keck	1

Continued on next page

Table B.3 – *Continued from previous page*

Object	z_{abs}	$\Delta\alpha/\alpha(10^{-5})$	Sample	Telescope	σ_{flag}
J101447+430030	2.9587	1.861 $\pm$ 1.948	C	Keck	2
J105756+455553	3.3172	2.747 $\pm$ 6.067	C	Keck	1
J111038+483115	0.80757	1.215 $\pm$ 1.221	C	Keck	1
J111038+483115	0.86182	-2.024 $\pm$ 1.636	C	Keck	1
J111038+483115	1.0158	-2.098 $\pm$ 0.937	C	Keck	1
J113508+222715	2.1053	4.361 $\pm$ 3.976	C	Keck	1
J120523-074232	1.7549	-1.465 $\pm$ 2.178	C	Keck	1
J120858+454035	0.92741	-0.280 $\pm$ 0.777	C	Keck	1
J122607+173649	2.4653	1.654 $\pm$ 1.908	C	Keck	1
J122607+173649	2.5577	0.419 $\pm$ 1.198	C	Keck	1
J122824+312837	1.7954	0.648 $\pm$ 1.415	C	Keck	1
J124714+312641	0.85048	-6.900 $\pm$ 7.023	C	Keck	1
J124714+312641	2.7504	2.485 $\pm$ 4.788	C	Keck	1
J131011+460124	0.22909	2.549 $\pm$ 5.395	C	Keck	1
J134002+110630	2.7955	4.109 $\pm$ 9.498	C	Keck	1
J142656+602550	2.7698	-0.688 $\pm$ 1.866	C	Keck	1
J142656+602550	2.8268	0.319 $\pm$ 0.929	C	Keck	1
J143912+295448	1.2259	0.280 $\pm$ 1.433	C	Keck	1
J144453+291905	2.4389	-0.939 $\pm$ 1.712	C	Keck	1
J155152+191104	1.1425	-0.092 $\pm$ 0.663	C	Keck	1
J155152+191104	1.3422	-0.853 $\pm$ 1.169	C	Keck	1
J155152+191104	1.8024	-2.001 $\pm$ 1.267	C	Keck	1
J162645+642655	0.58596	-1.977 $\pm$ 4.530	C	Keck	1
J162645+642655	2.1102	-0.164 $\pm$ 1.168	C	Keck	1
J163429+703132	0.9901	-2.202 $\pm$ 1.293	C	Keck	1
J185230+401906	1.9900	-1.562 $\pm$ 0.899	C	Keck	2

Continued on next page

Table B.3 – *Continued from previous page*

Object	z_{abs}	$\Delta\alpha/\alpha(10^{-5})$	Sample	Telescope	σ_{flag}
J194454+770552	1.7385	-0.194 $\pm$ 1.861	C	Keck	1
J214805+065738	0.79026	0.088 $\pm$ 0.590	C	Keck	1
J223408+000001	1.2128	1.326 $\pm$ 1.490	C	Keck	1
J223408+000001	2.0653	1.717 $\pm$ 1.249	C	Keck	2
J223408+000001	2.6532	-3.310 $\pm$ 1.938	C	Keck	2
J223619+132620	2.548	1.015 $\pm$ 6.186	C	Keck	1
J223619+132620	2.5548	-1.851 $\pm$ 6.572	C	Keck	1
J223619+132620	3.1513	-4.111 $\pm$ 3.441	C	Keck	1
J234628+124859	0.73117	-1.211 $\pm$ 0.976	C	Keck	1
J234628+124859	1.5899	0.449 $\pm$ 1.163	C	Keck	1
J234628+124859	2.1711	-0.944 $\pm$ 1.204	C	Keck	1
J234628+124859	2.4300	-1.322 $\pm$ 0.379	C	Keck	2
J234646+124527	1.0465	-0.750 $\pm$ 1.514	C	Keck	1
J234646+124527	1.1161	0.005 $\pm$ 1.964	C	Keck	1
J234646+124527	2.5378	-3.856 $\pm$ 2.277	C	Keck	1
J000344-232355	0.4521	-0.459 $\pm$ 0.787	D	VLT	3
J000344-232355	0.9491	-1.534 $\pm$ 2.788	D	VLT	3
J000344-232355	1.5864	-0.410 $\pm$ 1.003	D	VLT	3
J000448-415728	1.9886	0.266 $\pm$ 1.945	D	VLT	3
J000448-415728	2.1679	1.381 $\pm$ 0.944	D	VLT	3
J001210-012207	1.2030	0.772 $\pm$ 1.190	D	VLT	3
J001602-001225	0.6351	-0.673 $\pm$ 3.545	D	VLT	3
J001602-001225	0.6363	-1.561 $\pm$ 3.914	D	VLT	3
J001602-001225	0.8575	1.266 $\pm$ 1.826	D	VLT	3
J001602-001225	1.1468	-1.581 $\pm$ 2.922	D	VLT	3
J001602-001225	2.0292	-0.909 $\pm$ 0.934	D	VLT	3

Continued on next page

Table B.3 – *Continued from previous page*

Object	z_{abs}	$\Delta\alpha/\alpha(10^{-5})$	Sample	Telescope	σ_{flag}
J004131-493611	2.1095	0.386 $\pm$ 2.856	D	VLT	3
J004131-493611	2.2485	-1.230 $\pm$ 0.672	D	VLT	3
J005758-264314	1.2679	1.076 $\pm$ 1.931	D	VLT	3
J005758-264314	1.5336	-0.456 $\pm$ 0.903	D	VLT	3
J010311+131617	1.7975	0.443 $\pm$ 0.548	D	VLT	3
J010311+131617	2.3092	-0.082 $\pm$ 0.563	D	VLT	3
J010821+062327	1.9328	2.184 $\pm$ 2.454	D	VLT	3
J011143-350300	1.1827	0.142 $\pm$ 0.950	D	VLT	3
J011143-350300	1.3499	0.084 $\pm$ 0.378	D	VLT	3
J012417-374423	0.8221	0.702 $\pm$ 1.050	D	VLT	3
J012417-374423	0.8593	-0.677 $\pm$ 2.516	D	VLT	3
J012417-374423	1.2433	1.838 $\pm$ 1.221	D	VLT	3
J012417-374423	1.9102	-3.872 $\pm$ 3.111	D	VLT	3
J013105-213446	1.8566	0.236 $\pm$ 1.445	D	VLT	3
J014333-391700	0.3400	-6.748 $\pm$ 3.914	D	VLT	3
J014333-391700	1.7101	-1.465 $\pm$ 2.357	D	VLT	3
J015733-004824	0.7693	2.647 $\pm$ 4.288	D	VLT	3
J024008-230915	1.1846	-1.513 $\pm$ 2.754	D	VLT	3
J024008-230915	1.6359	1.000 $\pm$ 1.110	D	VLT	3
J024008-230915	1.6373	-0.187 $\pm$ 1.020	D	VLT	3
J024008-230915	1.6574	-0.137 $\pm$ 1.010	D	VLT	3
J033106-382404	0.7627	0.440 $\pm$ 0.988	D	VLT	3
J033106-382404	0.9709	-4.485 $\pm$ 4.216	D	VLT	3
J033106-382404	1.4380	-4.323 $\pm$ 2.571	D	VLT	3
J033108-252443	0.9925	0.513 $\pm$ 1.232	D	VLT	3
J033108-252443	2.4547	-2.122 $\pm$ 5.496	D	VLT	3

Continued on next page

Table B.3 – *Continued from previous page*

Object	z_{abs}	$\Delta\alpha/\alpha(10^{-5})$	Sample	Telescope	σ_{flag}
J033244-445557	2.4112	-1.000 $\pm$ 0.793	D	VLT	3
J033244-445557	2.6563	1.079 $\pm$ 1.689	D	VLT	3
J040718-441013	2.4126	2.420 $\pm$ 2.220	D	VLT	3
J040718-441013	2.5499	0.895 $\pm$ 0.353	D	VLT	3
J040718-441013	2.5948	0.574 $\pm$ 0.345	D	VLT	3
J040718-441013	2.6214	4.264 $\pm$ 2.744	D	VLT	3
J042707-130253	1.4080	-2.551 $\pm$ 1.110	D	VLT	3
J042707-130253	1.5632	-2.967 $\pm$ 2.449	D	VLT	3
J042707-130253	2.0351	8.057 $\pm$ 3.830	D	VLT	3
J043037-485523	1.3556	-0.405 $\pm$ 0.232	D	VLT	3
J044017-433308	1.4335	0.139 $\pm$ 2.500	D	VLT	3
J044017-433308	2.0482	1.400 $\pm$ 0.864	D	VLT	3
J051707-441055	0.2223	1.262 $\pm$ 3.703	D	VLT	3
J051707-441055	0.4291	-3.153 $\pm$ 1.502	D	VLT	3
J053007-250329	2.1412	0.676 $\pm$ 0.359	D	VLT	3
J055246-363727	1.2252	0.269 $\pm$ 0.895	D	VLT	3
J055246-363727	1.7475	-0.936 $\pm$ 1.155	D	VLT	3
J055246-363727	1.9565	1.740 $\pm$ 1.530	D	VLT	3
J064326-504112	2.6592	-1.530 $\pm$ 1.920	D	VLT	3
J091613+070224	1.3324	8.233 $\pm$ 5.915	D	VLT	3
J094253-110426	1.0595	0.372 $\pm$ 0.737	D	VLT	3
J094253-110426	1.7891	-2.330 $\pm$ 0.495	D	VLT	3
J103909-231326	1.4429	-1.980 $\pm$ 2.720	D	VLT	3
J103909-231326	2.7778	-1.130 $\pm$ 0.660	D	VLT	3
J103921-271916	0.8771	2.159 $\pm$ 2.071	D	VLT	3
J103921-271916	1.0093	-0.643 $\pm$ 3.280	D	VLT	3

Continued on next page

Table B.3 – *Continued from previous page*

Object	z_{abs}	$\Delta\alpha/\alpha(10^{-5})$	Sample	Telescope	σ_{flag}
J103921-271916	1.9721	2.980 $\pm$ 0.847	D	VLT	3
J104032-272749	1.3861	0.446 $\pm$ 0.693	D	VLT	3
J104032-272749	1.7761	0.262 $\pm$ 1.320	D	VLT	3
J110325-264515	1.1868	-0.745 $\pm$ 0.925	D	VLT	3
J110325-264515	1.2029	0.623 $\pm$ 0.830	D	VLT	3
J110325-264515	1.5515	-0.669 $\pm$ 0.998	D	VLT	3
J110325-264515	1.8389	0.612 $\pm$ 0.395	D	VLT	3
J111113-080401	3.6077	22.962 $\pm$ 16.134	D	VLT	3
J112010-134625	1.6283	0.886 $\pm$ 1.130	D	VLT	3
J112442-170517	0.8062	1.738 $\pm$ 1.373	D	VLT	3
J112442-170517	1.2342	2.271 $\pm$ 1.571	D	VLT	3
J115411+063426	1.7739	-0.739 $\pm$ 0.784	D	VLT	3
J115411+063426	1.8197	-0.948 $\pm$ 0.974	D	VLT	3
J115411+063426	2.3660	3.090 $\pm$ 1.780	D	VLT	3
J115944+011206	0.7908	1.561 $\pm$ 1.080	D	VLT	3
J115944+011206	1.3305	2.137 $\pm$ 2.249	D	VLT	3
J115944+011206	1.9438	0.518 $\pm$ 0.442	D	VLT	3
J120342+102831	1.3224	-0.965 $\pm$ 1.930	D	VLT	3
J120342+102831	1.3422	-2.006 $\pm$ 1.443	D	VLT	3
J120342+102831	1.5789	1.743 $\pm$ 2.716	D	VLT	3
J121140+103002	1.0496	-1.538 $\pm$ 0.672	D	VLT	3
J123200-022404	0.7569	2.253 $\pm$ 3.219	D	VLT	3
J123200-022404	0.8308	1.672 $\pm$ 0.911	D	VLT	3
J123437+075843	1.0201	-2.213 $\pm$ 1.442	D	VLT	3
J123437+075843	1.7194	0.485 $\pm$ 0.943	D	VLT	3
J133335+164903	0.7446	-0.828 $\pm$ 0.542	D	VLT	3

Continued on next page

Table B.3 – *Continued from previous page*

Object	z_{abs}	$\Delta\alpha/\alpha(10^{-5})$	Sample	Telescope	σ_{flag}
J133335+164903	1.3253	4.962 $\pm$ 10.607	D	VLT	3
J133335+164903	1.7765	0.843 $\pm$ 0.448	D	VLT	3
J133335+164903	1.7863	-0.489 $\pm$ 0.860	D	VLT	3
J134427-103541	1.9155	0.015 $\pm$ 0.744	D	VLT	3
J134427-103541	2.1474	6.448 $\pm$ 8.831	D	VLT	3
J135038-251216	1.4393	-0.987 $\pm$ 0.568	D	VLT	3
J135038-251216	1.7529	6.396 $\pm$ 3.258	D	VLT	3
J141217+091624	1.4187	-2.919 $\pm$ 1.771	D	VLT	3
J141217+091624	2.0188	0.849 $\pm$ 0.755	D	VLT	3
J141217+091624	2.4564	-0.903 $\pm$ 1.390	D	VLT	3
J141217+091624	2.6682	0.199 $\pm$ 0.849	D	VLT	3
J143040+014939	0.4878	3.580 $\pm$ 2.170	D	VLT	3
J143040+014939	1.2030	-0.812 $\pm$ 3.290	D	VLT	3
J143040+014939	1.2411	-2.660 $\pm$ 1.200	D	VLT	3
J144653+011356	0.5097	-0.567 $\pm$ 1.142	D	VLT	3
J144653+011356	0.6602	-0.073 $\pm$ 1.831	D	VLT	3
J144653+011356	1.1020	1.395 $\pm$ 4.030	D	VLT	3
J144653+011356	1.1292	2.278 $\pm$ 2.760	D	VLT	3
J144653+011356	1.1595	-2.557 $\pm$ 1.205	D	VLT	3
J145102-232930	1.5855	-4.500 $\pm$ 2.456	D	VLT	3
J200324-325144	2.0329	2.440 $\pm$ 1.200	D	VLT	3
J200324-325144	3.1878	3.411 $\pm$ 1.153	D	VLT	3
J200324-325144	3.1917	2.238 $\pm$ 4.217	D	VLT	3
J212912-153841	1.7380	1.310 $\pm$ 0.636	D	VLT	3
J212912-153841	2.0225	-1.628 $\pm$ 1.244	D	VLT	3
J212912-153841	2.6378	1.320 $\pm$ 3.330	D	VLT	3

Continued on next page

Table B.3 – *Continued from previous page*

Object	z_{abs}	$\Delta\alpha/\alpha(10^{-5})$	Sample	Telescope	σ_{flag}
J212912-153841	2.7686	-0.206 $\pm$ 1.090	D	VLT	3
J213314-464030	1.6148	4.320 $\pm$ 1.568	D	VLT	3
J214159-441325	2.1329	-0.470 $\pm$ 2.222	D	VLT	3
J214159-441325	2.3828	1.170 $\pm$ 0.858	D	VLT	3
J214159-441325	2.8523	2.089 $\pm$ 0.524	D	VLT	3
J214225-442018	0.9865	-0.093 $\pm$ 1.050	D	VLT	3
J214225-442018	1.0529	1.500 $\pm$ 1.290	D	VLT	3
J214225-442018	1.1543	-6.250 $\pm$ 4.000	D	VLT	3
J214225-442018	1.7569	-6.183 $\pm$ 4.308	D	VLT	3
J214225-442018	2.1126	1.177 $\pm$ 0.858	D	VLT	3
J214225-442018	2.2533	2.220 $\pm$ 1.120	D	VLT	3
J214225-442018	2.3798	0.747 $\pm$ 1.510	D	VLT	3
J220734-403655	1.6270	6.091 $\pm$ 2.709	D	VLT	3
J220852-194359	0.9478	0.151 $\pm$ 1.305	D	VLT	3
J220852-194359	0.9483	-2.686 $\pm$ 2.009	D	VLT	3
J220852-194359	1.0172	-0.525 $\pm$ 0.546	D	VLT	3
J220852-194359	1.0182	-0.412 $\pm$ 1.040	D	VLT	3
J220852-194359	1.2970	-1.435 $\pm$ 2.763	D	VLT	3
J220852-194359	1.9206	0.857 $\pm$ 0.385	D	VLT	3
J220852-194359	2.0762	0.942 $\pm$ 0.584	D	VLT	3
J222006-280323	0.7866	-0.557 $\pm$ 1.479	D	VLT	3
J222006-280323	0.9408	1.691 $\pm$ 1.762	D	VLT	3
J222006-280323	0.9424	0.988 $\pm$ 1.250	D	VLT	3
J222006-280323	1.5554	0.945 $\pm$ 0.604	D	VLT	3
J222006-280323	1.6279	2.300 $\pm$ 0.861	D	VLT	3
J222756-224302	1.4129	-1.649 $\pm$ 1.785	D	VLT	3

Continued on next page

Table B.3 – *Continued from previous page*

Object	z_{abs}	$\Delta\alpha/\alpha(10^{-5})$	Sample	Telescope	σ_{flag}
J222756-224302	1.4334	-4.507 $\pm$ 2.935	D	VLT	3
J222756-224302	1.4518	1.024 $\pm$ 1.586	D	VLT	3
J222756-224302	1.6398	-1.484 $\pm$ 2.957	D	VLT	3
J233446-090812	2.1522	0.525 $\pm$ 0.437	D	VLT	3
J233446-090812	2.2015	-0.058 $\pm$ 5.494	D	VLT	3
J233446-090812	2.2875	0.758 $\pm$ 0.376	D	VLT	3
J234625+124743	2.1733	4.160 $\pm$ 7.517	D	VLT	3
J234625+124743	2.5718	-17.274 $\pm$ 6.799	D	VLT	3
J234628+124858	1.1084	-1.536 $\pm$ 2.527	D	VLT	3
J234628+124858	1.5899	3.051 $\pm$ 2.268	D	VLT	3
J234628+124858	2.1713	-0.794 $\pm$ 0.951	D	VLT	3
J235034-432559	1.7962	0.942 $\pm$ 3.357	D	VLT	3

Table B.4: Values of the correspondent σ_{flag} in units of 10^{-5}- error associated to the random component (see Webb et al. (2011)). LC and HC mean "Low Constrast" and "High Contrast" as the Keck sample was computed in different ways.

Telescope	σ_{flag}	value
VLT	3	0.905
Keck LC	1	0
Keck HC	2	1.743

Appendix C.

Measurements of the proton-electron mass ratio, μ

Table C.1: Proton-electron mass ratio measurements compiled by Ferreira et al. (2015) listed by object along line of sight, the redshift and the value of the measurement with its corresponding uncertainty, as well as the original reference.

Object	z	$\Delta\mu/\mu[ppm]$	Reference
B0218+357	0.685	0.74 $\pm$ 0.89	Murphy et al. (2008)
B0218+357	0.685	-0.35 $\pm$ 0.12	Kanekar (2011)
PKS1830-211	0.886	0.08 $\pm$ 0.47	Henkel et al. (2009)
PKS1830-211	0.886	-1.2 $\pm$ 4.5	Ilyushin et al. (2012)
PKS1830-211	0.886	-2.04 $\pm$ 0.74	Muller et al. (2011)
PKS1830-211	0.886	-0.10 $\pm$ 0.13	Bagdonaite et al. (2013)
J2123-005	2.059	8.5 $\pm$ 4.2	van Weerdenburg et al. (2011)
J2123-005	2.059	5.6 $\pm$ 6.2	Malec et al. (2010)
HE0027-1836	2.402	-7.6 $\pm$ 10.2	Rahmani et al. (2013)
Q2348-011	2.426	-6.8 $\pm$ 27.8	Bagdonaite et al. (2012)
Q0405-443	2.597	10.1 $\pm$ 6.2	King et al. (2008)
J0643-504	2.659	7.4 $\pm$ 6.7	Albornoz Vásquez et al. (2014)
J1237+0647	2.690	-5.4 $\pm$ 7.5	Dàpra et al. (2015)
Q0528-250	2.811	0.3 $\pm$ 3.7	King et al. (2011)
Q0347-383	3.025	2.1 $\pm$ 6.0	Wendt et al. (2008)
J1443+2724	4.224	-9.5 $\pm$ 7.6	Bagdonaite et al. (2015)

Appendix D.

Measurements of combinations of fundamental couplings, $\Delta Q/Q$

Table D.1: Combined measurements of the dimensionless couplings α, μ and g_p from the compilation of Ferreira et al. (2014) (and references therein). The list is sorted by redshift z and specifies the object along the line of sight, the dimensionless parameter being constrained and the measurement with its associated uncertainty in parts per million.

Object	z	Q_{AB}	$\Delta Q_{AB}/Q_{AB}[ppm]$	Reference
PKS1413+135	0.247	$\alpha^{2\times1.85} g_p \mu^{1.85}$	-11.8 $\pm$ 4.6	Kanekar et al. (2010)
PKS1413+135	0.247	$\alpha^{2\times1.57} g_p \mu^{1.57}$	5.1 $\pm$ 12.6	Darling (2004)
PKS1413+135	0.247	$\alpha^2 g_p$	-2.0 $\pm$ 4.4	Murphy et al. (2001)
B0218+357	0.685	$\alpha^2 g_p$	-1.6 $\pm$ 5.4	Murphy et al. (2001)
J0135-0931	0.765	$\alpha^{2\times1.57} g_p \mu^{1.57}$	-5.2 $\pm$ 4.3	Kanekar et al. (2012)
J2358-1020	1.173	$\alpha^2 g_p/\mu$	1.8 $\pm$ 2.7	Rahmani et al. (2012)
J1623-0718	1.336	$\alpha^2 g_p/\mu$	-3.7 $\pm$ 3.4	Rahmani et al. (2012)
J2340-0053	1.361	$\alpha^2 g_p/\mu$	-1.3 $\pm$ 2.0	Rahmani et al. (2012)
J0501-0159	1.561	$\alpha^2 g_p/\mu$	3.0 $\pm$ 3.1	Rahmani et al. (2012)
J1024+4709	2.285	$\alpha^2 \mu$	100 $\pm$ 40	Curran et al. (2011)
J2135-0102	2.326	$\alpha^2 \mu$	-100 $\pm$ 100	Curran et al. (2011)
J1636+6612	2.517	$\alpha^2 \mu$	-100 $\pm$ 120	Curran et al. (2011)

Continued on next page

Table D.1 – *Continued from previous page*

Object	z	Q_{AB}	$\Delta Q_{AB}/Q_{AB}[ppm]$	Reference
H1413+117	2.558	$\alpha^2\mu$	-40 $\pm$ 80	Curran et al. (2011)
J1401+0252	2.565	$\alpha^2\mu$	-140 $\pm$ 80	Curran et al. (2011)
J0911+0551	2.796	$\alpha^2\mu$	-6.9 $\pm$ 3.7	Weiss et al. (2012)
J1337+3152	3.147	$\alpha^2 g_p/\mu$	-1.7 $\pm$ 1.7	Srianand et al. (2010)
APM0828+5255	3.174	$\alpha^2\mu$	-360 $\pm$ 90	Curran et al. (2011)
MM1842+5938	3.930	$\alpha^2\mu$	-180 $\pm$ 40	Curran et al. (2011)
PSS2322+1944	4.112	$\alpha^2\mu$	170 $\pm$ 130	Curran et al. (2011)
BR1202-0725	4.695	$\alpha^2\mu$	50 $\pm$ 150	Lentati et al. (2013)
J0918+5142	5.245	$\alpha^2\mu$	-1.7 $\pm$ 8.5	Levshakov et al. (2012)
J1148+5251	6.420	$\alpha^2\mu$	330 $\pm$ 250	Lentati et al. (2013)

Table D.2: Recent combined measurements of the dimensionless coupling $\alpha^2 g_p/\mu$. Listed is the name of the object along the line of sight, the redshift and the measurement itself with its corresponding uncertainty in parts per million. (Darling (2012) - Figure 4 - the individual data were requested directly to the author).

Object name	z	$\Delta Q_{AB}/Q_{AB}[ppm]$
0952+179	0.234	2.01 $\pm$ 5.02
1127-145	0.313	-7.86 $\pm$ 4.57
1229-021	0.395	22.1 $\pm$ 28.6
0235+164	0.524	-7.98 $\pm$ 3.95
1331+170	1.776	-12.8 $\pm$ 2.98
1157+014	1.944	23.1 $\pm$ 4.20
0458-020	2.040	1.88 $\pm$ 2.48